ABSTRACT

Title of dissertation: **TIME-REVERSAL MASSIVE MULTIPATH EFFECT AND BANDWIDTH HETEROGENEITY**

Yi Han, Doctor of Philosophy, 2016

Dissertation directed by: Professor K. J. Ray Liu
Department of Electrical and Computer Engineering

The proliferation of new mobile communication devices, such as smartphones and tablets, has led to an exponential growth in network traffic. The demand for supporting the fast-growing consumer data rates urges the wireless service providers and researchers to seek a new efficient radio access technology, which is the so-called 5G technology, beyond what current 4G LTE can provide. On the other hand, ubiquitous RFID tags, sensors, actuators, mobile phones and etc. cut across many areas of modern-day living, which offers the ability to measure, infer and understand the environmental indicators. The proliferation of these devices creates the term of the Internet of Things (IoT). For the researchers and engineers in the field of wireless communication, the exploration of new effective techniques to support 5G communication and the IoT becomes an urgent task, which not only leads to fruitful research but also enhance the quality of our everyday life.

Massive MIMO, which has shown the great potential in improving the achievable rate with a very large number of antennas, has become a popular candidate.

However, the requirement of deploying a large number of antennas at the base station may not be feasible in indoor scenarios. Does there exist a good alternative that can achieve similar system performance to massive MIMO for indoor environment? In this dissertation, we address this question by proposing the time-reversal technique as a counterpart of massive MIMO in indoor scenario with the massive multipath effect.

It is well known that radio signals will experience many multipaths due to the reflection from various scatters, especially in indoor environments. The traditional TR waveform is able to create a focusing effect at the intended receiver with very low transmitter complexity in a severe multipath channel. TR's focusing effect is in essence a spatial-temporal resonance effect that brings all the multipaths to arrive at a particular location at a specific moment. We show that by using time-reversal signal processing, with a sufficiently large bandwidth, one can harvest the massive multipaths naturally existing in a rich-scattering environment to form a large number of virtual antennas and achieve the desired massive multipath effect with a single antenna. Further, we explore the optimal bandwidth for TR system to achieve maximal spectral efficiency. Through evaluating the spectral efficiency, the optimal bandwidth for TR system is found determined by the system parameters, e.g., the number of users and backoff factor, instead of the waveform types. Moreover, we investigate the tradeoff between complexity and performance through establishing a generalized relationship between the system performance and waveform quantization in a practical communication system. It is shown that a 4-bit quantized waveforms can be used to achieve the similar bit-error-rate compared to

the TR system with perfect precision waveforms.

Besides 5G technology, Internet of Things (IoT) is another terminology that recently attracts more and more attention from both academia and industry. In the second part of this dissertation, the heterogeneity issue within the IoT is explored. One of the significant heterogeneity considering the massive amount of devices in the IoT is the device heterogeneity, i.e., the heterogeneous bandwidths and associated radio-frequency (RF) components. The traditional middleware techniques result in the fragmentation of the whole network, hampering the objects interoperability and slowing down the development of a unified reference model for the IoT. We propose a novel TR-based heterogeneous system, which can address the bandwidth heterogeneity and maintain the benefit of TR at the same time. The increase of complexity in the proposed system lies in the digital processing at the access point (AP), instead of at the devices' ends, which can be easily handled with more powerful digital signal processor (DSP). Meanwhile, the complexity of the terminal devices stays low and therefore satisfies the low-complexity and scalability requirement of the IoT. Since there is no middleware in the proposed scheme and the additional physical layer complexity concentrates on the AP side, the proposed heterogeneous TR system better satisfies the low-complexity and energy-efficiency requirement for the terminal devices (TDs) compared with the middleware approach.

TIME-REVERSAL MASSIVE MULTIPATH EFFECT AND BANDWIDTH HETEROGENEITY

by

Yi Han

Dissertation submitted to the Faculty of the Graduate School of the
University of Maryland, College Park in partial fulfillment
of the requirements for the degree of
Doctor of Philosophy
2016

Advisory Committee:
Professor K. J. Ray Liu, Chair/Advisor
Professor Min Wu
Professor Gang Qu
Dr. Zoltan Safar
Dr. Beibei Wang
Professor Lawrence C. Washington

Dedication

To my Family —

Fengkun Han, Aiqin Shi,

and Jingsha Chen.

Acknowledgments

First and foremost, I would like to express my most esteemed gratitude to my advisor, Prof. K. J. Ray Liu for his patient guidance and continuous support during my Ph.D. study. I would not have been able to afford studying abroad without his help in applying scholarships in the very beginning. His constant enthusiasm and inspiration lead me to innovative research and contributing to the advance of wireless communications. I appreciate his influence in my motivation, attitude, and my professional and personal development. I will always remember his advice — be confident, open your mind, and collaborate with others — which is the best thing I have learned throughout my graduate career.

I would also like to thank all members in my dissertation committee. I am specially grateful to Dr. Beibei Wang for kind guidance on my writing and research work, and thankful to Dr. Zoltan Safar for enlightening discussions on research and for generously sharing with me his invaluable industry experience. I also thank Prof. Min Wu, Prof. Gang Qu and Prof. Lawrence Washington for their time and efforts serving on my dissertation committee and reviewing my thesis.

I would like to thank all members in Signal and Information Group for their pleasant friendship and assistance. I have learned so much from Yan Chen, and Beibei Wang for their mentorship and collaboration on research. Special thanks to Feng Han, Yu-Han Yang, Chunxiao Jiang, Matthew Stamm, Hung-Quoc Lai, Zhung-Han Wu, Hang Ma, Chen Chen, Feng Zhang and Qinyi Xu for various thoughtful discussions and the wonderful time during the past few years.

I thank all my friends for the moments we shared, which gave me rest and reinvigoration to overcome the stresses of life. Thanks to Prof. Xianyi Gong and Prof. Minjian Zhao for encouraging me to study abroad. Special thanks to my wife and my cat, Jingsha Chen and Pumpkin, for their companionship and love, which enriched and lightened my daily life during the past years.

Most importantly, I give my most sincere appreciation to my parents, Fengkun Han and Aiqin Shi, and my wife, Jingsha Chen. Without their endless love, encouragement, and emotional support, I would not have been able to walk through my graduate study to this important achievement. This dissertation is dedicated to them.

Table of Contents

List of Tables

List of Figures

Chapter 1

Introduction

1.1 Motivation

The past decade has witnessed the monumental success of mobile and wireless access to the Internet. Nevertheless, the proliferation of new mobile communication devices, such as smartphones and tablets, has led to an exponential growth in network traffic. As indicated by the most recent Cisco Visual Networking Index (VNI) annual report [14], the global mobile data traffic grew 74% and the number of mobile devices increased 563 million in 2015. The global mobile data traffic is also predicted in the report that will increase nearly eightfold between 2015 and 2020. The demand for supporting the fast-growing consumer data rates urges the wireless service providers and researchers to seek a new efficient radio access technology, which is the so-called 5G technology, beyond what current 4G LTE can provide.

Besides 5G technology, Internet of Things (IoT) recently attracts more and more attention from both academia and industry. The new terminology is created by the proliferation of ubiquitous RFID tags, sensors, actuators, mobile phones and etc., which blend seamlessly with the environment around us. In the past decade, the coverage of IoT has been extended to a wide range of applications

1

including healthcare, utilities, transport, etc. [59]. Due to its high impact on several aspects of everyday life and behavior of the potential users [5], IoT is listed as one of six "Disruptive Civil Technologies" by the US National Intelligence Council with potential impacts on US national power [45].

For the researchers and engineers in the field of wireless communication, the exploration of new effective techniques to support 5G communication and the IoT becomes an urgent task of significant importance, which not only leads to fruitful research but also enhance the quality of our everyday life.

Massive multiple-input multiple-output (MIMO), besides ultra-densification and mmWave, is one of "big three" 5G technology [2], which can offer multi-fold benefits such as enormous enhancement in spectral efficiency and power efficiency [46] and simple transmit/receiver structures due to the quasi-orthogonal nature [42]. These benefits make massive MIMO one of the five disruptive technology directions for 5G communication [7].

Even though the benefits of massive MIMO seem very promising, several critical challenges must first be addressed before it can be implemented in practice. Considering the requirement of deploying a large amount of antennas, massive MIMO system may be not feasible in indoor scenarios, where 95% of data traffic will come from [50]. Does there exist a good alternative that can achieve similar system performance to massive MIMO for indoor environments? The answer is yes and the time-reversal (TR) technology is potentially a counterpart of massive MIMO in indoor scenarios.

It is well known that radio signals will experience many multipaths due to the

reflection from various scatters, especially in indoor environments. The traditional TR waveform [65] is able to create a focusing effect at the intended receiver with very low transmitter complexity in a severe multipath channel. Such a waveform is simply the time-reverse of the channel impulse response which is transmitted by propagating back through each multipath with channel reciprocity. TR's focusing effect is in essence a spatial-temporal resonance effect that brings all the multipaths to arrive at a particular location at a specific moment. Such a phenomenon will allow us to utilize the naturally existing multipaths as virtual antennas to realize the massive multipath effect, which is a counterpart of massive MIMO effect, even with a single antenna.

In essence, TR's ability to distinguish different receivers depends on the number of resolved multipaths in the environment. In order to harvest the multipaths, a large bandwidth can be utilized. More specifically, more multipaths can be resolved with the increase of bandwidth because of the better time resolution. On the other hand, broader bandwidth provides not only substantial more degrees of freedom but also challenges for system design due to the severe interference in high speed communications under large delay spread channels. Even though millimeter wave (mmWave) band may be utilized by TR communication in future, the spectrum is still a scarce resource with its own cost, and there is no existing work studying how much bandwidth is needed by TR communication to optimize its spectral efficiency.

As a promising candidate for 5G communication, the complexity is a critical metric. Due to the fact that TR utilizes the multipaths as virtual antenna array and the environment as the computational resource, the receiver complexity is

3

hence very low according to the one-tap detection, that is, the receiver detects the received signal using only one sample instead of more complicated receiver equalization. Therefore, the overall complexity of the communication system concentrates on the transmitter side. At the transmitter, embedding the waveforms into the transmit signal becomes the most complicated process in TR communication especially with a rate of gigabit per second [1]. Considering the practical implementation in hardware, the waveforms of the TR system are quantized and thus of limited precision instead of the prefect precision due to the resource constraint of hardware. Such a quantization on the waveforms will lead to the performance degradation, but there is no existing work fully discussing the tradeoff between the complexity and performance.

With the massive amount of devices and various application scenarios in the IoT, the devices within the IoT are highly heterogenous. To enable the connectivity between heterogenous devices, some existing works build middlewares to hide the technical details from the application layer. However, these techniques are often not suitable for resource-constrained scenario and hampering the devices interoperability. An overview of the TR wireless paradigm for green IoT has been presented in [13], where it is claimed that the TR-based paradigm can handle most challenges in IoT at the same time. Nevertheless, the TR-based paradigm in [13] cannot be applied directly to address the heterogeneity, because of the implicit assumption that all devices share the same bandwidth and RF front-end.

1.2 Dissertation Outline and Contributions

From the above discussions, we can see that TR technique has the great potential for both 5G communication and IoT. On the other hand, there are many new challenges to the system design. In this dissertation, we address these problems with a focus on the massive multipath effect and bandwidth heterogeneity. The first part of this dissertation is about the deployment of the time-reversal technique for 5G communication. In the second part, time-reversal technique is utilized to enable the connectivity among heterogeneous devices in the IoT. The rest of this dissertation is organized as follows.

1.2.1 Time-Reversal Massive Multipath Effect (Chapter 2)

In this chapter, we show that by using TR signal processing, with a sufficiently large bandwidth, one can harvest the massive multipaths naturally existing in a rich-scattering environment to form a large number of virtual antennas and achieve the desired massive multipath effect with a single antenna. We prove theoretically that TR technique can achieve the massive multipath effect, similar to the quasi-orthogonal property in massive MIMO, and completely eliminate the interference.

We further investigate the achievable rate with some waveforms, where the corresponding asymptotic achievable rate is derived under a massive multipath setting. Experiment results based on real indoor channel measurements show the massive multipaths can be revealed with a sufficiently large bandwidth in a practical indoor environment. Moreover, based on our experiments with real indoor measurements,

the achievable rate of the time-reversal wideband system is evaluated.

1.2.2 How Much Bandwidth is Needed? (Chapter 3)

In Chapter 2, it is shown that the massive multipath effect and thus system performance in TR communication rely on the ability to resolve many multipaths with a large bandwidth. However, the bandwidth is a limited resource and boarder bandwidth may result in severe interference in high speed communications under large delay spread channels.

In this chapter, we study the optimal bandwidth for a TR system to achieve maximum spectral efficiency. By evaluating the spectral efficiency of TR system with varying bandwidth and different waveform types, we find that the optimal bandwidth for TR system is determined by system parameters such as the number of users and backoff factor instead of waveform types.

Moreover, a sub-optimal bandwidth for the system is derived solely based on the rank condition of channel matrix, which can be easily acquired without evaluating the spectral efficiency. Simulation results validate the theoretical analysis and show that the sub-optimal bandwidth is very close to the optimal one when the backoff factor is small.

1.2.3 Limited Waveform Precision: Tradeoff Between Complexity and Performance (Chapter 4)

A key metric for 5G technology is the system complexity. Based on the asymmetric system architecture, the overall complexity most lie in the waveform-embedding process at the transmitter. Considering the resource constraint in hardware, the waveform is inevitably quantized, which degrades the TR spatio-temporal resonating effect and thus the system performance. In this chapter, we establish a general relation between the precision of waveform and the system performance. We derive theoretically the effective signal-to-interference-plus-noise ratio (SINR) with varying quantization stepsize. A metric α is proposed to characterize the performance loss due to the quantization.

Further, the effect of system parameters on the quantization requirement is discussed through evaluating the relative system performance degradation with varying system parameters. Based on the bit-error-rate (BER) performance evaluation, we conclude that 4-bit resolution for waveform is enough in the TR system.

1.2.4 Enabling Heterogeneous Connectivity (Chapter 5)

In this chapter, a novel TR-based heterogeneous system is proposed to support the bandwidth heterogeneity in the IoT, which can address the bandwidth heterogeneity and maintain the benefit of TR at the same time. By integrating the multirate signal processing into TR technique, the proposed system is capable to support these heterogeneous devices with a single set of RF front-end, therefore it is

a unified framework for connecting devices of heterogeneous bandwidths. Although there is an increase in complexity, it concentrates mostly on the digital processing of the access point (AP), which can be easily handled with more powerful digital signal processor (DSP). Since there is no middleware in the proposed system and the additional physical layer complexity concentrates on the AP side, the proposed TR approach better satisfies the requirement of low-complexity and energy-efficiency for terminal devices (TDs).

We further conduct the theoretical analysis of the interference in the proposed system. System performance is evaluated through both theoretical analysis and simulations, which show that the proposed system can serve the devices of heterogeneous bandwidths with a reasonable BER performance and the BER performance can be improved significantly with appropriate spectrum allocation.

Chapter 2

Time-Reversal Massive Multipath Effect

As introduced in Chapter 1, several critical challenges must first be addressed before the massive MIMO can be implemented in practice. First of all, a challenging task is the analog front-end design [40], for example, each tiny antenna need its own power amplifier and analog-to-digital convertor (ADC). Moreover, the antenna correlation and mutual coupling due to the increasing number of antennas has to be carefully addressed as well [3, 43]. The researchers in Lund University built a 100-antenna MIMO testbed, and the size is $0.8 \times 1.2 \times 1$ m with 300kg weight and 2.5kW average power consumption [63]. Considering the requirement of deploying a large amount of antennas, massive MIMO system may be not feasible in indoor scenarios. It is expected that 95% of data traffic will come from indoor in a few years [50], therefore a natural question to ask is: does there exist a good alternative that can achieve similar system performance to massive MIMO for indoor environments? The answer is yes and the time-reversal (TR) technology is potentially a counterpart of massive MIMO in indoor scenarios.

It is well known that radio signals will experience many multipaths due to the reflection from various scatters, especially in indoor environments. TR's focusing effect is in essence a spatial-temporal resonance effect that brings all the multipaths
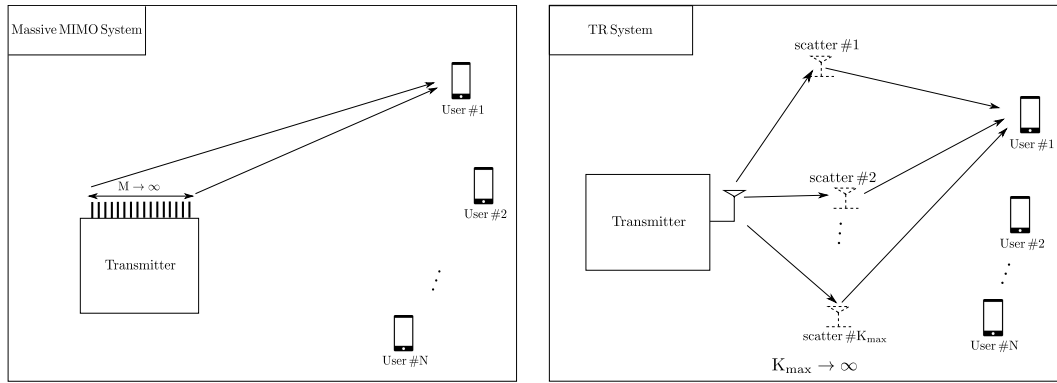
(a) An illustration of massive MIMO system.   (b) An illustration of TR system.

Figure 2.1: Comparison between massive MIMO system and TR system.

to arrive at a particular location at a specific moment. Such a phenomenon will allow us to utilize the naturally existing multipaths as virtual antennas to realize the massive multipath effect, which is a counterpart of massive MIMO effect, even with a single antenna. As shown in Fig. 2.1, TR inherently treats the multipaths in the environment as virtual antennas, similar to MIMO that uses multiple antennas for better spatial multiplexing. In essence, if cooperation of users, e.g. cooperative communications, is a distributed way of achieving MIMO effect of high diversity, then TR is similarly a distributed way to achieve the massive MIMO effect through utilizing the multipaths as virtual antennas. The TR waveform is nothing but to control each multipath (virtual antenna).

In order to harvest the multipaths, the transmit power and bandwidth can be utilized. More specifically, the maximum number of observable multipaths given by an environment increases with the transmit power. Once the power is fixed, the maximum number of observable multipaths is also fixed. In addition, more multipaths can be resolved with the increase of bandwidth because of the better time

resolution. Based on the real indoor ultra-wide-band (UWB) channel measurement (both LOS and NLOS) in [31, 55], around 60-80 independent multipaths can be revealed with a sufficiently large bandwidth. Later in Section 2.5.2, we will discuss about how to realize the massive multipath in a practical indoor environment.

TR technology is a promising candidate for indoor communication, but it requires wide bandwidth to achieve good time resolution. The wideband signal naturally requires the high sampling rate based on the Nyquist samping theorem, which leads to heavy computation burden in terms of processing. Fortunately, as indicated by Moore's Law, the more powerful analog-to-digital-converter (ADC) and digital signal processor (DSP) reduce the wideband signal processing cost dramatically [33]. Moreover, researchers and engineers are currently searching for new available wide band and re-allocating bandwidth for 5G technology [2]. For TR technology, it may use the spectrum of ultra-wide-band (UWB) or mmWave band. Based on the existing study at high frequencies, there still exists a large amount of multipaths, which is essential for TR communication. For example, based on the building penetration and reflection measurements of 28GHZ in NYC [54], the RF energy is mostly retained within buildings due to low attenuation and high reflection through indoor materials. Moreover, the delay spread for indoor 60GHz channels ranges between 30ns and 70ns [57], which indicates a multipath-rich environment. Even though the spectral efficiency of TR technique is not that high, it becomes more and more important to reduce complexity, operation energy consumption and offer other benefits given the potential wide bandwidth, especially in indoor scenarios.

By exploiting the massive number of virtual antennas, TR system can achieve

11

superior focusing effect in spatial-temporal domain, resulting in the promising performance as an indoor communication candidate for 5G. Moreover, the implementation complexity of TR system is much lower since it utilizes the environment as the virtual antenna array and computing resource. Specifically, in this chapter, we consider a Time-Reversal Division Multiple Access (TRDMA) downlink communication system [28] to demonstrate the TR massive multipath effect (TRMME) under typical waveforms, i.e., the basic TR, zero-forcing (ZF) and minimum mean square error (MMSE) waveforms. We further derive the asymptotic achievable rate performance as the number of observable multipaths grows to infinity. Later, we discuss the approach to realize massive multipaths based on real-world indoor channel measurements. Through the experiments with real indoor measurements, the achievable rate of a TR wideband system with a single antenna is evaluated.

This chapter is organized as follows. We first discuss the existing related work in Section 2.1. The system model is discussed in Section 2.2. In Section 2.3, the notion of TRMME is introduced assuming that the TR system has the ability to reveal infinite multipaths in a rich-scattering environment. In Section 2.4, the expected achievable rate of the TR system with typical waveforms are investigated. Moreover, the asymptotic achievable rates with these waveforms is derived in a massive multipath setting. The approach to realize massive multipaths in a practical indoor environment is discussed based on the real-world channel measurements in Section 2.5. Finally, Section 2.6 concludes the chapter.

2.1 Related Work

The TR technology was first introduced to compensate the delay distortion on wired transmission lines by Bogert from Bell Labs in the fifties [8]. Then, it has been applied in various areas including ultrasonics [23], acoustical imaging [38], electromagnetic imaging [39], and underwater acoustic communication [21]. More recently, TR has drawn more and more attention from researchers in the wireless communications field [17, 19, 48]. Under a rich-scattering environment, a TR communication system is shown to have the spatial-temporal focusing effect and thus work as an ideal platform for green wireless communications [9, 65] in terms of lower power consumption and less radio pollution. A time-reversal division multiple access (TRDMA) scheme is proposed in [28] which utilizes the location-specific waveform to separate different users' signal. It is shown in [28, 34] that the TR communication system can be extended to multiple-antenna scenarios easily, and more advanced waveform design can be implemented to further suppress the ISI and inter-user-interference (IUI) to achieve higher data rate [68–70]. The potential application of TR technology in the Internet of Things is discussed in [13, 30].

A closely related technology to TR is the code division multiple access (CD-MA). While TR technology utilizes the designed waveforms to distinguish multiple users, CDMA employs spread-spectrum to allocate distinct orthogonal codes to multiple users [64]. Compared with the Rake receiver deployed to counter the effect of multipaths in the CDMA system, TR technology harvests the multipaths in the environment to perform beamforming with the appropriate precoding at the trans-

mitter, which results in much lower complexity at the receiver side.

Time-Reversal is neither a new terminology in MIMO technology as well. First of all, time-reversal beamforming is well known as conjugate beamforming in MIMO systems when the system bandwidth is small [6]. Then, for wide-band, frequency-selective channel, OFDM can rigorously decompose the channel into parallel independent narrow-bandwidth sub-carriers, where TR precoding can be applied [35,41]. TR can be also employed as the precoding scheme directly for a single carrier wide-band system [52,71].

The focus of this chapter is not on the combination of massive MIMO and TR technologies. Instead, we show that TR technology itself is a promising approach to realize the massive multipath effect, which is similar to massive MIMO effect, for indoor communications. Together with the theoretic analysis of the TRMME, the idea of realizing massive virtual antennas with a single physical one and the approach to resolve the multipaths with the increase of bandwidth in an indoor environment constitute the novelty of our work.

2.2   System Model

In this chapter, we consider a time-reversal downlink system where one transmitter simultaneously communicates with N distinct receivers through the TRDMA technique [28]. We assume that both the transmitter and receivers are equipped with one single antenna. However, the results can be easily extended to the multiple-antenna scenario.

2.2.1 Channel Model

Suppose there are totally K_{max} independent multipaths from the transmitter to the jth receiver, then the channel $h_j(t)$ can be written as

$$h_j(t) = \sum_{k=1}^{K_{max}} \tilde{h}_{j,k} \delta(t - \tau_k), \tag{2.1}$$

where $\tilde{h}_{j,k}$ and τ_k are the complex channel gain and path delay of the kth path, respectively. Note that the delay spread of the channel is given by $\tau_C = \tau_{K_{max}}$.

Let W be the bandwidth of the TR system. Then, through Nyquist sampling, the discrete channel responses can obtained as

$$h_j[n] = \int_{n\tau_p - \tau_p}^{n\tau_p} p(n\tau_p - \tau) h_j(\tau) d\tau, \tag{2.2}$$

where $p(t)$ is the pulse with main lobe $\tau_p = 1/W$.

Through (2.2), a L-tap channel $\mathbf{h}_j = \left[h_j[1], h_j[2], ..., h_j[L] \right]^T$ with $L = round(\tau_C W)$ can be resolved for the link between the transmitter and the jth receiver as follows

$$\mathbf{h}_j = [h_{j,1}, h_{j,2}, \cdots, h_{j,L}], \tag{2.3}$$

where $h_{j,i}$ is the complex channel gain of the ith tap, and $h'_{j,i}s$ are independent for all $i \in [1, L]$ and $j \in [1, N]$.

Suppose that there are K non-zero elements in the L-tap channel $\mathbf{h}_j$. When the bandwidth W is small, all elements in $\mathbf{h}_j$ are generally non-zero, i.e., $K = L$. On the other hand, when W is sufficiently large, the side lobes of $p(t)$ becomes negligible and thus there are at most $K = K_{max} < L$ non-zero elements in $\mathbf{h}_j$. Let $\phi_{K_{max}}$ be the non-zero multipath set, which reflects the physical patterns of scatters

15
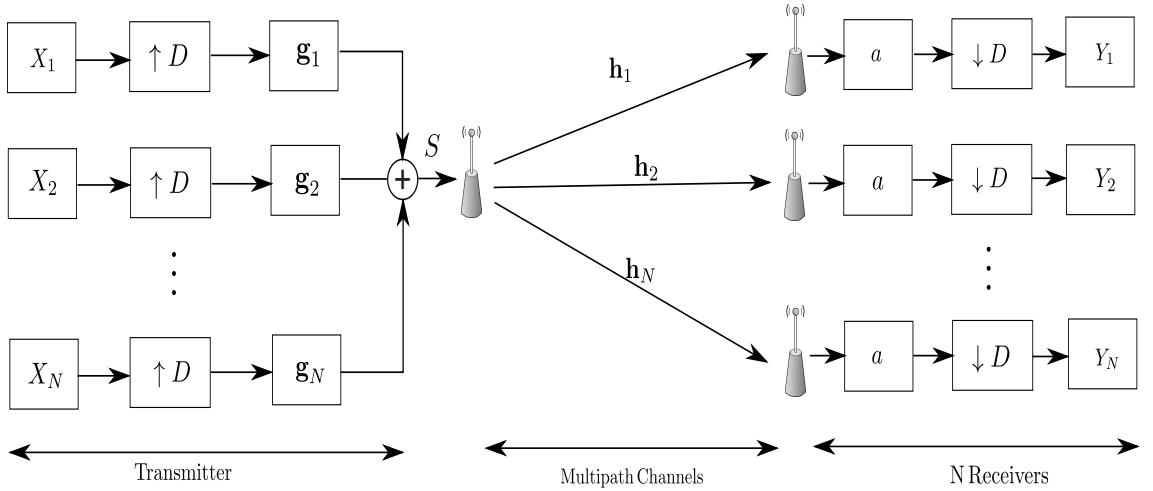
Figure 2.2: TRDMA System.

distribution in the environment. Then, $h_j[k] = 0$ for $k \notin \phi_{K_{max}}$, and for $k \in \phi_{K_{max}}$, $h_j[k]$ is a complex random variable with zero mean and variance σ_k^2.

Prior to the TR-transmission, a pseudo random sequence is sent to the transmitter from the receiver, based on which the channel state information (CSI) $\mathbf{h}_j$ is estimated. By cross-correlating the received signal with the known pseudo random sequence, the power of CSI is boosted thus maintaining the good CSI quality. Due to the more powerful DSP and the efficient Golay correlator [53], the CSI estimation is obtained quickly in terms of time consumption by converting the multiplication operation into addition/substruction. In addition, based on the real measurement in [67], the CSI is quite stationary given only slightly changing of the environment, which indicates the channel need not to be re-probed very frequently and the overhead price of channel probing is very small.

Note that pilot contamination, when a lot of users simultaneously channel probe to the base station, will cause the performance degradation in the TR system

due to the non-ideal CSI. In the following, we assume the estimated CSI is perfect.

2.2.2 TRDMA Downlink Communication

In the TR system, the transmitter simultaneously communicates with multiple receivers. Specifically, as shown in Fig. 2.2, the information to be transmitted to the jth receiver, denoted as X_j, is first up-sampled by a backoff factor D to alleviate the interference, and then precoded by a waveform $\mathbf{g}_j$. Actually, the symbol rate is lower down by D to suppress the ISI caused by the multipath channel. Note that multiple designs of the waveform such as basic TR waveform [65], zero-forcing (ZF) waveform [15] and minimal mean square error (MMSE) waveform [69] can be utilized, and the details will be discussed in the next section. After that, all signals to different receivers are mixed together as follows

$$S[k] = \sum_{i=1}^{N} \left(X_i^{[D]} * \mathbf{g}_i \right)[k], \tag{2.4}$$

where

$$X_i^{[D]}[k] = \begin{cases} X_i[k/D], & \text{if } mod(k, D) = 0, \\ \\ 0, & \text{otherwise.} \end{cases} \tag{2.5}$$

The mixed signal is broadcast to all receivers through the rich-scatter environment. At the receiver side, the jth receiver simply scales the received signal and down-samples it to obtain the estimated signal Y_j as follows

$$\begin{aligned} Y_j[k] =&(\mathbf{h}_j * \mathbf{g}_j)[L]X_j[k - \frac{L}{D}] + \sum_{l=1, l \neq L/D}^{\frac{2L-1}{D}} (\mathbf{h}_j * \mathbf{g}_j)[Dl]X_j[k - l] \\ &+ \sum_{i=1, i \neq j}^{N} \sum_{l=1}^{\frac{2L-1}{D}} (\mathbf{h}_j * \mathbf{g}_i)[Dl]X_i[k - l] + n_j[k]. \end{aligned} \tag{2.6}$$

17

Without loss of generality, we assume with the typical waveforms $(\mathbf{h}_j * \mathbf{g}_j)$ has the resonating effect at time index L. Then the first term in (2.6) is the desired signal, the second term is the ISI, the third term is the IUI, and the last term is the noise.

The (2.6) can be re-written by replacing the convolution as inner product as follows

$$
\begin{aligned}
Y_j[k] = \mathbf{H}_j^{(\frac{L}{D})} \mathbf{g}_j X_j[k - \frac{L}{D}] + \sum_{l=1, l \neq L/D}^{(2L-1)/D} \mathbf{H}_j^{(l)} \mathbf{g}_j X_j[k - l] \\
+ \sum_{l=1}^{(2L-1)/D} \mathbf{H}_j^{(l)} \left(\sum_{i=1, i \neq j}^{N} \mathbf{g}_i X_i[k - l] \right) + n_j[k],
\end{aligned}
\tag{2.7}
$$

where $\mathbf{H}_j^{(m)}$ is the mth row of the $(2L-1)/D \times L$ matrix $\mathbf{H}_j$ decimated by rows of Toeplitz matrix, which can be written in (2.8).

$$
\mathbf{H}_j = \begin{pmatrix}
h_j[D] & h_j[D-1] & \cdots & h_j[1] & 0 & \cdots & \cdots & 0 \\
h_j[2D] & h_j[2D-1] & \cdots & \cdots & h_j[1] & 0 & \cdots & 0 \\
\vdots & \vdots & \ddots & \ddots & \ddots & \ddots & \ddots & \vdots \\
h_j[L] & h_j[L-1] & \cdots & \cdots & \cdots & \cdots & \cdots & h_j[1] \\
\vdots & \vdots & \ddots & \ddots & \ddots & \ddots & \ddots & \vdots \\
0 & \cdots & 0 & h_j[L] & \cdots & \cdots & h_j[L-D+1] & h_j[L-2D] \\
0 & \cdots & \cdots & 0 & h_j[L] & \cdots & h_j[L-D+1] & h_j[L-D]
\end{pmatrix}.
\tag{2.8}
$$

Therefore, $\mathbf{H}_j^{(\frac{L}{D})}$ is the time-reversal channel

$$
\mathbf{H}_j^{(\frac{L}{D})} = \left[h_j[L]\, h_j[L-1] \cdots h_j[1] \right].
\tag{2.9}
$$

2.2.3 Expected Achievable Rate for Individual User

Let P and P_n be the average transmitting power and noise power, respectively, and $(\cdot)^\dagger$ represents the conjugate transpose operator. According to (2.7) and the uplink-downlink duality [32, 56, 61], the achievable rate of the jth receiver can be derived using its dual uplink format, where the uniform power allocation is assumed. Then we take an expectation of the downlink achievable rate as shown in (2.10). In the rest of the chapter, we analyze the expected achievable rate of the TR system.

$$R_j = \frac{W}{D} \mathbb{E}\left[\log_2\left(1 + \frac{\frac{P}{N}\mathbf{g}_j^\dagger \mathbf{H}_j^{(\frac{L}{D})\dagger}\mathbf{H}_j^{(\frac{L}{D})}\mathbf{g}_j}{\frac{P}{N}\mathbf{g}_j^\dagger\left(\mathbf{H}_j^\dagger\mathbf{H}_j - \mathbf{H}_j^{(\frac{L}{D})\dagger}\mathbf{H}_j^{(\frac{L}{D})}\right)\mathbf{g}_j + \frac{P}{N}\sum_{i=1,i\neq j}^{N}\mathbf{g}_j^\dagger\mathbf{H}_i^\dagger\mathbf{H}_i\mathbf{g}_j + P_n} \right)\right].$$

$$(2.10)$$

2.3 Time-Reversal Massive Multipath Effect

In this section, we derive a time-reversal massive multipath effect (TRMME) for the TR technique in a rich-scattering environment. Similar to the massive MIMO effect in massive MIMO given an excessive amount of antennas [42], the multipath profile of different users in the TR system will also be orthogonalized given massive independent multipaths. Considering the channel delay spread in wideband system, the channel matrix considered in the following is the combination of decimated Toeplitz matrices in (2.8).

Theorem 1 (Time-Reversal Massive Multipath Effect): Under the asymptotic setting where $K = K_{max} \to \infty$, the off-diagonal elements in the cor-

relation matrix of channels $\mathbf{Q}\mathbf{Q}^\dagger$ converge to zero in distribution, and

$$\frac{[\mathbf{Q}\mathbf{Q}^\dagger]_{l_j,l_j}}{\|\mathbf{h}_j\|^2} \xrightarrow{d} 1, \tag{2.11}$$

where $\mathbf{Q} = [\mathbf{H}_1^T, \mathbf{H}_2^T, \cdots, \mathbf{H}_N^T]^T$ and $\xrightarrow{d}$ represents the convergence in distribution.

Proof: In order to reveal all the observable multipaths, e.g., $K = K_{max}$, the bandwidth of the system W should be large enough so that $L/K_{max}^p \to c$ where c is a constant and $p > 2$. Notice that every element in $\mathbf{Q}\mathbf{Q}^\dagger$ is the sum of multiple independent variables, which converges to a Gaussian random variable in distribution in the asymptotical scenario based on the central limit theorem. Since Gaussian random variable is only determined by the first and second moment and obviously each element in $\mathbf{Q}\mathbf{Q}^\dagger$ has zero mean, we only need to prove the largest variance of off-diagonal element will converge to zero.

Based on the definition of $\mathbf{Q}$, we have

$$\mathbf{Q}\mathbf{Q}^\dagger = \begin{bmatrix} \mathbf{H}_1\mathbf{H}_1^\dagger & \mathbf{H}_1\mathbf{H}_2^\dagger & \cdots & \mathbf{H}_1\mathbf{H}_N^\dagger \\ \mathbf{H}_2\mathbf{H}_1^\dagger & \mathbf{H}_2\mathbf{H}_2^\dagger & \cdots & \mathbf{H}_2\mathbf{H}_N^\dagger \\ \vdots & \vdots & \ddots & \cdots \\ \mathbf{H}_N\mathbf{H}_1^\dagger & \mathbf{H}_N\mathbf{H}_2^\dagger & \cdots & \mathbf{H}_N\mathbf{H}_N^\dagger \end{bmatrix}. \tag{2.12}$$

With (2.12), we can directly obtain

$$\left[\mathbf{Q}\mathbf{Q}^\dagger\right]_{l_j,l_j} = \mathbf{H}_j^{(\frac{L}{D})}\mathbf{H}_j^{(\frac{L}{D})\dagger} = \|\mathbf{h}_j\|^2, \tag{2.13}$$

where $[\cdot]_{m,n}$ represents the element in the mth row and the nth column of the matrix.

Then, we prove that $\mathbf{Q}\mathbf{Q}^\dagger$ is diagonal by examining the off-diagonal elements.

Note that each off-diagonal matrix ($\forall i \neq j$) in (2.12), $\mathbf{H}_i\mathbf{H}_j^\dagger$, can be expanded as

$$\mathbf{H}_i\mathbf{H}_j^\dagger = \begin{bmatrix} \mathbf{H}_i^{(1)}\mathbf{H}_j^{(1)\dagger} & \mathbf{H}_i^{(1)}\mathbf{H}_j^{(2)\dagger} & \cdots & \mathbf{H}_i^{(1)}\mathbf{H}_j^{(\frac{2L-1}{D})\dagger} \\ \mathbf{H}_i^{(2)}\mathbf{H}_j^{(1)\dagger} & \mathbf{H}_i^{(2)}\mathbf{H}_j^{(2)\dagger} & \cdots & \mathbf{H}_i^{(2)}\mathbf{H}_j^{(\frac{2L-1}{D})\dagger} \\ \vdots & \vdots & \ddots & \cdots \\ \mathbf{H}_i^{(\frac{2L-1}{D})}\mathbf{H}_j^{(1)\dagger} & \mathbf{H}_i^{(\frac{2L-1}{D})}\mathbf{H}_j^{(2)\dagger} & \cdots & \mathbf{H}_i^{(\frac{2L-1}{D})}\mathbf{H}_j^{(\frac{2L-1}{D})\dagger} \end{bmatrix}. \tag{2.14}$$

From (2.14), we can see that each element of $\mathbf{H}_i\mathbf{H}_j^\dagger$, $\left[\mathbf{H}_i\mathbf{H}_j^\dagger\right]_{m,n} = \mathbf{H}_i^{(m)}\mathbf{H}_j^{(n)\dagger}$, is the sum of multiple independent random variables. Therefore, when K_{max} is sufficiently large, $\left[\mathbf{H}_i\mathbf{H}_j^\dagger\right]_{m,n}$ can be regarded as a Gaussian random variable, whose distribution is completely determined by the first and the second moments.

Based on the independence between the channel taps and distinct receivers, it is obvious that

$$\mathbb{E}\left[\mathbf{H}_i^{(m)}\mathbf{H}_j^{(n)\dagger}\right] = 0, \tag{2.15}$$

while the second moment can be upper bounded as follows

$$\begin{aligned} \mathbb{E}\left[|\mathbf{H}_i^{(m)}\mathbf{H}_j^{(n)\dagger}|^2\right] &\overset{(a)}{=} \sum_{l=1}^{L}\mathbb{E}\left[|\mathbf{H}_i^{(m)}(l)|^2|\mathbf{H}_j^{(n)}(l)|^2\right] \\ &\overset{(b)}{\leq} \sum_{l=1}^{L}\mathbb{E}\left[|\mathbf{H}_i^{(\frac{L}{D})}(l)|^2\right]\mathbb{E}\left[|\mathbf{H}_j^{(\frac{L}{D})}(l)|^2\right] \\ &\overset{(c)}{=} \frac{\left(\sum_{k=1}^{K_{max}}\sigma_k^2\right)^2}{L}, \end{aligned} \tag{2.16}$$

where (a) is obtained directly from the independence, (b) is based on the matrix structure in (2.8) and (c) comes from the fact that the K_{max} multipaths are randomly distributed among the L-tap channel and thus

$$\mathbb{E}\left[|h_j(m)|^2\right] = \mathbb{E}\left[|h_j(n)|^2\right] = \frac{\sum_{k=1}^{K_{max}}\sigma_k^2}{L}, \quad \forall m, n. \tag{2.17}$$

21

Note $\sum_{k=1}^{K_{max}} \sigma_k^2 < K_{max}$ due to the path loss attenuation. Therefore, (c) will converge to 0 given $L/K_{max}^p \to c$ where c is a constant and $p > 2$. From (2.15) and (2.16), we can conclude that

$$\left[\mathbf{H}_i \mathbf{H}_j^\dagger\right]_{m,n} \xrightarrow{d} 0, \quad \forall m, n, \text{ and } i \neq j. \tag{2.18}$$

Next, let us examine the diagonal submatrix of $\mathbf{QQ}^\dagger$, which can be expanded as

$$\mathbf{H}_j \mathbf{H}_j^\dagger = \begin{bmatrix} \mathbf{H}_j^{(1)}\mathbf{H}_j^{(1)\dagger} & \mathbf{H}_j^{(1)}\mathbf{H}_j^{(2)\dagger} & \cdots & \mathbf{H}_j^{(1)}\mathbf{H}_j^{(\frac{2L-1}{D})\dagger} \\ \mathbf{H}_j^{(2)}\mathbf{H}_j^{(1)\dagger} & \mathbf{H}_j^{(2)}\mathbf{H}_j^{(2)\dagger} & \cdots & \mathbf{H}_j^{(2)}\mathbf{H}_j^{(\frac{2L-1}{D})\dagger} \\ \vdots & \vdots & \ddots & \cdots \\ \mathbf{H}_j^{(\frac{2L-1}{D})}\mathbf{H}_j^{(1)\dagger} & \mathbf{H}_j^{(\frac{2L-1}{D})}\mathbf{H}_j^{(2)\dagger} & \cdots & \mathbf{H}_j^{(\frac{2L-1}{D})}\mathbf{H}_j^{(\frac{2L-1}{D})\dagger} \end{bmatrix}. \tag{2.19}$$

Similarly, each element $\left[\mathbf{H}_j \mathbf{H}_j^\dagger\right]_{m,n} = \mathbf{H}_j^{(m)}\mathbf{H}_j^{(n)\dagger}$ can be regarded as Gaussian variable when K_{max} is sufficiently large. Since $\mathbf{H}_j^{(m)}$ and $\mathbf{H}_j^{(n)}$ are independent when $m \neq n$, similar to (2.15) and (2.16), we can derive

$$\begin{cases} \mathbb{E}\left[\mathbf{H}_j^{(m)}\mathbf{H}_j^{(n)\dagger}\right] & = 0, \quad m \neq n, \\ \mathbb{E}\left[|\mathbf{H}_j^{(m)}\mathbf{H}_j^{(n)\dagger}|^2\right] & \leq \frac{(\sum_{k=1}^{K_{max}} \sigma_k^2)^2}{L}, \quad m \neq n, \end{cases} \tag{2.20}$$

and given $L/K_{max}^p \to c$ where c is a constant and $p > 2$, we have derived that

$$\left[\mathbf{H}_j \mathbf{H}_j^\dagger\right]_{m,n} \xrightarrow{d} 0, \quad \forall j, \text{ and } m \neq n. \tag{2.21}$$

Therefore, we can conclude that $\mathbf{QQ}^\dagger$ is diagonal. This completes the proof.

$\square$

Since $\mathbf{Q}$ is the combination of CSIs from the transmitter to N receivers, the term $\mathbf{QQ}^\dagger$ represents the correlation matrix of these N CSIs. Therefore, the derived
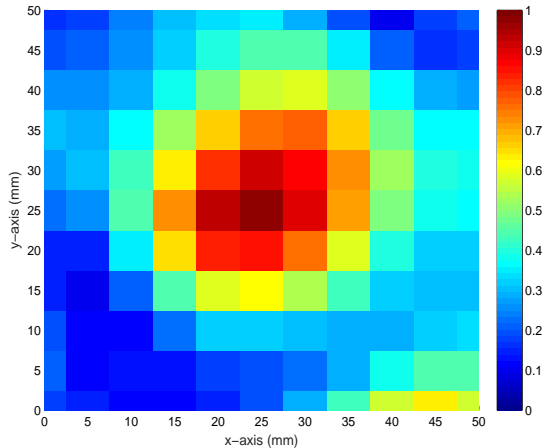
Figure 2.3: Spatial Focusing Ball with 125MHz Bandwidth.

TRMME implies that the CSIs to N receivers become orthogonal to each other under the rich-multipath setting. Based on the indoor measurements with the TR prototype in [67], TR with 125MHz bandwidth is capable to formulate a spatial focusing ball as shown in Fig. 2.3. With the derived TRMME, the focusing ball of TR naturally shrinks to a pinpoint in a rich-scattering environment with a sufficiently large bandwidth, which is also predicted and observed in the massive MIMO system. Therefore, the derived TRMME is a counterpart of the massive MIMO effect in indoor scenarios.

The assumption that $K_{max} \to \infty$ is just for analyzing the asymptotical achievable rate of the TR system as the assumption $M_t \to \infty$ in early massive MIMO works. In practice, we only need that K_{max} is large enough to achieve the massive multipath effect. Based on the real indoor measurement in Section 2.5.2, we have demonstrated that the number of the resolved multipaths in a typical indoor environment is large enough given a sufficiently large bandwidth. Even though K_{max}

is a fixed value given the power and environment, there still exist other methods to realize massive multipaths. Since the TR and MIMO technology are not mutually exclusive, the independent multipaths can be easily scaled up by adding a few antennas. How to realize massive multipaths is discussed with real indoor measurement later in Section 2.5. In the following, the asymptotic performance of TR technologies in a rich-scattering environment is derived based on the TRMME.

2.4 Expected Achievable Rate under Different Waveforms

In this section, we analyze the asymptotic rates of TR technology. First, we derive the expected achievable rate under typical waveforms: basic TR waveform [65], ZF waveform [15] and MMSE waveform [69]. Then, the asymptotical achievable rate with the three waveforms is further derived based on the TRMME derived in Section 2.3.

2.4.1 Expected Achievable Rate

The three waveforms are shown in the following,

$$
\mathbf{g}_j = \begin{cases}
\mathbf{H}_j^{(L/D)\dagger}/\|\mathbf{H}_j^{(L/D)}\|, & \text{Basic TR} \\[2mm]
c_{ZF}\mathbf{Q}^\dagger(\mathbf{Q}\mathbf{Q}^\dagger)^{-1}\mathbf{e}_{l_j}, & \text{ZF} \\[2mm]
c_{MMSE}(\mathbf{Q}^\dagger\mathbf{Q}+\frac{1}{p_u}\mathbf{I})^{-1}\mathbf{Q}^\dagger\mathbf{e}_{l_j}, & \text{MMSE}
\end{cases} \tag{2.22}
$$

where c_{ZF} and c_{MMSE} are normalization constants, $\mathbf{Q} = [\mathbf{H}_1^T, \mathbf{H}_2^T, \cdots, \mathbf{H}_N^T]^T$, $\mathbf{e}_{l_j}$ is an elementary vector with $l_j = (j-1)(2L-1)/D + L/D$, $\mathbf{I}$ is the identity matrix,

and p_u is the transmitting signal-to-noise ratio (SNR) of each user defined as

$$p_u = \frac{P}{NP_n}. \qquad (2.23)$$

With the definition of $\mathbf{Q}$ and $\mathbf{e}_{l_j}$ above, we have

$$\mathbf{Q}^\dagger \mathbf{e}_{l_j} = \mathbf{H}_j^{(L/D)\dagger}. \qquad (2.24)$$

Note that under the multipath-rich scenario, ZF waveform can completely cancel out the interference given a large amount of independent multipaths. In addition, MMSE waveform has a simpler closed form solution with the fixed dual uplink power allocation [69].

Considering the more and more power DSP and the small time consumption of channel probing, the overhead of channel probing and waveform design is ignored in the following achievable rate analysis.

Theorem 2 (Expected Achievable Rate): The expected achievable rate of the TR system with basic TR waveform, ZF waveform, and MMSE waveform can be written as follows

$$
\begin{aligned}
R_j^{Basic} &= \\
&\frac{W}{D}\mathbb{E}\left[\log_2\left(1 + \frac{p_u\|\mathbf{h}_j\|^4}{p_u([\mathbf{Q}\mathbf{Q}^\dagger\mathbf{Q}\mathbf{Q}^\dagger]_{l_j,l_j} - \|\mathbf{h}_j\|^4) + \|\mathbf{h}_j\|^2}\right)\right], \\
R_j^{ZF} &= \frac{W}{D}\mathbb{E}\left[\log_2\left(1 + \frac{p_u}{[(\mathbf{Q}\mathbf{Q}^\dagger)^{-1}]_{l_j,l_j}}\right)\right], \\
R_j^{MMSE} &= \frac{W}{D}\mathbb{E}\left[\log_2\left(\frac{1}{\left[(\mathbf{I} + p_u\mathbf{Q}\mathbf{Q}^\dagger)^{-1}\right]_{l_j,l_j}}\right)\right].
\end{aligned}
\qquad (2.25)
$$

Note that the equations in Theorem 2 are not in closed-form due to the general channel model assumed in this chapter. Theorem 2 serves as a starting point

to derive the asymptotical expected achievable rate, which will be shown in later sections. Even though (2.25) seems similar to those for MIMO MRC/ZF/MMSE receivers, the matrix $\mathbf{Q}$ is different from the channel profile matrix in MIMO system, which results in significantly different derivation of the asymptotical performance in the TR system. More specifically, due to the large channel delay spread in the TR system, there exists ISI. Therefore, backoff factor D is adopted in our chapter and the channel profile $\mathbf{H}_i$ becomes the decimated Toeplitz matrix, which is much more complicated than that in MIMO system. Furthermore, it is the first work analyzing the asymptotical achievable rate for TR system with various waveform design methods with considering the ISI in practical system.

From Theorem 2, we can see that the expressions of expected achievable rate under different waveforms are closely related to $\mathbf{Q}\mathbf{Q}^\dagger$ and $\left[\mathbf{Q}\mathbf{Q}^\dagger\mathbf{Q}\mathbf{Q}^\dagger\right]_{l_j,l_j}$. Actually, the asymptotical property of $\mathbf{Q}\mathbf{Q}^\dagger$ has been studied previously as the TRMME. In the following section, we will further explore the property of $\left[\mathbf{Q}\mathbf{Q}^\dagger\mathbf{Q}\mathbf{Q}^\dagger\right]_{l_j,l_j}$ under a massive multipath setting, i.e., when $K_{max} \to \infty$, and study the corresponding asymptotic expected achievable rates with different waveforms.

2.4.2 Asymptotic Performance

We derive the asymptotic property of $\left[\mathbf{Q}\mathbf{Q}^\dagger\mathbf{Q}\mathbf{Q}^\dagger\right]_{l_j,l_j}$ in the following Lemma.

Lemma 1: Under the asymptotic setting where $K = K_{max} \to \infty$, we have

$$\limsup_{K_{max}\to\infty} \frac{\left[\mathbf{Q}\mathbf{Q}^\dagger\mathbf{Q}\mathbf{Q}^\dagger\right]_{l_j,l_j} - \|\mathbf{h}_j\|^4}{\sum_{k=1}^{K_{max}} \sigma_k^2} = \alpha, \tag{2.26}$$

where $\alpha = 2N/D$.

Proof: With the definition of $\mathbf{Q}$ and (2.9), we have

$$\left[\mathbf{Q}\mathbf{Q}^\dagger\mathbf{Q}\mathbf{Q}^\dagger\right]_{l_j,l_j} - \|\mathbf{h}_j\|^4 = \sum_{i=1,i\neq j}^{N} \sum_{l=1}^{(2L-1)/D} |\mathbf{H}_i^{(l)}\mathbf{H}_j^{(\frac{L}{D})\dagger}|^2 + \sum_{l=1,l\neq(L/D)}^{(2L-1)/D} |\mathbf{H}_j^{(l)}\mathbf{H}_j^{(\frac{L}{D})\dagger}|^2,$$

(2.27)

which is the sum of multiple independent random variables. Therefore, $\left[\mathbf{Q}\mathbf{Q}^\dagger\mathbf{Q}\mathbf{Q}^\dagger\right]_{l_j,l_j} -$

$\|\mathbf{h}_j\|^4$ can be regarded as a Guassian random variable when K_{max} is sufficiently large.

Similar to (2.16), we have the following

$$\begin{cases} \mathbb{E}\left[|\mathbf{H}_i^{(l)}\mathbf{H}_j^{(\frac{L}{D})\dagger}|^2\right] & \leq \frac{(\sum_{k=1}^{K_{max}}\sigma_k^2)^2}{L}, \quad i \neq j, \\[2mm] \mathbb{E}\left[|\mathbf{H}_j^{(l)}\mathbf{H}_j^{(\frac{L}{D})\dagger}|^2\right] & \leq \frac{(\sum_{k=1}^{K_{max}}\sigma_k^2)^2}{L}, \quad l \neq (L/D). \end{cases}$$

(2.28)

Therefore, with $K_{max} \to \infty$, the expectation of $\left[\mathbf{Q}\mathbf{Q}^\dagger\mathbf{Q}\mathbf{Q}^\dagger\right]_{l_j,l_j} - \|\mathbf{h}_j\|^4$ can be

bounded by

$$\mathbb{E}\left[\left[\mathbf{Q}\mathbf{Q}^\dagger\mathbf{Q}\mathbf{Q}^\dagger\right]_{l_j,l_j} - \|\mathbf{h}_j\|^4\right] \leq \frac{N(2L-1)}{D}\frac{(\sum_{k=1}^{K_{max}}\sigma_k^2)^2}{L} \leq \alpha\left(\sum_{k=1}^{K_{max}}\sigma_k^2\right)^2, \quad (2.29)$$

with $\alpha = 2N/D$.

Similar to the argument in the derivation of (2.17), the fourth moment of

$h_j(m)$ can be given as

$$\mathbb{E}\left[|h_j(m)|^4\right] = \mathbb{E}\left[|h_j(n)|^4\right] = 2\left(\frac{\sum_{k=1}^{K_{max}}\sigma_k^2}{L}\right)^2, \quad \forall m, n. \qquad (2.30)$$

Then, we have,

$$\begin{cases} \mathbb{E}\left[|\mathbf{H}_i^{(l)}\mathbf{H}_j^{(\frac{L}{D})\dagger}|^4\right] & \leq \frac{4(\sum_{k=1}^{K_{max}}\sigma_k^2)^4}{L^3}, \quad i \neq j, \\[2mm] \mathbb{E}\left[|\mathbf{H}_j^{(l)}\mathbf{H}_j^{(\frac{L}{D})\dagger}|^4\right] & \leq \frac{4(\sum_{k=1}^{K_{max}}\sigma_k^2)^4}{L^3}, \quad l \neq (L/D). \end{cases}$$

(2.31)

As $K_{max} \to \infty$, $L/K_{max}^p \to c$ where c is a constant and $p > 2$ holds in the

multipath-rich scenario. Therefore, the variance of $\left[\mathbf{Q}\mathbf{Q}^\dagger\mathbf{Q}\mathbf{Q}^\dagger\right]_{l_j,l_j} - \|\mathbf{h}_j\|^4$ goes to

27

zero as $K_{max} \to \infty$. Combining the first moment in (2.29), we can derive the result in Lemma 1. This completes the proof. $\qquad\qquad\qquad\qquad\qquad\qquad\qquad\qquad\square$

Remark: In a massive MIMO system, when the number of antennas grows large, the random channel vectors between the users and the base station become pairwisely orthogonal [60]. Similarly, in a TR system, when the number of multipaths grows, the random channel vectors between the receivers and the transmitter are also pairwise orthogonal, as shown in the TRMME. Different from the matched filter beamforming in massive MIMO system, basic TR waveform cannot completely remove the interference due to the channel delay spread in the wideband system. Therefore, the analysis of interference in Lemma 1 is needed for the derivation of the asymptotic expected achievable rate with basic TR waveform.

Based on the TRMME and Lemma 1, we can analyze the asymptotic expected achievable rate under different waveforms, and the results are summarized in the following Theorem.

Theorem 3: When $K_{max} \to \infty$, the asymptotic expected achievable rate with the ZF waveform and MMSE waveform satisfy that

$$\lim_{K_{max} \to \infty} \frac{R_j^{ZF}}{W/D} = \lim_{K_{max} \to \infty} \frac{R_j^{MMSE}}{W/D} = \mathbb{E}\left[\log_2\left(1 + p_u \|\mathbf{h}_j\|^2\right)\right], \qquad (2.32)$$

while the asymptotic expected achievable rate with the basic TR waveform satisfies the following equation,

$$\liminf_{K_{max} \to \infty} \frac{R_j^{Basic}}{W/D} = \mathbb{E}\left[\log_2\left(1 + \frac{p_u \|\mathbf{h}_j\|^2}{\frac{p_u \alpha \left(\sum_{k=1}^{K_{max}} \sigma_k^2\right)^2}{\|\mathbf{h}_j\|^2} + 1}\right)\right]. \qquad (2.33)$$

28

Proof: According to the TRMME, we have

$$\frac{\left[\left(\mathbf{Q}\mathbf{Q}^\dagger\right)^{-1}\right]_{l_j,l_j}}{\|\mathbf{h}_j\|^2} \xrightarrow{d} 1, \tag{2.34}$$

since the inverse of a diagonal matrix should be diagonal.

Then, according to (2.25), the asymptotic expected achievable rate under ZF waveform is

$$\lim_{K_{max}\to\infty}\frac{R_j^{ZF}}{W/D} = \mathbb{E}\left[\log_2\left(1 + p_u\|\mathbf{h}_j\|^2\right)\right]. \tag{2.35}$$

Similarly, with the TRMME, we can also have

$$\left[\left(\mathbf{I} + p_u\mathbf{Q}\mathbf{Q}^\dagger\right)^{-1}\right]_{l_j,l_j} \xrightarrow{d} \left[(\mathbf{I} + p_u\lambda)^{-1}\right]_{l_j,l_j}$$
$$= \frac{1}{1 + p_u\|\mathbf{h}_j\|^2}. \tag{2.36}$$

By substituting (2.36) into (2.25), the asymptotic expected achievable rate under MMSE waveform is

$$\lim_{K_{max}\to\infty}\frac{R_j^{MMSE}}{W/D} = \mathbb{E}\left[\log_2\left(1 + p_u\|\mathbf{h}_j\|^2\right)\right]. \tag{2.37}$$

Finally, by substituting (2.26) of Lemma 1 into (2.25), the asymptotic expected achievable rate under basic TR waveform can be lower bounded as

$$\liminf_{K_{max}\to\infty}\frac{R_j^{Basic}}{W/D} = \mathbb{E}\left[\log_2\left(1 + \frac{p_u\|\mathbf{h}_j\|^2}{\frac{p_u\alpha\left(\sum_{k=1}^{K_{max}}\sigma_k^2\right)^2}{\|\mathbf{h}_j\|^2} + 1}\right)\right]. \tag{2.38}$$

This completes the proof. □

From Theorem 3, we can see that the ZF and MMSE waveforms generally outperform the basic TR waveform in terms of expected achievable rate. However, when D is sufficiently large so that $\frac{\alpha\left(\sum_{k=1}^{K_{max}}\sigma_k^2\right)^2}{\|\mathbf{h}_j\|^2}$ goes to zero, this is the case when the ISI and IUI are eliminated, then the basic TR waveform can achieve the same asymptotic expected achievable rate with ZF and MMSE waveforms.
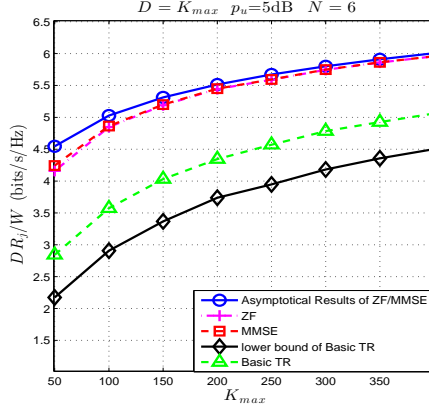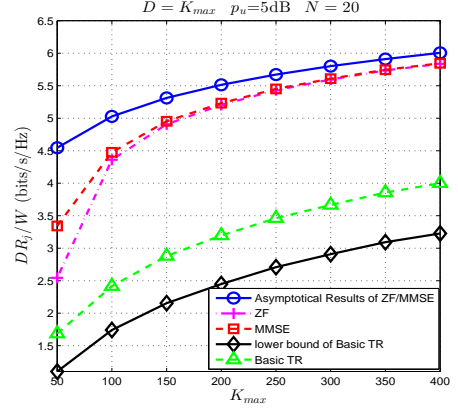
(a) $N = 6$.   (b) $N = 20$.

Figure 2.4: Comparison between the asymptotic performance with varying N, with $D = K_{max}$ and $p_u = 5$dB.

2.5   Simulations and Experiments

In this section, we conduct simulations and experiments to evaluate the expected asymptotical performance of a TR system under various settings. We assume that the N receivers are uniformly, randomly distributed and share the same channel model, which is discussed in Section 2.2. Since more received power will be captured within the multipath-rich environment, we assume the expected channel gain as an increasing function of the number of independent multipaths K_{max}.

2.5.1   Asymptotical Performance

We first validate our theoretical analysis in Theorem 3. The y-axis is DR_j/W, where R_j is the expected achievable rate of the jth receiver, D is the backoff factor and W is the system bandwidth. Since the channel gain is assumed to be an increasing function of K_{max}, the asymptotical performance would increase with K_{max} as
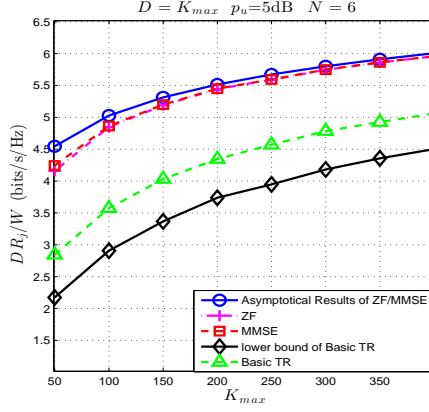
(a) $D = K_{max}$.
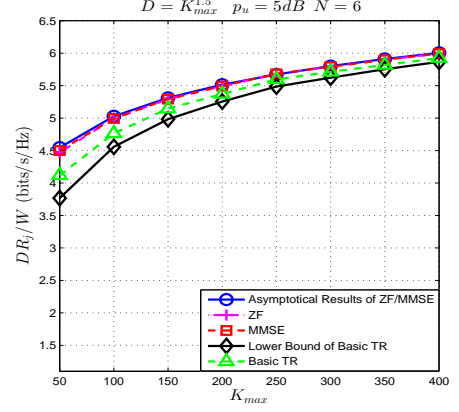
(b) $D = K_{max}^{1.5}$.

Figure 2.5: Comparison between the asymptotic performance with varying D, with $N = 6$ and $p_u = 5$dB.

well. The case when D is not sufficiently large, e.g., $D = K_{max}$ is first investigated. The expected asymptotical performance of each receiver is shown in Fig. 2.4 with $p_u = 5$dB and different N. From Fig. 2.4, we can observe that the performance using ZF and MMSE waveforms converges to the same limit quickly as K_{max} increases. Also, there is a gap between the asymptotic limit of ZF/MMSE waveform and the lower bound of the basic TR waveform. This is mainly because when the basic TR waveform is used and the D is not large enough, there exists residual ISI and IUI and $\frac{\alpha\left(\sum_{k=1}^{K_{max}} \sigma_k^2\right)^2}{\|\mathbf{h}_j\|^2}$ cannot be negligible. By comparing the results with $N = 6$ and $N = 20$, we notice that the gap becomes even larger when N increases, which is due to the increase of $\alpha = 2N/D$.

We also compare the asymptotical performance of basic TR, ZF and MMSE waveforms by varying D. It can be seen in Fig. 2.5 that the gap between the asymptotic performance of ZF/MMSE waveform and that of the basic TR waveform

becomes much smaller when D and K_{max} are both sufficiently larger. Such a phenomenon is mainly due to less severe ISI and IUI and a much smaller $\frac{\alpha\left(\sum_{k=1}^{K_{max}} \sigma_k^2\right)^2}{\|\mathbf{h}_j\|^2}$. Therefore, the basic TR waveform can achieve the same optimal asymptotic expected achievable rate with ZF and MMSE waveforms with sufficiently large D.

Note that p_u is fixed as 5dB in the simulations, which implies that the trend in Fig. 2.4 and Fig. 2.5 also applies to the energy efficiency. In other words, the energy efficiency of the TR system increases with K_{max}.

2.5.2 The Number of Observable Independent Multipaths K in a Typical Indoor Environment

To achieve the asymptotic performance in Theorem 3 requires the TR system to operate in a multipath-rich environment. In this subsection, we investigate the property of K in a typical indoor environment using real-world measurements. First, we demonstrate that, in a typical office, the number of resolvable multipaths is large with a sufficiently large bandwidth. Then, the approach to increase K_{max} is further discussed and validated through real measurements.

We use two Universal Software Radio Peripherals (USRPs) as channel sounders to probe the channel in a typical office room, whose floor plan is shown in Fig. 2.6. As shown in the figure, TX is placed on a grid structure with 5cm resolution and RX is placed at the corner. With two USRPs, we scan the spectrum, e.g., from 4.9GHz to 5.9GHz, to acquire the channel impulse response with a bandwidth of 10MHz-1GHz.
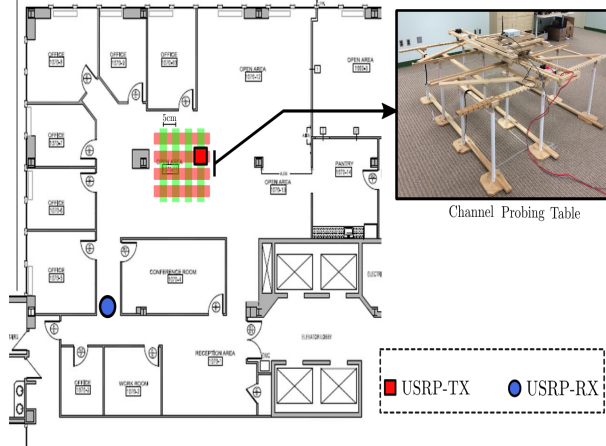
Figure 2.6: Floor Plan and Experiment Setting

We employ eigenvalue analysis to determine the value of K for any given bandwidth W. First, we estimate the covariance matrix of the measured channels $\mathbf{K}_{h,W}$ using statistical averaging

$$\mathbf{K}_{h,W} = \frac{1}{N} \sum_{i=1}^{N} \mathbf{h}_{i,W} \mathbf{h}_{i,W}^{\dagger}, \tag{2.39}$$

where $\mathbf{h}_{i,W}$ is the channel information obtained at location i with bandwidth W and $N = 100$. Since $\mathbf{K}_{h,W}$ is Hermitian and positive definite, there exists a unitary matrix U such that

$$\mathbf{K}_{h,W} = U\Lambda U^{\dagger} = \sum_{i=1}^{L} \lambda_{i,W} \psi_i \psi_i^{\dagger}, \tag{2.40}$$

where $\lambda_{1,W} \geq \lambda_{2,W} \geq \cdots \geq \lambda_{L,W}$ and $L = \tau_C W$.

In Fig. 2.7, we show the percentage of the captured energy E_l versus the number of significant eigenvalues l, with E_l defined as $E_l = \frac{\sum_{i=1}^{l} \lambda_i}{\sum_{i=1}^{L} \lambda_i}$. From Fig. 2.7, we can see that the channel energy is concentrated in a small number of eigenvalues when the bandwidth is small, while spread over a large number of eigenvalues as the bandwidth increases. In other words, the degree of freedom K increases as

33
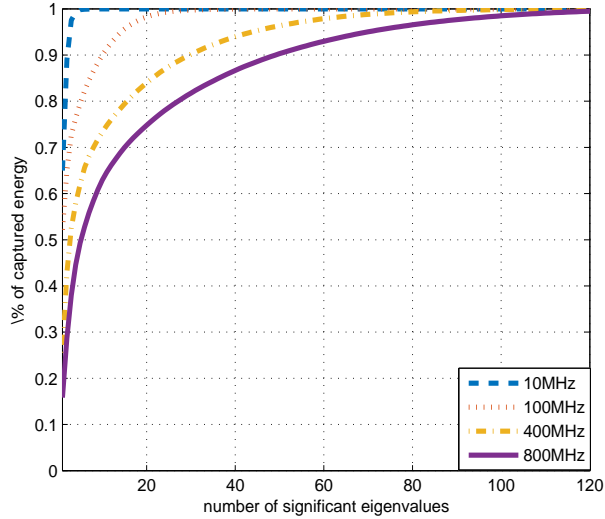
Figure 2.7: Percentage of captured energy versus the number of significant eigen-values with a single antenna

the bandwidth W increases. This is further confirmed in Fig. 2.8, where we show the number of significant eigenvalues versus the channel bandwidth by fixing the captured energy at 98%.

From previous measurements, K_{max} is a large value in a typical indoor environment. Now we discuss an approach to further increase K_{max} in practical environment. Since the TR and MIMO technology are not mutually exclusive, the degree of freedom can be further scaled up by deploying a couple antennas to harvest hundreds of virtual antennas as shown in Fig. 2.8. As indicated in the figure, it would be easy to realize massive virtual antennas with a few antennas in the TR system instead of installing hundreds of physical antennas.
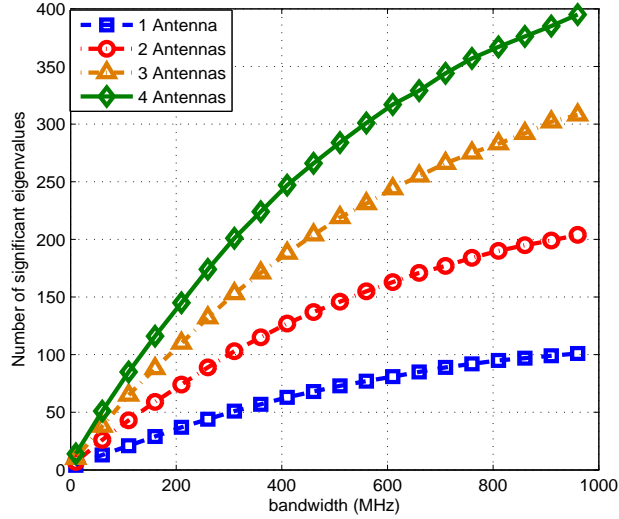
Figure 2.8: Number of significant eigenvalues K at different bandwidth W

2.5.3 Achievable Rate Evaluation

The assumption that $K_{max} \to \infty$ is just for analyzing the asymptotical achievable rate of the TR system as the assumption $M_t \to \infty$ in early massive MIMO works. In practice, we only need that K_{max} is large enough to achieve massive multipath effect. In the following, we will demonstrate that even with a single antenna, TR wideband system is still capable to reach a promising achievable rate based on our indoor experiment. Our experiment is conducted with the real indoor channel measurement and the achievable rate in TR system is calculated based on Theorem 2.

We first evaluate the expected achievable rate of the TR system in a typical indoor environment using the channel measurements in the previous subsection, with $W = 1\text{GHz}$. Then we compare the performance of the TR system with that of a massive MIMO system. Clearly, there is a tradeoff in selecting a proper D: W/D
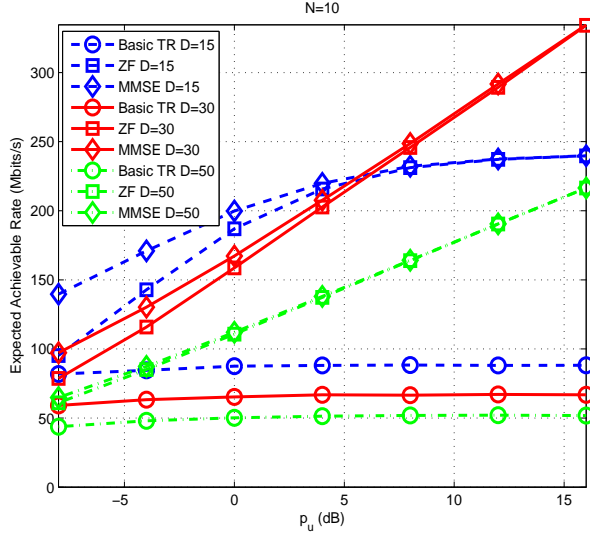
Figure 2.9: Expected achievable rate by varying the backoff factor D, with $N = 10$ and $W = 1\text{GHz}$.

will decrease as D increases, while both the ISI and IUI get reduced as D increases. In Fig. 2.9 we show the the expected achievable rate of different waveforms with different D.

We can see that the expected achievable rate of the basic TR waveform saturates quickly as p_u increases because it is interference-limited with $N = 10$ receivers. Increasing D may decrease the expected achievable rate for the basic TR waveform if the decrease in W/D dominates the increase in SINR for a relatively large D as shown in Fig. 2.9. The expected achievable rates of ZF and MMSE waveforms also saturate at high p_u with $D = 15$, but can be improved by increasing D, e.g. $D = 30$, to reduce the interference. However, it may hurt the rate performance if we increase D too much, e.g., $D = 50$.

We choose $D = 30$ as the backoff factor used in the TR system to evaluate the
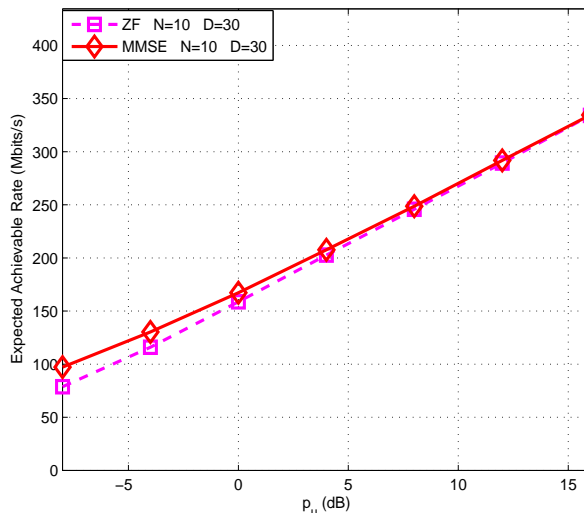
Figure 2.10: Expected achievable rate evaluation for TR system, with $W = 1\text{GHz}$, $N = 10$ and $D = 30$.

achievable rate in a practical indoor environment, as shown in Fig. 2.10, which is comparable to a 20MHz massive MIMO system with around 500 transmit antennas. Note that TR technology pays the price of spectral efficiency loss for the low cost and complexity implementation for indoor communications. For example, as shown in Fig. 2.11 [67], the TR prototype is a customized software defined radio (SDR) platform for designing and deploying TR-based communication systems. The size of the radio is 5cm by 17cm by 23cm, the weight is about 400g, and the power consumption is 25W. Compared with the massive MIMO prototype built in [63], the complexity and operation power consumption are obviously much lower. Considering the potential wide bandwidth available in future (e.g., UWB and mmWave band), the complexity, energy consumption and other metrics become more and more important compared with the spectral efficiency in indoor scenarios, which

Figure 2.11: TR Prototype

makes the TR technology a promising candidate for indoor communication.

2.6   Conclusion

In this chapter, we demonstrate that the TR technology, through harvesting the naturally existing virtual antennas, can offer a cost effective solution to realize the massive multipath effect, which is a counterpart of massive MIMO effect in indoor scenarios. With the derived massive multipath effect, we further derive the asymptotic rates of TR technology in a rich-scattering environment. We validate with simulations that the TR system with typical waveforms can asymptotically achieve the limiting achievable rate, where the interference is completely eliminated. Finally, based on the real channel measurements, it is shown that the single-antenna TR wideband system can achieve promising rates in a practical indoor environment.

Chapter 3

How Much Bandwidth is Needed?

As claimed in Chapter 2, even though the benefits of massive MIMO seem very promising, considering the requirement of deploying a large amount of antennas, massive MIMO system may be not feasible in indoor scenarios, where 95% of data traffic will come from [50]. As demonstrated in Chapter 2, Time-Reversal (TR) can achieve superior focusing effect in spatial-temporal domain by realizing the massive multipath effect, resulting in the promising performance as an indoor communication candidate for 5G.

As introduced in Chapter 2, the massive multipath effect and thus the performance of TR communication relies on the ability of resolving the many multipaths naturally existing in the environment. Based on the indoor experiment results in Fig. 2.8, a large bandwidth is required in the TR systems to reveal the multipaths with a better time resolution. For TR technology, it may use the spectrum utilized by ultra-wide-band (UWB) or mmWave band. Based on the existing study at high frequencies, there still exists a large amount of multipaths, which is essential for TR communication. For example, based on the building penetration and reflection measurements of 28GHZ in NYC [54], the RF energy is mostly retained within buildings due to low attenuation and high reflection through indoor materials. Moreover, the

delay spread for indoor 60GHz channels ranges between 30ns and 70ns [57], which indicates a multipath-rich environment.

Even though mmWave band may be utilized by TR communication in future, the spectrum is still a scarce resource with its own cost, and there is no existing work studying how much bandwidth is needed by TR communication to optimize its spectral efficiency. In this chapter, we explore this question by investigating the spectral efficiency of a Time-Reversal Division Multiple Access (TRDMA) system with multiple antennas and varying bandwidths. The optimal bandwidth for the system is defined as the bandwidth required to achieve the maximum spectral efficiency given the number of users N and backoff factor D. We first establish an equivalent multi-tap channel model for the system with varying bandwidths based on the real channel measurement in a typical indoor environment as discussed in Section 2.5.2. By evaluating the spectral efficiency of the TRDMA system with varying bandwidths and different waveform types (e.g., basic TR waveform and zero-forcing waveform), we find that the optimal bandwidth for TR communication is determined by the number of users N and backoff factor D instead of the waveform types. More specifically, the optimal bandwidth for the system increases with D when D is small, while increases with N when D is large. Even though the optimal bandwidth for a TR system can obtained through examining the spectral efficiency, a sub-optimal bandwidth is derived later based on the rank condition of the channel matrix, which is much easier to acquire than evaluating the spectral efficiency. Simulation results validate our theoretical analysis and show that the sub-optimal bandwidth is very close to the optimal one when D is small.

The rest of the chapter is organized as follows. In Section 3.1, the system model of the TR communication system is introduced in detail, where the channel model with varying bandwidths is established. The optimal bandwidth for the TRDMA system is investigated for both basic TR waveform and zero-forcing waveform in Section 3.2. Based on the rank condition of the channel matrix, a sub-optimal bandwidth is derived in the end of Section 3.2. In Section 3.3, simulation results are shown to validate our theoretical analysis. Finally, we draw the conclusion in Section 3.4.

3.1   System Model

In this section, we will first introduce the system architecture of the time-reversal division multiple access system with multiple antennas (TRDMA-MA system) [28]. Then, we describe the two phases of the communication in the TRDMA-MA system. Finally, the expression of the effective signal-to-interference-plus-noise ratio (SINR) of the proposed system is derived, based on which the uplink individual spectral efficiency is derived in Section 3.2.

A typical TRDMA-MA uplink system is shown in Fig. 3.1, where N terminal devices (TDs) simultaneously transmit signal to the access point (AP) equipped with M antennas. The emitted signal propagates through the multipath channels $\mathbf{h}_i^{(m)}$'s and arrives at the AP, where $\mathbf{h}_i^{(m)}$ represents the multipath channel between the ith TD and the mth antenna at the AP.

To handle the inter-symbol-interference (ISI) due to the multipath channel
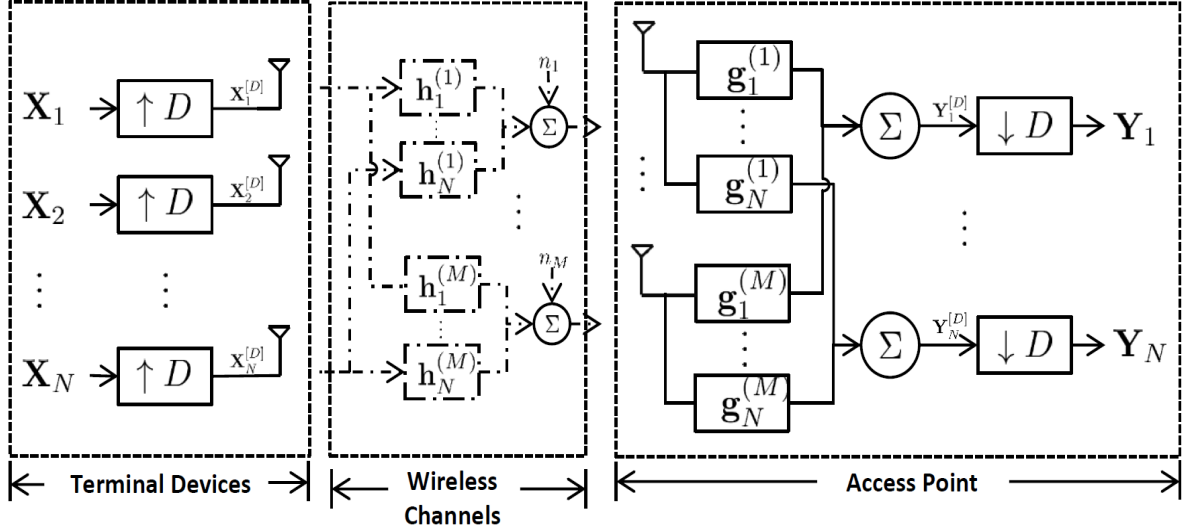
Figure 3.1: The diagram of TRDMA-MA uplink system.

profile, a backoff factor D is adopted in the system. Regarding the inter-user-interference (IUI) suppression, $\mathbf{g}_i^{(m)}$'s are the equalizers designed based on the multipath channels $\mathbf{h}_i^{(m)}$'s as shown in in Fig. 3.1.

3.1.1 Channel Model

The performance of TR communications inherently depends on the rich number of resolved independent taps in the channel impulse response (CIR), which is utilized to enable the multiple access of the TDs. Instead of deploying the massive number of antennas like massive MIMO system, TR technique tries to harvest the naturally existing multipaths in the environment with a large bandwidth. In the following, we first illustrate the relationship between the number of resolved independent multipaths and the system bandwidth. Then, a channel model with varying bandwidths is established for later theoretical analysis in this chapter.

Suppose there are totally K_{max} independent multipaths from the ith TD to the mth antenna at the AP, then the channel $h_i^{(m)}(t)$ can be written as

$$h_i^{(m)}(t) = \sum_{k=1}^{K_{max}} h_{i,k}^{(m)} \delta(t - \tau_k), \tag{3.1}$$

where $h_{i,k}^{(m)}$ and τ_k are the complex channel gain and path delay of the kth path, respectively. Without loss of generality, we assume that $\tau_1 = 0$, and as a result, the delay spread of channel is given by $\tau_C = \tau_{K_{max}}$.

Constrained by the limited bandwidth W of practical communication systems, pulse shaping filters are typically used to limit the effective bandwidth of transmission. Generally, the duration of the pulse T_p is limited by the available bandwidth W through the relation $T_p = 1/W$. Therefore, the equivalent channel response for a system with a limited bandwidth W can be expressed as

$$\widetilde{h}_i^{(m)}(t) = \int_{t-T_p}^t p(t-\tau) h_i^{(m)}(\tau) d\tau, \quad 0 \le t \le \tau_C + T_p \tag{3.2}$$

From (3.2), one can see that for those paths whose time differences are less than T_p, they are mixed together due to the limited bandwidth W. In other words, these paths are treated like one path in the equivalent CIR in the system.

According to the analysis, we propose a channel model as follows

$$h_{i,l}^{(m)} \sim \mathbf{CN} \left(0, \frac{e^{-\frac{\alpha}{L}l}}{\sum_{l=1}^{L} e^{-\frac{\alpha}{L}l}} \right) \tag{3.3}$$

where L is the number of resolved independent taps given the bandwidth W and α is a constant determined by the environment. Note that L is determined by the bandwidth through $L = \mathbf{f}(W)$ and $\mathbf{f}$ is a one-to-one mapping given a certain range of W, which can be curve fitted by the experiment results in Fig. 2.8.

From (3.3), it is observed that the overall expect channel gain $\mathbb{E}\left[\mathbf{h}_i^{(m)}\right]$ remains the constant for the varying W and thus L. Moreover, the larger the L, the smaller the decay for two taps in (3.3) due to the better time resolution.

For ease of notation in the theoretical analysis, we explore to find the optimal L^* in the following analysis and the corresponding optimal W^* can be obtained through the inverse mapping of $\mathbf{f}$.

3.1.2 Channel Probing Phase

Prior to the data transmission, N TDs first take turn to transmit an impulse signal, which in practice is a modified raised-cosine signal depending on the system bandwidth. The AP estimates the channel response $\mathbf{h}_i^{(m)}$ of each antenna for the ith TD, and we assume the perfect channel estimation in this chapter.

Upon acquiring all the $\mathbf{h}_i^{(m)}$'s of each link, different designed equalizers $\mathbf{g}_i^{(m)}$'s (e.g. basic TR waveform [65] and ZF waveform [15]) can be deployed at the AP side. According to the asymmetric system architecture, these waveforms serve as the equalizers in the uplink transmission phase as shown in Fig. 3.1.

3.1.3 Uplink Transmission Phase

Denote $\{\mathbf{X}_i\}$ as the sequence of information symbols at the ith TD to be transmitted to the AP. To suppress the ISI as well as match the symbol rate with chip rate, a backoff factor D is introduced by inserting $(D-1)$ zeros between two

symbols [22, 28, 65], i.e.,

$$X^{[D]}[k] = \begin{cases} X[k/D], & \text{if } (k \bmod D) = 0 \\ \\ 0, & \text{if } (k \bmod D) \neq 0. \end{cases} \tag{3.4}$$

where $(\cdot)^{[D]}$ denotes the D-times upsampling. The upsampled information symbols of the N TDs are transmitted out through the multipath channel and are added together at the AP. For instance, the signal received at the mth antenna of the AP is represented as follows

$$S_m[k] = \sum_{i=1}^{N} \left(\mathbf{X}_i^{[D]} * \mathbf{h}_i^{(m)} \right)[k] + n_m[k] \tag{3.5}$$

where $\mathbf{n}_m$ is an additive Gaussian noise at the mth antenna.

The equalized symbols for the ith TD are combined over the M antennas as

$$Y_i^{[D]}[k] = \sum_{m=1}^{M} \left(\sum_{i=1}^{N} \left(\mathbf{X}_i^{[D]} * \mathbf{h}_i^{(m)} \right) * \mathbf{g}_i^{(m)} \right)[k] + \widetilde{n}_i[k] \tag{3.6}$$

where $\{\widetilde{n}_i[k]\}$ is the equivalent AWGN with zero mean and variance σ^2.

Finally, $\mathbf{Y}_i^{[D]}$ is downsampled with the same factor D, ending up with $\mathbf{Y}_i$ given as follows

$$Y_i[k] = \sum_{m=1}^{M} \sum_{j=1}^{N} \sum_{l=1}^{(2L-1)/D} \left(\mathbf{h}_j^{(m)} * \mathbf{g}_i^{(m)} \right)[Dl]X_i[k-l] + n_i[k] \tag{3.7}$$

where $n_i[k] = \widetilde{n}_i[Dk]$. The information symbols $\mathbf{X}_i$ for the ith TD is estimated through $\mathbf{Y}_i$.

3.1.4 Effective SINR

By replacing the convolution with inner product, (3.7) can be rewritten as follows

$$
\begin{aligned}
Y_i[k] = {} & \sum_{m=1}^{M} \left(\mathbf{H}_{m,i}^{(\frac{L}{D})} \mathbf{g}_{m,i} \right) X_i[k - \frac{L}{D}] \quad (Signal) \\
& + \sum_{m=1}^{M} \left(\sum_{l=1, l \neq L/D}^{(2L-1)/D} \mathbf{H}_{m,i}^{(l)} \mathbf{g}_{m,i} \right) X_i[k - l] \quad (ISI) \\
& + \sum_{m=1}^{M} \sum_{j=1, j \neq i}^{N} \left(\sum_{l=1}^{(2L-1)/D} \mathbf{H}_{m,j}^{(l)} \mathbf{g}_{m,i} \right) X_j[k - l] \quad (IUI) \\
& + n_i[k] \quad (Noise)
\end{aligned}
\tag{3.8}
$$

where $\mathbf{H}_{m,i}^{(l)}$ is the lth row of the $(2L-1)/D \times L$ matrix $\mathbf{H}_{m,i}$ that is decimated by rows of a Toeplitz matrix as shown in (3.9).

$$
\mathbf{H}_{m,i} =
$$

$$
\begin{pmatrix}
h_i^{(m)}[D] & h_i^{(m)}[D-1] & \cdots & h_i^{(m)}[1] & 0 & \cdots & \cdots & 0 \\
h_i^{(m)}[2D] & h_i^{(m)}[2D-1] & \cdots & \cdots & h_i^{(m)}[1] & 0 & \cdots & 0 \\
\vdots & \vdots & \ddots & \ddots & \ddots & \ddots & \ddots & \vdots \\
h_i^{(m)}[L] & h_i^{(m)}[L-1] & \cdots & \cdots & \cdots & \cdots & \cdots & h_i^{(m)}[1] \\
\vdots & \vdots & \ddots & \ddots & \ddots & \ddots & \ddots & \vdots \\
0 & \cdots & 0 & h_i^{(m)}[L] & \cdots & \cdots & h_i^{(m)}[L-D+1] & h_i^{(m)}[L-2D] \\
0 & \cdots & \cdots & 0 & h_i^{(m)}[L] & \cdots & h_i^{(m)}[L-D+1] & h_i^{(m)}[L-D]
\end{pmatrix} ,
\tag{3.9}
$$

Consequently, the effective SINR [37,44] of the ith TD can be derived as shown in (3.10),

$$SINR_i =$$

$$\frac{\rho \mathbb{E}\left[\left|\sum_{m=1}^{M}\left(\mathbf{H}_{m,i}^{(\frac{L}{D})}\mathbf{g}_{m,i}\right)\right|^2\right]}{\rho \mathbb{E}\left[\sum_{l=1,l\neq L/D}^{(2L-1)/D}\left|\sum_{m=1}^{M}\left(\mathbf{H}_{m,i}^{(l)}\mathbf{g}_{m,i}\right)\right|^2\right] + \rho \mathbb{E}\left[\sum_{j=1,j\neq i}^{N}\sum_{l=1}^{(2L-1)/D}\left|\sum_{m=1}^{M}\mathbf{H}_{m,j}^{(l)}\mathbf{g}_{m,i}\right|^2\right] + 1}, \tag{3.10}$$

where $\rho = \mathbb{E}[|X_i[k]|^2]/\sigma^2$ is the signal-to-noise ratio (SNR).

Based on (3.10), the effective SINR of the ith TD depends not only on N and D but also L, which is closely related to the system bandwidth. The relationship between the number of resolved independent multipath L and system bandwidth is previously discussed in Section 2.5.2.

3.2 Optimal Bandwidth for Best Spectral Efficiency

Based on the channel model as shown in (3.3), there exists a one-to-one mapping between W and L. Therefore, the bandwidth plays a significant role in determining the individual spectral efficiency of the TRDMA-MA system as shown in (3.10).

The spectral efficiency of the ith TD in the TRDMA-MA system is defined as

$$R_i \triangleq \frac{1}{D}\log(1 + SINR_i), \tag{3.11}$$

which is an increasing function of $SINR_i$ given a fixed D. Given N and D, the optimal L^* that maximizes the spectral efficiency is written as

$$L^* \triangleq \underset{L}{\operatorname{argmax}} R_i, \tag{3.12}$$

where N TDs are assumed uniformly distributed and thus share the same spectral efficiency. After that, the optimal bandwidth W^* can be obtained as

$$W^* = \mathbf{f}^{-1}\left(L^*\right), \tag{3.13}$$

where $\mathbf{f}$ is the function that maps the system bandwidth W to the number of resolved independent taps L. The function $\mathbf{f}$ can be derived with curve fitting on the experiment data, e.g. in Fig. 2.8, which would vary with different indoor environments.

Even though various waveform types can be deployed in TRDMA-MA system that results in different values of spectral efficiency, the waveform design method should not affect the L^* and thus the optimal bandwidth W^* for the TRDMA-MA system due to the same number of degree of freedom. Moreover, since there exists a one-to-one mapping between the bandwidth W and L, we try to find the optimal L^* in the following.

In the following, we explore the L^* for TRMDA-MA system with basic TR waveform and ZF waveform.

3.2.1 Basic TR Waveform

Upon acquiring the CIR between the ith TD and the mth antenna, the basic TR waveform can be obtained as the normalized (by the average channel gain to M antennas) complex conjugate of time-reversed CIR,

$$\mathbf{g}_i^{(m)} = \frac{\mathbf{H}_{m,i}^{\left(\frac{L}{D}\right)^\dagger}}{\sqrt{M}}, \tag{3.14}$$

where $\mathbf{H}_{m,i}^{(\frac{L}{D})}$ is the time reversed channel and based on (3.9),

$$\mathbf{H}_{m,i}^{(\frac{L}{D})} = \left[h_i^{(m)}[L], h_i^{(m)}[L-1], \cdots h_i^{(m)}[1] \right]. \qquad (3.15)$$

Based on (3.14), the expected power of signal, ISI and IUI terms in (3.10) can be written as follows,

$$
\begin{aligned}
P_{sig} &= \frac{\rho}{M} \mathbb{E}\left[\left(\sum_{m=1}^{M} \left\| \mathbf{H}_{m,i}^{(\frac{L}{D})} \right\|^2 \right)^2 \right] \\
P_{isi} &= \frac{\rho}{M} \mathbb{E}\left[\sum_{l=1,l\neq L/D}^{(2L-1)/D} \left| \sum_{m=1}^{M} \left(\mathbf{H}_{m,i}^{(l)} \mathbf{H}_{m,i}^{(\frac{L}{D})\dagger} \right) \right|^2 \right] \\
P_{iui} &= \frac{\rho}{M} \mathbb{E}\left[\sum_{j=1,j\neq i}^{N} \sum_{l=1}^{(2L-1)/D} \left| \sum_{m=1}^{M} \mathbf{H}_{m,j}^{(l)} \mathbf{H}_{m,i}^{(\frac{L}{D})\dagger} \right|^2 \right]
\end{aligned}
\qquad (3.16)
$$

Assume that the taps of $\mathbf{h}_i^{(m)}$ and the CIRs of different links are mutually independent. Then, according to the channel model in (3.3), we have

$$
\begin{aligned}
P_{sig} &= \rho \left(\sum_{l=1}^{L} \frac{e^{-\frac{2\alpha}{L}l}}{c^2} + M \right) \\
P_{isi} &= \rho \sum_{l=1,l\neq L/D}^{(2L-1)/D} \beta_l \\
P_{iui} &= \rho(N-1) \sum_{l=1}^{(2L-1)/D} \beta_l,
\end{aligned}
\qquad (3.17)
$$

where

$$
\begin{aligned}
c &= \sum_{l=1}^{L} e^{-\frac{\alpha}{L}l} \\
\beta_l &= \sum_{k=1}^{Dl} \frac{e^{-\frac{\alpha}{L}(L-Dl+2k)}}{c^2}.
\end{aligned}
$$

It is observed that P_{sig} increases with the number of transmit antennas M given the fixed number of users N and backoff factor D. However, P_{sig} decreases with L, since the power of each tap becomes much smaller even though the number of

49

terms is larger. Regarding the other terms, P_{isi} increases with L while P_{iui} decreases with L. Therefore, the main benefit of using a larger bandwidth is to suppress the IUI through resolving a larger L. On the other hand, a larger L leads to a smaller signal power and a larger ISI. Based on these observations, the spectral efficiency increases with L if the decrease in the IUI outperforms the side effect of a larger L on both P_{sig} and P_{isi}. Therefore, there would exist an optimal L^* and thus W^* that can achieve the maximum spectral efficiency.

3.2.2   ZF Waveform

Different from the basic TR waveform that designed based on CIR of each individual TD, ZF waveform is designed according to the CIRs of all TDs, i.e.,

$$\mathbf{g}_i^{(m)} =$$

$$\begin{cases} c_{zf}\mathbf{Q}_m^\dagger \left(\mathbf{Q}_m\mathbf{Q}_m^\dagger\right)^{-1}\mathbf{e}_{l_i}, & \text{if } \mathbf{Q}_m \text{ is full row rank,} \\ \\ c_{zf}\left(\mathbf{Q}_m^\dagger\mathbf{Q}_m\right)^{-1}\mathbf{Q}_m^\dagger\mathbf{e}_{l_i}, & \text{if } \mathbf{Q}_m \text{ is full column rank,} \end{cases} \tag{3.18}$$

where c_{zf} is the normalization factor to make the waveform unitary power, and $\mathbf{Q}_m$ is the combined channel matrix of the N TDs to the mth antenna, i.e.,

$$\mathbf{Q}_m = \left[\mathbf{H}_{m,1}^\dagger\,\mathbf{H}_{m,2}^\dagger\cdots\mathbf{H}_{m,N}^\dagger\right]^\dagger, \tag{3.19}$$

and $\mathbf{e}_{l_i}$ is an elementary vector with

$$l_i = (i-1)\left(2\left\lfloor\frac{L-1}{D}\right\rfloor + 1\right) + \left\lfloor\frac{L-1}{D}\right\rfloor + 1. \tag{3.20}$$

With the definition of $\mathbf{Q}_m$ and $\mathbf{e}_{l_i}$ above, we have

$$\mathbf{Q}_m^\dagger\mathbf{e}_{l_i} = \mathbf{H}_{m,i}^{(\frac{L}{D})\dagger}. \tag{3.21}$$

We first consider the case of $\mathbf{Q}_m$ being full-column rank. Under this scenario, the expected power of the intended signal, ISI and IUI in (3.10) can be derived based on (3.18) and (3.21) as follows,

$$P_{sig} = \rho c_{zf}^2 \mathbb{E}\left[\left|\sum_{m=1}^{M}\left(\mathbf{H}_{m,i}^{(\frac{L}{D})}\left(\mathbf{Q}_m^\dagger \mathbf{Q}_m\right)^{-1}\mathbf{H}_{m,i}^{(\frac{L}{D})\dagger}\right)\right|^2\right]$$

$$P_{isi} = \rho c_{zf}^2 \mathbb{E}\left[\sum_{l=1,l\neq L/D}^{(2L-1)/D}\left|\sum_{m=1}^{M}\left(\mathbf{H}_{m,i}^{(l)}\left(\mathbf{Q}_m^\dagger \mathbf{Q}_m\right)^{-1}\mathbf{H}_{m,i}^{(\frac{L}{D})\dagger}\right)\right|^2\right] \quad (3.22)$$

$$P_{iui} = \rho c_{zf}^2 \mathbb{E}\left[\sum_{\substack{j=1\\j\neq i}}^{N}\sum_{l=1}^{\frac{2L-1}{D}}\left|\sum_{m=1}^{M}\mathbf{H}_{m,j}^{(l)}\left(\mathbf{Q}_m^\dagger \mathbf{Q}_m\right)^{-1}\mathbf{H}_{m,i}^{(\frac{L}{D})\dagger}\right|^2\right].$$

From (3.22), it can been seen that the interference P_{isi} and P_{iui} can not be completely canceled when $\mathbf{Q}_m$ is full column rank. Based on the numerical simulations results in Section 3.3, the interference will decrease as $\mathbf{Q}_m$ tends to be full row rank.

Once $\mathbf{Q}_m$ becomes full row rank, according to (3.18), all the interference can be removed. More specifically,

$$\mathbf{Q}_m \mathbf{g}_i^{(m)} = c_{zf}\mathbf{Q}_m \mathbf{Q}_m^\dagger\left(\mathbf{Q}_m \mathbf{Q}_m^\dagger\right)^{-1}\mathbf{e}_{l_i} = c_{zf}\mathbf{e}_{l_i}. \quad (3.23)$$

In other words,

$$\begin{cases} \mathbf{H}_{m,i}^{(l)}\mathbf{g}_i^{(m)} = 0, & \text{for } \forall i, m \text{ and } l \neq L/D \\[2mm] \mathbf{H}_{m,j}^{(l)}\mathbf{g}_i^{(m)} = 0, & \text{for } \forall l, m \text{ and } i \neq j. \end{cases} \quad (3.24)$$

Therefore, based on (3.24), it is obvious that $P_{isi} = 0$ and $P_{iui} = 0$. The signal power becomes

$$P_{sig} = \rho c_{zf}^2 M^2, \quad (3.25)$$

51

where

$$c_{zf}^2 = \frac{1}{M\mathbb{E}\left[\left(\mathbf{Q}_m\mathbf{Q}_m^\dagger\right)^{-1}\right]_{l_i,l_i}}. \tag{3.26}$$

From the numerical simulation, (3.25) first increases with L and later saturates. Therefore, the spectral efficiency first increases with L and then saturates under the full row rank scenario.

From the above analysis, the optimal L^* is closely related to the rank condition of $\mathbf{Q}_m$. To suppress the ISI and IUI, L^* should be close to the L that makes $\mathbf{Q}_m$ either full row rank or most likely to full row rank. This observation motivates us to propose a sub-optimal $\overline{L}$, solely based on the rank condition of $\mathbf{Q}_m$, as an approximation of L^*. In the following, we analyze the sufficient condition of L to make $\mathbf{Q}_m$ full row rank.

3.2.3 Rank Condition Analysis of $\mathbf{Q}_m$

As defined in (3.19), $\mathbf{Q}_m$ is an $N\left(2\lfloor\frac{L-1}{D}\rfloor + 1\right) \times L$ matrix. Since the taps in each CIR and the CIRs of different TDs are mutually independent, it is reasonable to assume that the rows of $\mathbf{Q}_m$ are independent. Generally, $\mathbf{Q}_m$ will be full row rank when $N\left(2\lfloor\frac{L-1}{D}\rfloor + 1\right) \leq L$. Based on the fact that $\lfloor x \rfloor \leq x$ where x is a positive number, we derive one sufficient condition on L to make $\mathbf{Q}_m$ full row rank.

Theorem 1 (Rank Condition): Given N and D, a sufficient condition on

L to make $\mathbf{Q}_m$ full row rank is

$$
\begin{cases}
L & \leq \frac{2N-DN}{2N-D}, \quad \text{for } D \leq 2N, \\[2ex]
L & \geq \frac{DN-2N}{D-2N}. \quad \text{for } D \geq 2N.
\end{cases}
\tag{3.27}
$$

We observe that in order to make $\mathbf{Q}_m$ full row rank, L has an upper bound when D is small and a lower bound when D is large. Since the interference will be completely canceled when $\mathbf{Q}_m$ is full row rank, we propose a sub-optimal $\overline{L}$ as the approximation to L^* based on the rank condition.

Theorem 2 (Sub-optimal $\overline{L}$): Based on the rank condition of $\mathbf{Q}_m$, the optimal L^* can be approximated by $\overline{L}$ which satisfies

$$
\overline{L} \triangleq \min \left(\underset{L}{\operatorname{argmin}} \left(2N \lfloor \frac{L-1}{D} \rfloor + N - L \right) \right).
\tag{3.28}
$$

According to Theorem 2, the sub-optimal $\overline{L}$ only depends on the system parameters such as the number of users N and the backoff factor D, which makes it much easier to obtain than evaluating the spectral efficiency to derive the optimal L^*. Once the optimal L^* or the sub-optimal $\overline{L}$ is derived, the corresponding bandwidth for the system can be obtained according to (3.13). An example of deriving (3.13) is shown in the following simulation section.

3.3   Simulation Results

In this section, simulations are conducted to evaluate the optimal L^* and thus the optimal bandwidth of the TRDMA-MA system with both basic TR and ZF waveforms.
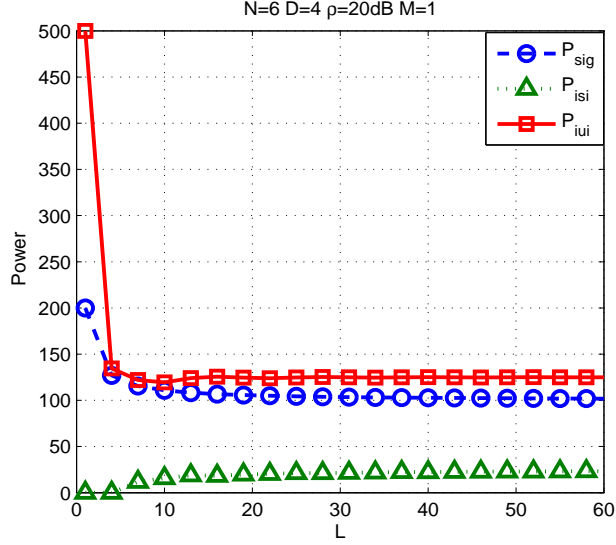
Figure 3.2: P_{sig}, P_{isi} and P_{iui} vs L with Basic TR Waveform.

3.3.1 L^* with Basic TR Waveform

In the following, the system with basic TR waveform is considered. Based on (3.17), we first investigate how these terms in SINR change with L. We assume that $M = 1$, $D = 4$ and $N = 6$. The P_{sig}, P_{isi} and P_{iui} with different L are shown in Fig. 3.2. It is obvious that P_{sig} and P_{iui} decrease with L while P_{isi} increases with L and then all saturate. Therefore, a L^* will exist to achieve maximum SINR and thus the maximum spectral efficiency.

From previous analysis, we find that the optimal L^* is closely related to both D and N. Therefore, in the following, we evaluate the effect of D and N separately on L^*.

54
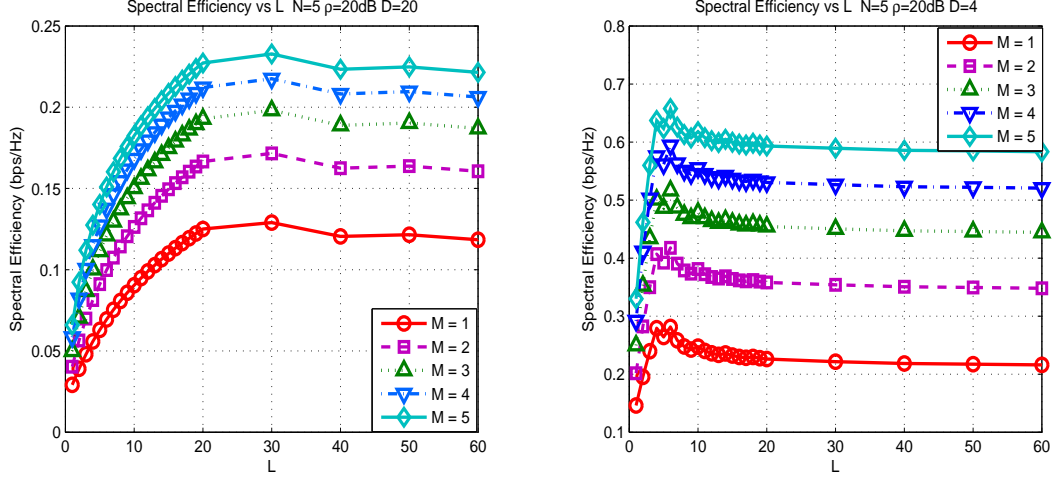
(a) $D = 20$.   (b) $D = 4$.

Figure 3.3: Spectral efficiency of individual with the fixed number of users $N = 5$ and varying M.

3.3.1.1 The effect of D on L^*

First, we investigate the effect of D on L^* given the fixed $N = 5$. We assume the SNR of system is 20dB. The spectral efficiency of one user is shown in Fig. 3.3 with $D = 20$ and $D = 4$. From the figure, it is obvious that M has no effect on L^* even though the spectral efficiency increases with M. The curve of spectral efficiency looks quite distinguishable for large D and small D. More specifically, the spectral efficiency seems to have an upper bound when D is large, i.e., the spectral efficiency saturates after L is sufficiently large. On the other hand, there exists a unique L^* when D is small. The spectral efficiency decreases when $L > L^*$.

Now we study the more general case by selecting a series of D. Since M has no effect on L^*, the number of antenna is fixed as $M = 2$. The spectral efficiency of individual with basic TR waveform is shown in Fig. 3.4. From the figure, we
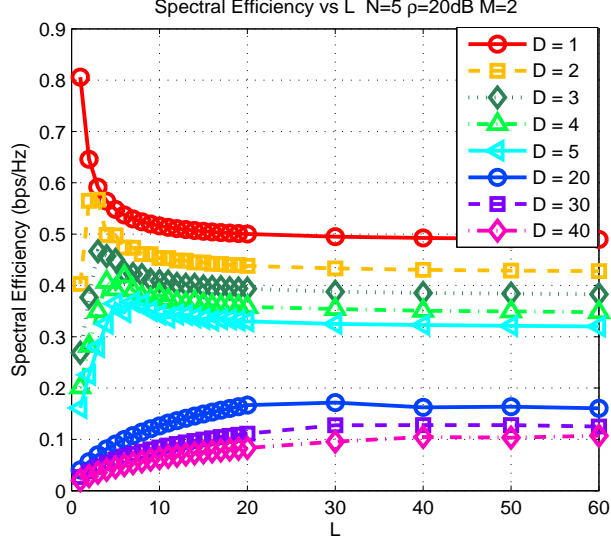
Figure 3.4: Spectral efficiency of individual with $N = 5$, $M = 2$ and varying D

first observe that the spectral efficiency decreases with D, which is due to the fact that the term $1/D$ dominates the improvement of SINR in (3.10). Then, we find that the effect of D on L^* heavily depends on the value of D. On one hand, the L^* increases with D when D is small, e.g., $D = 1 \to 5$. On the other hand, L^* seems independent from D when D is sufficiently large, e.g., $D \geq 20$.

3.3.1.2 The effect of N on L^*

In the following, we explore the effect of N on L^*. As we know, L^* is independent from M and determined by D when D is small. Therefore, we consider the system with $M = 2$ with varying N for both $D = 20$ and $D = 4$ in the following simulation. From Fig. 3.5, it is obvious that the spectral efficiency decreases with N since the IUI increases with N. As shown in Fig. 3.5(a), the larger the N, the larger the L^* to achieve the maximum spectral efficiency when D is large. It is also

56
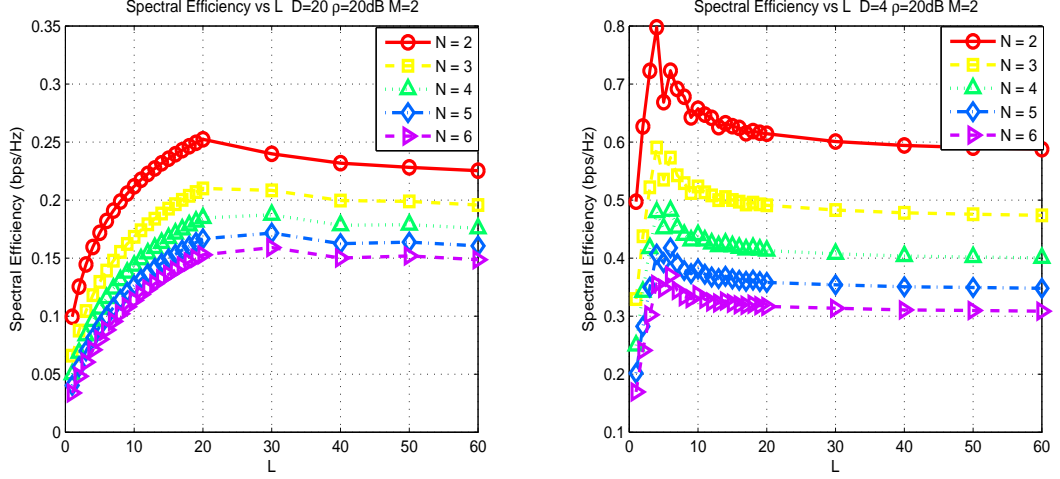
(a) $D = 20$.   (b) $D = 4$.

Figure 3.5: Spectral efficiency of individual with $M = 2$ and varying N.

validated that the L^* is independent of N when D is small as shown in Fig. 3.5(b).

Remark: By summarizing the previous simulation results of the spectral efficiency with basic TR waveform, we observe that L^* is determined by N and D instead of M. Moreover, when D is small, L^* is independent of N but increases with D. On the other hand, when D is large, L^* increases with N but independent of D. Even though different waveform design methods can achieve different spectral efficiencies, the L^* should be independent of the specified waveform design methods. Therefore, the conclusion about L^* in this subsection can also be applied for the ZF waveform scenario, which is validated in the following subsection.

3.3.2 L^* with ZF Waveform

As discussed in the previous subsection, we find some general conclusion about the effect of D and N on L^* under the basic TR scenario. In the following, we will
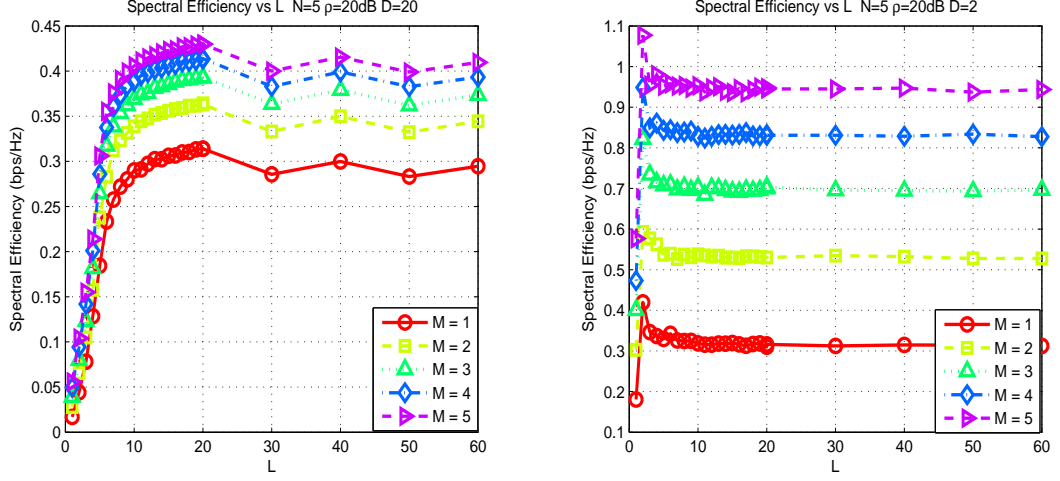
(a) $D = 20$.   (b) $D = 2$.

Figure 3.6: Spectral efficiency of individual with the fixed number of users $N = 5$ and varying M.

demonstrate that the same conclusion is applicable to ZF waveform scenario as well.

3.3.2.1 The effect of D on L^*

We first investigate the effect of D on L^* given the fixed $N = 5$. Same as the previous, we evaluate the spectral efficiency for both large D and small D with ZF waveform. We assume the SNR of the system is 20dB. The spectral efficiency with ZF waveform is shown in Fig. 3.6, where $D = 20$ and $D = 2$. First of all, the spectral efficiency increases with M but L^* is independent from M. When D is large as shown in Fig. 3.6(a), L has a lower bound to achieve the maximum spectral efficiency. While D is small, there exists a unique L^* as shown in Fig. 3.6(b).

Then we investigate the spectral efficiency under ZF waveform with varying D. We fix $M = 2$ and $N = 5$ in the simulation. According to Fig. 3.7, the L^* to
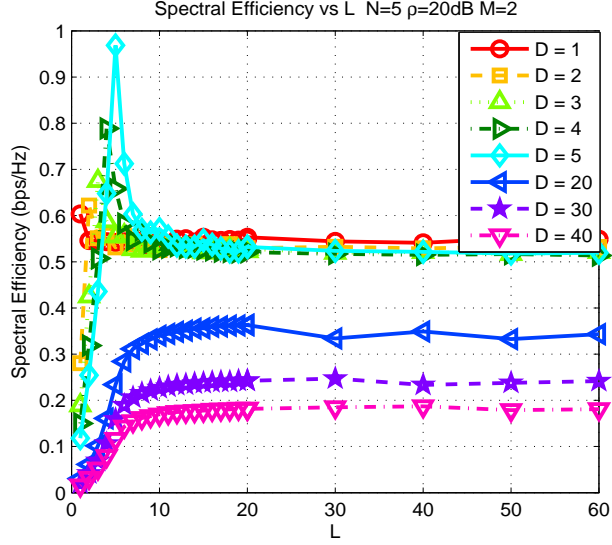
Figure 3.7: Spectral efficiency of individual with $N = 5$, $M = 2$ and varying D

achieve the maximum spectral efficiency increases with D given D is small. While D is sufficiently large, L^* tends to be independent of D.

3.3.2.2 The effect of N on L^*

We explore the effect of N on L^* in the following. In the simulation, we fixed $M = 2$ and SNR to be 20dB. The spectral efficiency is simulated with varying N for both $D = 20$ and $D = 2$ as shown in Fig. 3.8. From Fig. 3.8(a), it is shown that L^* increases with N when D is efficiently large. However, L^* becomes independent of N when D is small as shown in Fig. 3.8(b).

Remark: From the simulation results for ZF waveform, we find the effect of D and N on L^* is exactly same with the basic TR waveform scenario. In other words, the L^* has been validated to be independent of the waveform types. Our
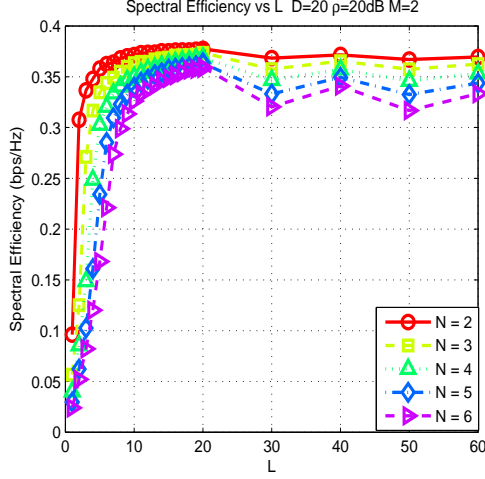
(a) $D = 20$.
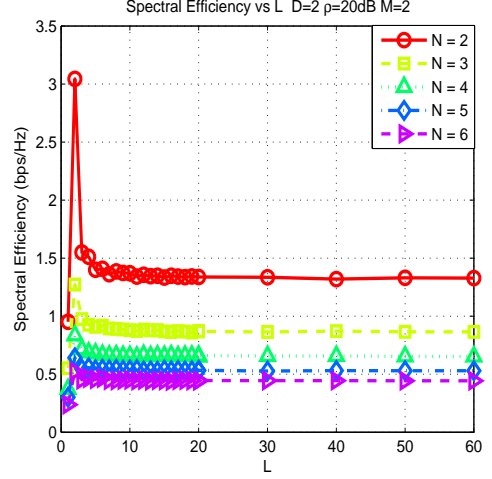
(b) $D = 2$.

Figure 3.8: Spectral efficiency of individual with $M = 2$ and varying N.

findings can be summarized in the following equation,

$$
L^* = \begin{cases} \mathrm{f}\,(D), & \text{when } D \text{ is small} \\ \\ \mathrm{g}\,(N). & \text{when } D \text{ is large.} \end{cases} \tag{3.29}
$$

where both f and g are the increasing functions.

3.3.3   Sub-optimal $\overline{L}$ Based on Rank Condition

Even though we have found some useful conclusions about L^* in (3.29), the spectral efficiency needs to be evaluated to get the exact value of L^*, which is costly in terms of computation. Based on the discussion in Section 3.2.3, we propose the rank evaluation as an alternative of computing the spectral efficiency, which provides a sub-optimal approximation of L^*. Although the rank evaluation is more intuitive for ZF waveform, it is also applicable for other waveform types according to the previous discussion.
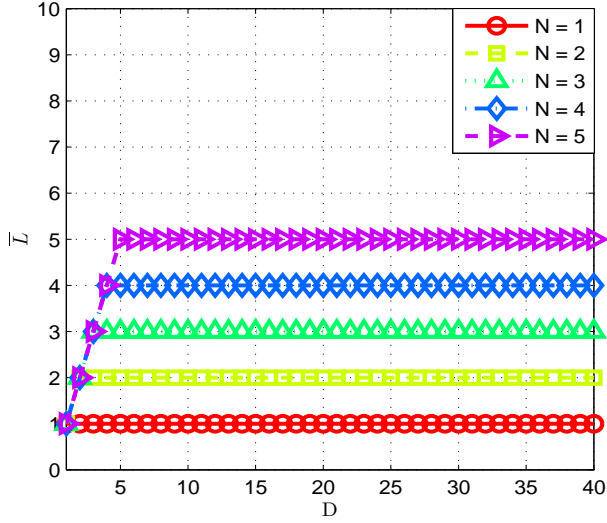
Figure 3.9: Sub-optimal $\overline{L}$ with varying D and N

Based on (3.28) in Theorem 2, the sub-optimal $\overline{L}$ only depends on D and N, which is plotted in Fig. 3.9. From the figure, it is obvious that the sub-optimal $\overline{L}$ is consistent with L^* in terms of (3.29). By comparing Fig. 3.9 with Fig. 3.4 and Fig. 3.7, $\overline{L}$ is quite accurate as an estimation of L^* when D is small. When D is large, $\overline{L}$ becomes an lower bound for L^* as shown in Fig. 3.5(a) and Fig. 3.8(a). For the system with ZF waveform, the spectral efficiency continues to increase with L for a while after $\overline{L}$, since the c_{zf} in (3.25) continues to increase with L before it saturates.

The sub-optimal $\overline{L}$ compared with L^* has more practical meaning. First of all, the derivation of $\overline{L}$ solely depends on D and N without evaluating the spectral efficiency. Second, the estimation of L^* based on $\overline{L}$ is very accurate when D is small, which is the typical setting in communication. Once the $\overline{L}$ is derived, the sub-optimal bandwidth for the system can be calculated according to (3.13).

3.4   Conclusion

In this chapter, we investigate the optimal bandwidth for the TR system to achieve the maximum spectral efficiency. Through evaluating the spectral efficiency of TR system with both basic TR waveform and ZF waveform, we find that the optimal bandwidth for TR system, instead of being affected by the waveform types, is determined by the system parameters such as the number of users N and backoff factor D. We validate with simulations that the optimal bandwidth increases with D when D is small while increases with N when D is large. Finally, based on the rank condition of channel matrix, a sub-optimal bandwidth is proposed for TR system. Based on the simulation results, it is shown that the sub-optimal bandwidth serves as a low bound for optimal bandwidth and the bound is quite tight when D is small.

Chapter 4

Limited Waveform Precision: Tradeoff Between Complexity and

Performance

As shown in the previous chapters, the success of TR communication for 5G indoor scenario relies on the waveform designed based on the many multipaths naturally existing in the environment. Moreover, considering the asymmetric system architecture [28], the overall hardware and computational complexity of TR communication systems mostly lie in the waveform-embedding process.

Due to the finite resource in hardware, the waveforms of the TR system are quantized and thus of limited precision instead of the prefect precision in the ideal case. Such limited precision in the waveform will degrade the TR spatio-temporal resonating effect [12] and thus the performance of the TR systems. Moreover, embedding the high precision waveforms into the transmit signal is practically difficult especially with a rate of gigabit per second [1], which translates into not only the hardware complexity but also computation burden. Although many works have been proposed in the literature to theoretical analyze the TR system with the assumption of full-precision waveform [9, 13, 17, 19, 28, 34, 48, 65, 69, 70], few work has been done on analyzing the TR systems with limited waveform precision except those on one-bit TR system [1, 11, 20, 36, 47].

In [20], it is shown that the received signal-to-noise-ratio (SNR) is lowered by 1.2 dB with only one-bit waveform. Followed by that work, several works have studied the performance of one-bit TR system. For example, the Nguyen derived the analytical solutions for the temporal and spatial focusing metrics of one-bit TR system [47], while the Chang et al. in [11] applied one-bit TR in Ultra-wideband (UWB) communication systems and examined the system performance. Moreover, the one-bit TR UWB communication system was further extended to a single-input-multiple-out (SIMO) architecture [36].

More recently, a study on the system performance with generalized number of quantization bits is provided in [29], where a TR system with only one user is considered. In [29], it is shown that one-bit quantization is not enough for the TR system in terms of communication purpose. In the academic integrity of the TR system, we extend the previous work to multiuser scenario and explore the system performance degradation with generalized number of quantization bits and number of users in this chapter. Specifically, we try to address the question that how many quantization bits are required for a TRDMA system with multiple users to achieve similar performance compared to that in the prefect precision scenario. To do so, we first derive theoretically the generalized effective signal-to-interference-plus-noise ratio (SINR) in the multiuser case with varying quantization stepsize. Then, a metric α is proposed to characterize the relative performance loss due to the quantization in terms of effective SINR. Through evaluating the impact of other system parameters (e.g., the number of users and the backoff factor) on α, we discuss about the quantization requirement with varying system parameters to maintain

64

the same level of system performance. Finally, it is found that 4-bit quantization is enough for the TRDMA system by numerically evaluating the bit-error-rate (BER) performance with different number of quantization bits.

The rest of the chapter is organized as follows. The system model is described in Section 4.1. In Section 4.2, we propose the effective SINR for the TRDMA system with limited waveform precision based on the system model. The theoretical effective SINR with varying quantization stepsize is derived in the closed-form in Section 4.3. Moreover, a metric α is proposed to depict the performance degradation due to quantization. In Section 4.4, we discuss the relationship between the quantization stepsize and the number of quantization bits. In Section 4.5, the theoretical analysis is validated using numerical simulation. Finally, Section 4.6 concludes this chapter.

4.1 System Model

In this chapter, we consider a time-reversal downlink system where one transmitter simultaneously communicates with N distinct receivers through the TRDMA technique [28]. We assume that both the transmitter and receivers are equipped with one single antenna. However, the results can be easily extended to multiple-antenna scenario.

4.1.1 Channel Model

There exits a large amount of multipaths in the indoor environment, which can be harvested with a large bandwidth. More specifically, a larger number of

multipaths can be resolved with the increase of bandwidth because of the better time resolution. Based on the real indoor ultra-wide-band (UWB) channel measurement (both LOS and NLOS) in [55] and [31], around 100 independent multipaths can be revealed with a sufficiently large bandwidth.

In this chapter, we consider a multipath Rayleigh fading channel model. Equipped with a large bandwidth W, we assume that TRDMA system can resolve L independent multipaths in the environment. The channel impulse response (CIR) between the AP and the ith TD is modeled as

$$\mathbf{h}_i[k] = \sum_{l=0}^{L-1} h_{i,l}\delta[k-l], \tag{4.1}$$

where $h_{i,l}$ is the complex channel gain of the lth tap in the CIR, and $\delta[\cdot]$ is the Dirac delta function. For the CIR to each TD, we assume that $\mathbf{h}_i[k]$'s are independent circular symmetric complex Gaussian (CSCG) random variables with zero mean and variance σ_k^2.

Based on the two-phase property of the TR technique, the channels are assumed to be reciprocal, ergodic and blockwise-constant with their tap values remaining fixed during at least one duty circle. Moreover, we assume that the CIRs to different TDs are mutually uncorrelated since real indoor experiment results in [67] show that in a typical indoor environment the correlation between CIRs associated with distinct locations decreases to a neglectable level even when these locations are just several wavelengths apart.

4.1.2 Channel Probing Phase

Prior to the data transmission, N TDs first take turn to transmit an impulse signal to the AP, which in practice is a modified raised-cosine signal depending on the system bandwidth W. Meanwhile, the AP records the channel response $\mathbf{h}_i$ for the ith TD. Without loss of generality, we assume in this chapter that the channel responses recorded by AP reflect the true channel response, ignoring the small corruption caused by thermal noise. Such an assumption is reasonable since the thermal noise can be effective reduced by utilizing the pseudo-random sequence for channel estimation [26].

Upon acquiring the $\mathbf{h}_i$'s for the ith TD, basic TR waveform $\mathbf{g}_i$'s [65] can be deployed at the AP side, i.e.,

$$\mathbf{g}_i[k] = \frac{\mathbf{h}_i^*[L-1-k]}{\sqrt{\sum_{l=0}^{L-1} \sigma_l^2}}. \tag{4.2}$$

From (4.2), we can see that $\mathbf{g}_i$'s for different TDs are i.i.d. and and obey CSCG distribution, i.e., $\mathbf{g}_i[k] \sim CN(0, \sigma_{L-1-k}^2/\sigma_s^2)$, where $\sigma_s^2 = \sum_{l=0}^{L-1} \sigma_l^2$. These waveforms serve as the precoding in the downlink transmission phase as shown in Fig. 4.1.

4.1.3 Downlink Transmission Phase

The block diagram of a TRDMA downlink system is shown in Fig. 4.1. According to Fig. 4.1, there is a sequence of information symbols $\mathbf{X}_i$ at the AP to be transmitted to the ith TD. To suppress the inter-symbol-interference (ISI) as well as match the symbol rate with chip rate, a backoff factor D is introduced by inserting
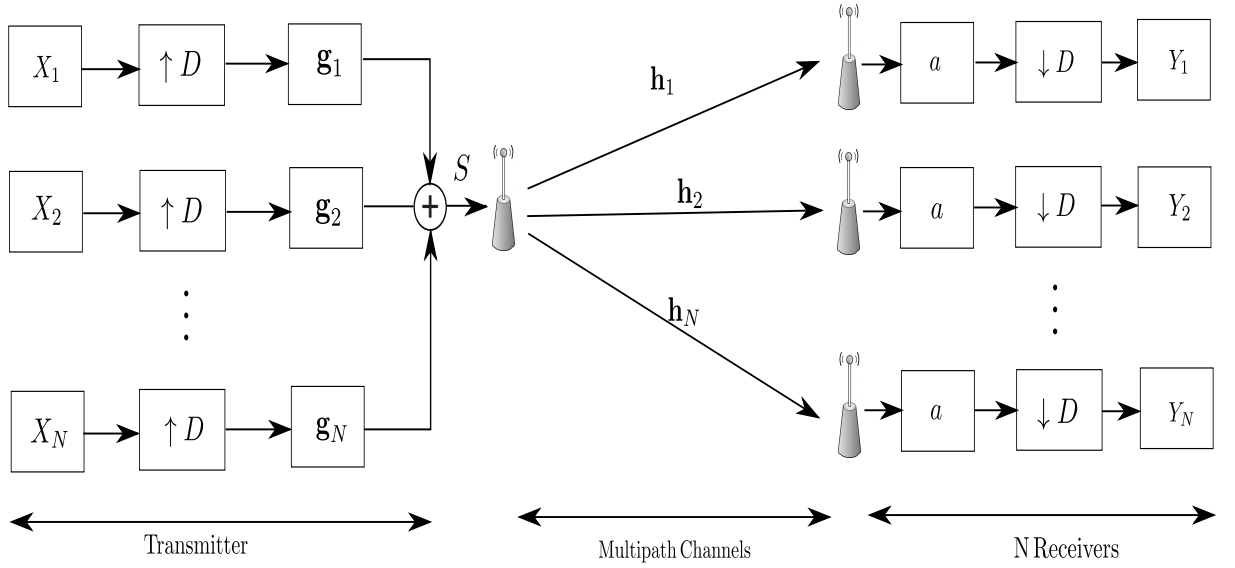
Figure 4.1: The diagram of TRDMA downlink system.

$(D-1)$ zeros between two symbols [22, 28, 65] , i.e.,

$$X_i^{[D]}[k] = \begin{cases} X_i[k/D], & \text{if } (k \bmod D) = 0, \\ \\ 0, & \text{if } (k \bmod D) \neq 0, \end{cases} \tag{4.3}$$

where $(\cdot)^{[D]}$ denotes the D-times upsampling. Then the upsampled information symbols $\{\mathbf{X}_i^{[D]}[k]\}$ are convolved with the specific waveform $\mathbf{g}_i$. By convolving the information symbols with $\mathbf{g}_i$'s, it provides a mechanism to embed the location-specific waveform into the symbols for the intended TD. After that, all the waveform-embedded symbols are added together, and then the combined signal $\{S[k]\}$ is broadcasted into wireless channels with

$$S[k] = \sum_{i=1}^{N} \left(\mathbf{X}_i^{[D]} * \mathbf{g}_i \right)[k]. \tag{4.4}$$

Later, the signal received at the ith TD is represented as

$$Y_i^{[D]}[k] = \left(\sum_{j=1}^{N} \mathbf{X}_j^{[D]} * \mathbf{g}_j * \mathbf{h}_i \right) + \widetilde{n}_i[k], \tag{4.5}$$

68

which is the convolution of the broadcast signal $\{S[k]\}$ and the CIR $\mathbf{h}_i$, plus an additive white Gaussian noise with zero mean and unity power. Thanks to the TR spatio-temporal resonating effect, the ith TD can detect the information symbols $\{X_i[k]\}$ with a simple one-tap detection. After amplifying the received signal by an amplifier with the gain a_i, the ith TD downsamples the signal with the same backoff factor D, ending up with $Y_i[k]$ shown as follows,

$$Y_i[k] = (\mathbf{h}_i * \mathbf{g}_i)[L-1]X_i[k - \frac{L-1}{D}] + \sum_{l=0, l \neq \frac{L-1}{D}}^{\frac{2L-2}{D}} (\mathbf{h}_i * \mathbf{g}_i)[Dl]X_i[k-l]$$
$$+ \sum_{j=1, j \neq i}^{N} \sum_{l=0}^{\frac{2L-2}{D}} (\mathbf{h}_i * \mathbf{g}_j)[Dl]X_j[k-l] + n_i[k], \tag{4.6}$$

where the terms in (4.6) represents the intended signal, ISI, inter-user-interference (IUI) and additive noise.

Nevertheless, the waveforms $\mathbf{g}_i$'s need to be quantized before deployed in Fig. 4.1, which results in performance degradation due to the limited precision of waveforms. More specifically, denote $\widetilde{\mathbf{g}}_i$ as the quantized waveform and thus $\mathbf{e}_i = \widetilde{\mathbf{g}}_i - \mathbf{g}_i$ represents the quantization noise of the waveforms. In next section, we will theoretically analyze the TRDMA system with quantized waveforms $\widetilde{\mathbf{g}}_i$'s and evaluate the performance degradation due to the quantization.

4.2 TRDMA System with Limited Waveform Precision

In a practical communication system with hardware implementation, quantization is an inevitable process to go through before the waveform implemented in the real hardware. In this section, we conduct the theoretical analysis on the TRDMA

69

system with limited waveform precision. More specifically, we first investigate how the quantization noise degrades the received symbols $Y_i[k]$ in (4.6). Then, the associated effective signal-to-interference-plus-noise ratio (SINR) is defined. After that, we initiate the statistical analysis of the defined effective SINR without considering the quantization error based on the statistical channel model in (4.1).

4.2.1　Received Symbols

According to the previous discussion, the quantized waveform $\widetilde{\mathbf{g}}_i$'s are deployed in a practical TRDMA system instead of the perfect waveforms $\mathbf{g}_i$'s. Therefore, the received symbols in the limited-precision TRDMA system can be expressed as

$$
\begin{aligned}
Y_i[k] = (\mathbf{h}_i * \widetilde{\mathbf{g}}_i)\,[L-1]X_i[k - \frac{L-1}{D}] + \sum_{l=0, l \neq \frac{L-1}{D}}^{\frac{2L-2}{D}} (\mathbf{h}_i * \widetilde{\mathbf{g}}_i)\,[Dl]X_i[k-l] \\
+ \sum_{j=1, j \neq i}^{N} \sum_{l=0}^{\frac{2L-2}{D}} (\mathbf{h}_i * \widetilde{\mathbf{g}}_j)\,[Dl]X_j[k-l] + n_i[k].
\end{aligned}
\tag{4.7}
$$

With the relationship that $\widetilde{\mathbf{g}}_i = \mathbf{e}_i + \mathbf{g}_i$, where $\mathbf{e}_i$ stands for the quantization noise, (4.7) can be rewritten as

$$
\begin{aligned}
Y_i[k] = (\mathbf{h}_i * \mathbf{g}_i)\,[L-1]X_i[k - \frac{L-1}{D}] + \sum_{l=0, l \neq \frac{L-1}{D}}^{\frac{2L-2}{D}} (\mathbf{h}_i * \mathbf{g}_i)\,[Dl]X_i[k-l] \\
+ \sum_{j=1, j \neq i}^{N} \sum_{l=0}^{\frac{2L-2}{D}} (\mathbf{h}_i * \mathbf{g}_j)\,[Dl]X_j[k-l] + Q_i[k] + n_i[k],
\end{aligned}
\tag{4.8}
$$

70

where $Q_i[k]$ represents the additional term of quantization error, i.e.,

$$Q_i[k] = (\mathbf{h}_i * \mathbf{e}_i)[L-1]X_i[k - \frac{L-1}{D}]$$
$$+ \sum_{l=0,l\neq\frac{L-1}{D}}^{\frac{2L-2}{D}} (\mathbf{h}_i * \mathbf{e}_i)[Dl]X_i[k-l] \qquad (4.9)$$
$$+ \sum_{j=1,j\neq i}^{N} \sum_{l=0}^{\frac{2L-2}{D}} (\mathbf{h}_i * \mathbf{e}_j)[Dl]X_j[k-l].$$

Due to the additional quantization error term $Q_i[k]$, it is obvious that the decoding of

$X_i[k-\frac{L-1}{D}]$ based on $Y_i[k]$ becomes harder for the TRDMA system with quantization.

4.2.2 Effective SINR

To characterize the effect of quantization on the system performance, an effective SINR is defined for the TRDMA system with limited waveform precision. We define the effective SINR at the ith TD $SINR_i$ as the ratio of the averaged signal power to the averaged inference, quantization error, and noise power, i.e.,

$$SINR_i = \frac{\mathbb{E}[P_{sig}]}{\mathbb{E}[P_{isi}] + \mathbb{E}[P_{iui}] + \mathbb{E}[P_{quan}] + 1}, \qquad (4.10)$$

where the additive white noise is assumed to be of unit power, and the other terms are defined as

$$\mathbb{E}[P_{sig}] = \mathbb{E}\left[\left|(\mathbf{h}_i * \mathbf{g}_i)[L-1]X_i[k - \frac{L-1}{D}]\right|^2\right],$$
$$\mathbb{E}[P_{isi}] = \mathbb{E}\left[\sum_{l=0,l\neq\frac{L-1}{D}}^{\frac{2L-2}{D}}\left|(\mathbf{h}_i * \mathbf{g}_i)[Dl]X_i[k-l]\right|^2\right], \qquad (4.11)$$
$$\mathbb{E}[P_{iui}] = \mathbb{E}\left[\sum_{j=1,j\neq i}^{N}\sum_{l=0}^{\frac{2L-2}{D}}\left|(\mathbf{h}_i * \mathbf{g}_j)[Dl]X_j[k-l]\right|^2\right],$$

and

$$
\begin{aligned}
\mathbb{E}\left[P_{quan}\right] = {} & \mathbb{E}\left[\left|\left(\mathbf{h}_i * \mathbf{e}_i\right)\left[L-1\right]X_i[k-\frac{L-1}{D}]\right|^2\right] \\
& + \mathbb{E}\left[\sum_{l=0, l \neq \frac{L-1}{D}}^{\frac{2L-2}{D}}\left|\left(\mathbf{h}_i * \mathbf{e}_i\right)[Dl]X_i[k-l]\right|^2\right] \\
& + \mathbb{E}\left[\sum_{j=1, j \neq i}^{N}\sum_{l=0}^{\frac{2L-2}{D}}\left|\left(\mathbf{h}_i * \mathbf{e}_j\right)[Dl]X_j[k-l]\right|^2\right].
\end{aligned} \tag{4.12}
$$

Due to the quantization error $\mathbb{E}[P_{quan}]$, the effective SINR in the practical TRDMA system degrades compared with the that in the ideal case (full precision).

Note that the effective SINR in (4.10) can be treated as an approximation of the quantity $\mathbb{E}\left[\frac{P_{sig}}{P_{isi}+P_{iui}+P_{quan}+1}\right]$. Such an approximation is especially useful when the calculation of the averaged SINR using multiple integration is too complex, as is the case in literatures such as [22, 28, 44].

4.2.3   Statistical Analysis of P_{sig}, P_{isi} and P_{iui}

In the following, we initiate the statistical analysis of the effective SINR by obtaining the closed-form for P_{sig}, P_{isi} and P_{iui} based on the channel model.

Based on the channel model presented in Section II, the fourth moments of $\mathbf{h}_i[k]$ are given by

$$
\mathbb{E}\left[\left|\mathbf{h}_i[k]\right|^4\right] = 2\sigma_k^4, \tag{4.13}
$$

where σ_k^2 is the second moment of $\mathbf{h}_i[k]$. Depends on (4.1) and (4.13), after some basic mathematical derivations, we obtain the following expected values with inde-

pendent assumption of CIRs for different TDs, i.e.,

$$\mathbb{E}[P_{sig}] = \frac{\theta}{\sigma_s^2}\left(\sum_{l=0}^{L-1}\sigma_l^4 + \sigma_s^2\right),$$

$$\mathbb{E}[P_{isi}] = \frac{\theta}{\sigma_s^2}\left(\sum_{l=0, l\neq\frac{L-1}{D}}^{(2L-2)/D}\sum_{m=Dl-L+1}^{Dl}\sigma_m^2\sigma_{L-1-Dl+m}^2\right),\tag{4.14}$$

$$\mathbb{E}[P_{iui}] = \frac{\theta(N-1)}{\sigma_s^2}\left(\sum_{l=0}^{(2L-2)/D}\sum_{m=Dl-L+1}^{Dl}\sigma_m^2\sigma_{L-1-Dl+m}^2\right),$$

where θ represents the power of symbol $X_i[k]$ and $\sigma_s^2 = \sum_{l=0}^{L-1}\sigma_l^2$.

Assume that the CIR obeys exponential decay as in [28], i.e.,

$$\sigma_k^2 = e^{-\frac{kT_s}{\sigma_T}}, \qquad 0 \leq k \leq L-1 \tag{4.15}$$

where T_s is the sampling period such that the system bandwidth $W = 1/T_s$, and σ_T is the root mean square (rms) delay spread of channel. Then, (4.14) can be further simplified as (4.16).

$$\mathbb{E}[P_{sig}] = \theta\frac{1+e^{-\frac{LT_s}{\sigma_T}}}{1+e^{-\frac{T_s}{\sigma_T}}} + \theta\frac{1-e^{-\frac{LT_s}{\sigma_T}}}{1-e^{-\frac{T_s}{\sigma_T}}},$$

$$\mathbb{E}[P_{isi}] = 2\theta\frac{e^{-\frac{T_s}{\sigma_T}}\left(1-e^{-\frac{(L-2+D)T_s}{\sigma_T}}\right)}{\left(1-e^{-\frac{DT_s}{\sigma_T}}\right)\left(1+e^{-\frac{T_s}{\sigma_T}}\right)},\tag{4.16}$$

$$\mathbb{E}[P_{iui}] = \theta(N-1)\frac{\left(1+e^{-\frac{DT_s}{\sigma_T}}\right)\left(1+e^{-\frac{2LT_s}{\sigma_T}}\right) - 2e^{-\frac{(L+1)T_s}{\sigma_T}}\left(1+e^{-\frac{(D-2)T_s}{\sigma_T}}\right)}{\left(1-e^{-\frac{DT_s}{\sigma_T}}\right)\left(1+e^{-\frac{T_s}{\sigma_T}}\right)\left(1-e^{-\frac{LT_s}{\sigma_T}}\right)}.$$

Note that in order to numerically characterize the effect of quantization on the system performance, the theoretical analysis of $\mathbb{E}[P_{quan}]$ is necessary but on which no previous work exists. The analysis of the expected power of the term $Q_i[k]$

requires the knowledge of quantization theory, which will be fully discussed in the next section.

4.3   Statistical Analysis of Quantization Error in TRDMA System

To completely evaluate of the effective SINR in the limited-precision TRDMA system, we need to theoretically derive $\mathbb{E}[P_{quan}]$ based on the quantization theory. In this section, we first introduce the statistical relationship between the Gaussian quantizer input and its quantization noise in Lemma 1. Then, after some basic mathematical derivation, we obtain the closed-form of $\mathbb{E}[P_{quan}]$ as a function of the quantization stepsize q based on the general channel model in (4.1). Moreover, a simplified $\mathbb{E}[P_{quan}]$ can be further derived with the exponential decay assumption in the multipath channel. After that, a metric α is proposed to depicts the system performance degradation, in terms of the effective SINR, due to the quantization.

4.3.1   Statistical Relationship between Gaussian Input and Quantization Noise

Let υ be a Gaussian random variable with zero mean and variance σ^2. After going through the uniform quantizer with the quantization stepsize q, ϵ represents the associated quantization noise, i.e., the difference between the quantized output and the input υ. The statistical properties of υ and ϵ are summarized in Lemma 1 as follows.

Lemma 1: Given the Gaussian random input υ and the quantization stepsize

q, we have [66]

$$\mathbb{E}[\epsilon] = 0$$

$$\mathbb{E}[\epsilon^2] = \frac{q^2}{12} + \frac{q^2}{\pi^2} \sum_{l=1}^{\infty} \Phi_\upsilon(\frac{2\pi l}{q})\frac{(-1)^l}{l^2}$$

$$\mathbb{E}[\upsilon\epsilon] = \frac{q}{\pi} \sum_{l=1}^{\infty} \dot{\Phi}_\upsilon(\frac{2\pi l}{q})\frac{(-1)^{l+1}}{l}$$

$$\mathbb{E}[\upsilon^2\epsilon^2] = \frac{\sigma^2 q^2}{12} + \frac{q^2}{\pi^2} \sum_{l=1}^{\infty} \mathbf{Re}\{\ddot{\Phi}_\upsilon(\frac{2\pi l}{q})\}\frac{(-1)^{l+1}}{l^2}$$

(4.17)

where Φ_υ is the characteristic function of Gaussian random variable υ.

Moreover, from the numerical results shown in Table 4.1, we find that, when q is small, the quantities $\mathbb{E}[\epsilon^2]$, $\mathbb{E}[\upsilon\epsilon]$ and $\mathbb{E}[\upsilon^2\epsilon^2]$ can be approximated as $q^2/12$, 0, and $\sigma^2 q^2/12$, respectively.

	$\mathbb{E}[\epsilon]$	$\mathbb{E}[\epsilon^2]$	$\mathbb{E}[\upsilon\epsilon]$	$\mathbb{E}[\upsilon^2\epsilon^2]$
$q = 2\sigma$	0	$\left(\frac{1}{12} - 6.7 \times 10^{-4}\right) q^2$	-2.47×10^{-2}	$\frac{\sigma^2 q^2}{12}\left(1 + 7.91 \times 10^{-2}\right)$
$q = 1.5\sigma$	0	$\left(\frac{1}{12} - 2.8 \times 10^{-5}\right) q^2$	-9.1×10^{-4}	$\frac{\sigma^2 q^2}{12}\left(1 + 5.3 \times 10^{-3}\right)$
$q = \sigma$	0	$\left(\frac{1}{12} - 4.5 \times 10^{-6}\right) q^2$	-1.2×10^{-4}	$\frac{\sigma^2 q^2}{12}\left(1 + 1.00 \times 10^{-5}\right)$

Table 4.1: Statistical Relationship between υ and ϵ

4.3.2 The Closed-form of $\mathbb{E}[P_{quan}]$

Based on the channel model in (4.1) and Lemma 1, the statistical features of the quantization terms are summarized in Lemma 2.

Lemma 2: With the quantization stepsize q, the average of the quantization terms is given as

$$\mathbb{E}\left[|(\mathbf{h}_i * \mathbf{e}_i)[L-1]|^2\right] \approx \frac{q^2 \sigma_s^2}{6},$$

$$\mathbb{E}\left[\sum_{l=0, l \neq \frac{L-1}{D}}^{\frac{2L-2}{D}} |(\mathbf{h}_i * \mathbf{e}_i)[Dl]|^2\right] \approx \frac{q^2}{6} \sum_{l=0, l \neq \frac{L-1}{D}}^{\frac{2L-2}{D}} \sum_{m=Dl-L+1}^{Dl} \sigma_m^2, \qquad (4.18)$$

$$\mathbb{E}\left[\sum_{j=1, j \neq i}^{N} \sum_{l=0}^{\frac{2L-2}{D}} |(\mathbf{h}_i * \mathbf{e}_j)[Dl]|^2\right] \approx \frac{(N-1)q^2}{6} \sum_{l=0}^{\frac{2L-2}{D}} \sum_{m=Dl-L+1}^{Dl} \sigma_m^2,$$

where σ_k^2 is the variance of $\mathbf{h}_i[k]$ and $\sigma_s^2 = \sum_{k=0}^{L-1} \sigma_k^2$.

Proof: Based on (4.2) and the fact that $\mathbf{e}_i = \widetilde{\mathbf{g}}_i - \mathbf{g}_i$, it is obvious that $\mathbf{e}_i$ is independent from $\mathbf{g}_j$, where $j \neq i$. Moreover, $\mathbb{E}[\mathbf{e}_i(k)\mathbf{e}_i(l)] = 0$ for $l \neq k$.

Since the real part and imaginary part of a CSCG random variable can be considered as two independent Gaussian random variables, we can derive the following equalities when the quantization stepsize q is small based on Lemma 1 and (4.2), i.e.,

$$\mathbb{E}[\mathbf{e}_i(k)] = 0,$$

$$\mathbb{E}\left[|\mathbf{e}_i(k)|^2\right] = \mathbb{E}\left[|\mathbf{e}_i^R(k)|^2\right] + \mathbb{E}\left[|\mathbf{e}_i^I(k)|^2\right] \approx \frac{q^2}{6}, \qquad (4.19)$$

$$\mathbb{E}\left[\mathbf{e}_i^R(k)\mathbf{g}_i^R(k)\right] = \mathbb{E}\left[\mathbf{e}_i^I(k)\mathbf{g}_i^I(k)\right] = 0,$$

$$\mathbb{E}\left[|\mathbf{e}_i^R(k)\mathbf{g}_i^R(k)|^2\right] = \mathbb{E}\left[|\mathbf{e}_i^I(k)\mathbf{g}_i^I(k)|^2\right] \approx \frac{q^2 \sigma_{L-1-k}^2}{24\sigma_s^2},$$

where $\mathbf{e}_i^R(k) = \text{real}(\mathbf{e}_i(k))$ and $\mathbf{e}_i^I(k) = \text{imag}(\mathbf{e}_i(k))$. Moreover, $\mathbf{g}_i^R(k)$ and $\mathbf{g}_i^I(k)$ are defined similarly.

Hence, based on (4.2), we have

$$(\mathbf{h}_i * \mathbf{e}_i)[L-1] = \sigma_s \sum_{l=0}^{L-1} \mathbf{g}_i^*[L-1-l]\mathbf{e}_i[L-1-l],$$

$$(\mathbf{h}_i * \mathbf{e}_i)[Dl] = \sigma_s \sum_{m=0}^{L-1} \mathbf{g}_i^*[L-1-m]\mathbf{e}_i[Dl-m], \qquad (4.20)$$

$$(\mathbf{h}_i * \mathbf{e}_j)[Dl] = \sigma_s \sum_{m=0}^{L-1} \mathbf{g}_i^*[L-1-m]\mathbf{e}_j[Dl-m].$$

Substituting (4.19) into (4.20), Lemma 2 can be derived considering the independence properties. □

Therefore, depends on Lemma 2, the expected power of quantization error is obtained in the following theorem.

Theorem 1: With the quantization stepsize q, the expected power of quantization error in TRDMA system can be approximated as

$$
\mathbb{E}[P_{quan}] \approx \frac{\theta q^2 \sigma_s^2}{6} + \frac{\theta q^2}{6} \sum_{l=0,l\neq\frac{L-1}{D}}^{\frac{2L-2}{D}} \sum_{m=Dl-L+1}^{Dl} \sigma_m^2
$$
$$
+ \frac{\theta(N-1)q^2}{6} \sum_{l=0}^{\frac{2L-2}{D}} \sum_{m=Dl-L+1}^{Dl} \sigma_m^2. \qquad (4.21)
$$

Assuming the CIR obeys exponential decay as (4.15), (4.21) can be further simplified as (4.22). From (4.21), it is easy to observe that $\mathbb{E}[P_{quan}]$ is an increasing function of the quantization stepsize q.

$$
\mathbb{E}[P_{quan}] \approx \frac{\theta q^2 N \left(1 - e^{-\frac{LT_s}{\sigma_T}}\right)}{6\left(1 - e^{-\frac{T_s}{\sigma_T}}\right)} + \frac{\theta q^2 N \left[(L-1)\left(1 - e^{-\frac{DT_s}{\sigma_T}}\right) - De^{-\frac{T_s}{\sigma_T}} + De^{-\frac{LT_s}{\sigma_T}}\right]}{6D\left(1 - e^{-\frac{DT_s}{\sigma_T}}\right)\left(1 - e^{-\frac{T_s}{\sigma_T}}\right)}
$$
$$
+ \frac{\theta q^2 N \left[D\left(1 - e^{-\frac{(L-1)T_s}{\sigma_T}}\right) - (L-1)e^{-\frac{LT_s}{\sigma_T}}\left(e^{\frac{DT_s}{\sigma_T}} - 1\right)\right]}{6D\left(e^{\frac{DT_s}{\sigma_T}} - 1\right)\left(1 - e^{-\frac{T_s}{\sigma_T}}\right)}.
$$

$$(4.22)$$

4.3.3 Metric for Effective SINR Degradation

According to the definition of effective SINR in (4.10), the effective SINR gets degraded due to the nonzero stepsize q in (4.21). To better depicts the effect of quantization on the system performance, we introduce a new metric to characterize the degradation of effective SINR.

Considering an ideal TRDMA system with perfect waveform precision, the corresponding SINR, denoted as $SINR_p$, is defined as

$$SINR_p = \frac{\mathbb{E}[P_{sig}]}{\mathbb{E}[P_{isi}] + \mathbb{E}[P_{iui}] + 1}, \tag{4.23}$$

which is obviously larger than (4.10) in the system with limited waveform precision. By taking a ratio between (4.10) and (4.23), we have

$$\frac{SINR_i}{SINR_p} = \frac{1}{1 + \alpha}, \tag{4.24}$$

where α represents the significance of the quantization error compared with the interference-plus-noise in the TRDMA system, i.e.,

$$\alpha = \frac{\mathbb{E}[P_{quan}]}{\mathbb{E}[P_{isi}] + \mathbb{E}[P_{iui}] + 1}. \tag{4.25}$$

The α serves as a good metric to evaluate the system performance degradation due to the quantization. Based on (4.24), the larger α the further degradation of effective SINR due to quantization. In other words, if α keeps unchanged, no need to change about the quantization procedure to maintain the same level of system performance.

4.4 Number of Quantization Bits

In the previous sections, we have theoretically analyzed the degraded effective SINR due to the quantization. However, the previous analysis all depends on the quantization stepsize q. In practice, the number of quantization bits B is more important for the engineers to both implement the communication system and evaluate its complexity. Therefore, in the following, we will build the relationship between B and q given the uniform quantizer.

From (4.2), we know that each tap of the waveform is a CSCG random variable with zero mean and maximum variance $\max_i \sigma_i^2 / \sigma_s^2$. Considering the real and imaginary part quantization separately, the input into the quantizer can be treated as a Gaussian random variable with the maximum variance σ_{max}^2, e.g.,

$$\sigma_{max}^2 = \frac{\max_i \sigma_i^2}{2\sigma_s^2}. \tag{4.26}$$

Therefore, the probability that such a Gaussian input lies outside the range $[-2\sigma_{max}, 2\sigma_{max}]$ is less than 5%. Thus, we assume that the values of input lies within this range.

For a symmetric uniform quantizer with quantization step $q = m\sigma_{min}$, where $\sigma_{min}^2 = \frac{\min_i \sigma_i^2}{2\sigma_s^2}$, to cover the range of input values, $2 \left\lceil \frac{4\sigma_{max} - m\sigma_{min}}{2m\sigma_{min}} \right\rceil + 1$ quantization levels are required. Therefore, it is needed B bits each to represent the real and imaginary part of the waveform, where

$$B = \left\lceil \log_2 \left(2 \left\lceil \frac{4\sigma_{max} - m\sigma_{min}}{2m\sigma_{min}} \right\rceil + 1 \right) \right\rceil, \tag{4.27}$$

and the associated quantization stepsize is $q = m\sigma_{min}$.

4.5 Numerical Simulation

In this section, we conduct various numerical simulations to validate our theoretical analysis and explore the performance degradation due to quantization. First of all, we present some numerical evaluation of the effective SINR with different quantization stepsizes and system parameters. After that, we investigate the effect of system parameters (e.g. the number of users N, backoff factor D and quantization stepsize q) on α, which serves as the metric to characterize the performance loss due to the quantization. Finally, the bit-error-rate (BER) performance of the TRDMA system is evaluated with different number of quantization bits. Based on the simulation results, we try to answer the question that how many quantization bits are enough for the TRDMA system.

In the following simulations, we assume that the channel delay profiles follow the exponential decay as in [28]. The effective SINR and α are evaluated under various received signal-to-noise ratio (SNR) ρ, i.e.,

$$\rho = \frac{\theta N}{D} \sum_{l=0}^{L-1} \sigma_l^2, \tag{4.28}$$

with assumption of unity additive noise power.

4.5.1 Effective SINR Evaluation

In the first simulation, we evaluate the effective SINR performance under different quantization stepsize q, where we assume $\sigma_T = 256 T_s$, $L = 513$, $N = 2$ and $D = 1$. In Fig. 4.2, the solid curves are collected from simulation which numerically computes $\mathbb{E}\left[\frac{P_{sig}}{P_{isi}+P_{iui}+P_{quan}+1}\right]$ while dashed curves are obtained according to
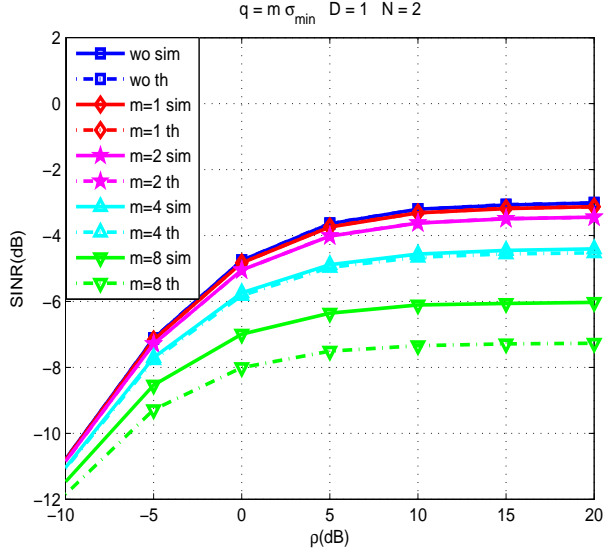
Figure 4.2: The effective SINR with $N = 2$, $D = 1$ and $q = m\sigma_{min}$.

the analytical results given by (4.14) and Theorem 1. Moreover, the quantization stepsize is chosen as $q = m\sigma_{min}$ and "wo" stands for the case without quantization error (perfect waveform precision). According to the analysis in Section V, $m = 1$, $m = 2$, $m = 4$ and $m = 8$ correspond to $B = 4$, $B = 3$, $B = 2$ and $B = 1$, respectively. From Fig. 4.2, we can see that the theoretical results match well with the numerical results when $q \leq 4\sigma_{min}$, which validates Theorem 1. The larger gap between theory and simulation when $m = 8$ is because Lemma 1 is accurate only when q is relatively small. We can also see from the figure that the effective SINR degrades with the increase of q compared with the case of prefect precision.

In the second simulation, we evaluate the effective SINR performance under different D, where we assume $\sigma_T = 256T_s$, $L = 513$, $N = 2$ and $q = 2\sigma_{min}$. The simulation results are shown in Fig. 4.3. Again, the solid curves stand for numerical results while the dashed curves represent the theoretical results. Based on the figure,
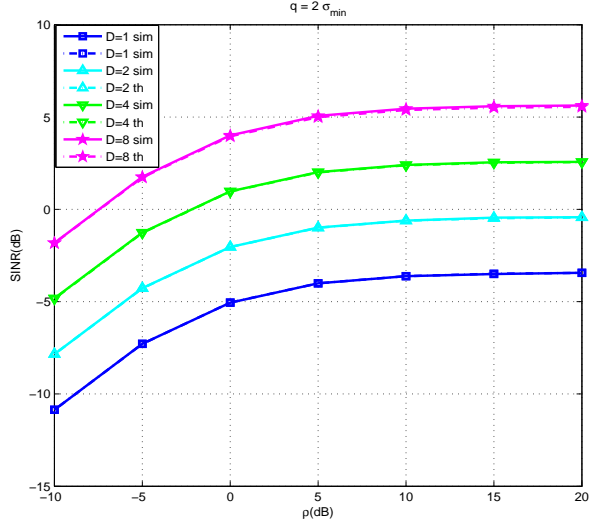
Figure 4.3: The effective SINR with $N = 2$, $q = 2\sigma_{min}$ and varying D.

our theoretical results match well with the numerical results given not too large q, regardless of other system parameters such as D. Note that even though the effective SINR increases with D due to the smaller ISI and IUI, the effective SINR cannot be significantly improved with even finer quantization, which also is implied in Fig. 4.2.

4.5.2 The Effect of System Parameters on α

As discussed in the previous subsection, α is a good numerical metric to characterize the effective SINR degradation due to quantization. From (4.25), α is affected by other system parameters, e.g. θ, D and N, given the fixed quantization stepsize q thus the number of quantization bits B. Based on this observation, it is interesting to explore the question that whether it is necessary to modify q and thus B in order to maintain the same level of degradation (same α) under different
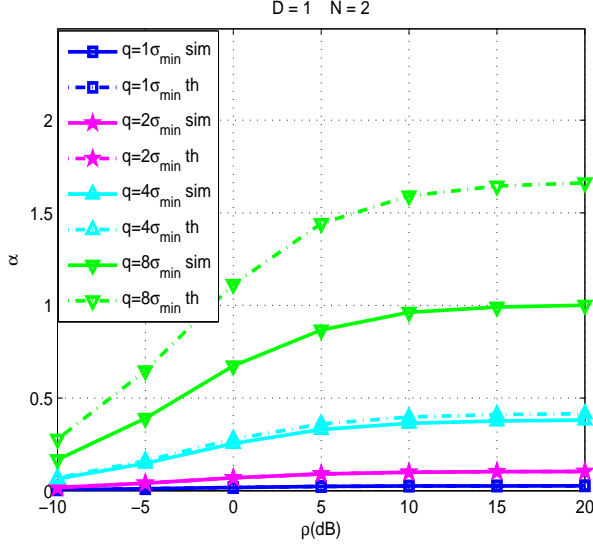
Figure 4.4: The α with $N = 2$, $D = 1$ and varying q.

system settings (e.g., θ, D and N). To answer this question, we have conducted the following simulations.

4.5.2.1 The effect of q on α

First, we evaluate the α with varying quantization stepsize q, where it is assumed that $\sigma_T = 256T_s$, $L = 513$, $N = 2$ and $D = 1$. In Fig. 4.4, the solid curves are collected from simulations while the dashed curves are obtained according to the analytical results given by Theorem 1. At the first glance, Fig. 4.4 indicates again that our theoretical analysis match well with the numerical simulations when q is small. Moreover, it can be seen from the figure that α increases with q given other system parameters, which is because, for a fixed SNR ρ, the terms in (4.14) are all fixed and $\mathbb{E}[P_{quan}]$ increases with q. In addition, the increase of α with q is not significant when q is small enough.
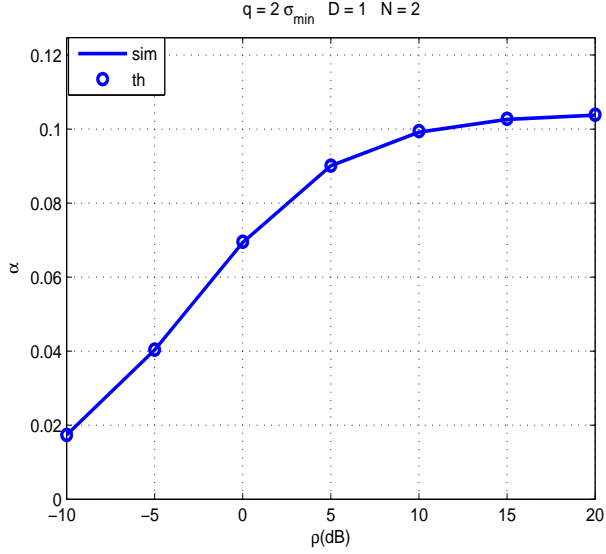
Figure 4.5: The α with $q = 2\sigma_{min}$, $N = 2$, $D = 1$ and varying θ.

4.5.2.2　The effect of θ on α

In the following, we evaluate the α with varying θ and thus associated ρ defined in (4.28), where it is assumed that $q = 2\sigma_{min}$, $\sigma_T = 256T_s$, $L = 513$, $N = 2$ and $D = 1$. The simulation results are shown in Fig. 4.5, where the solid curve stands for the numerical simulation results and the circle markers represent the theoretical results. From the figure, α increases with θ and the corresponding ρ. It is because that $\mathbb{E}[P_{quan}]$ becomes more significant compared with the unity power additive noise based on (4.25).

4.5.2.3　The effect of D on α

Compared with θ, we are more curious about the effect of D and N on α, since it will indicate whether we need to allocate more resource to maintain the same level of system performance under different system setting (e.g., a smaller D or a larger
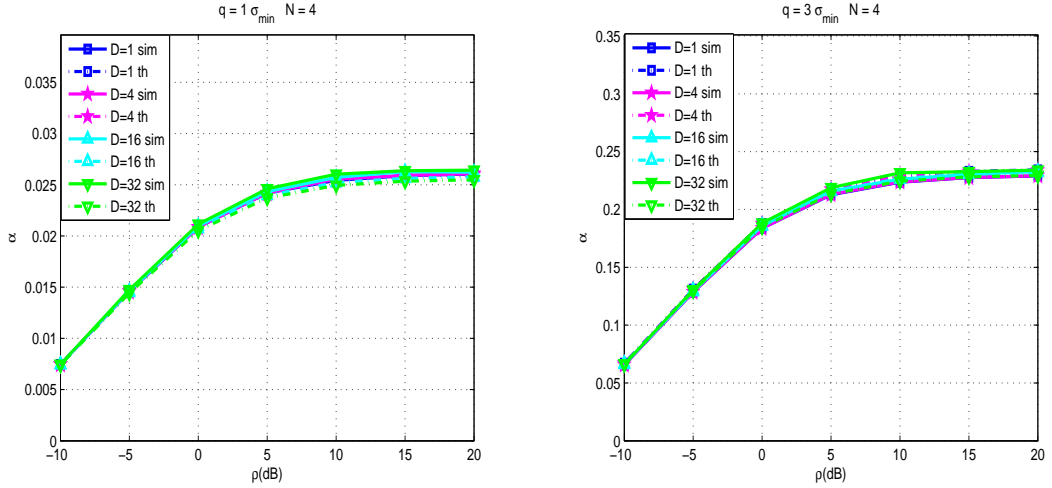
(a) $q = 1\sigma_{min}$. (b) $q = 3\sigma_{min}$.

Figure 4.6: The α with varying D.

N).

In the following, we evaluate the α with varying D, where it is assumed that

$\sigma_T = 256T_s$, $L = 513$ and $N = 4$. The results are summarized in Fig. 4.6, where

we evaluate two different quantization stepsizes $q = 1\sigma_{min}$ and $q = 3\sigma_{min}$ in the

subfigures (a) and (b). In Fig. 4.6(a), we evaluate the α with $D = 1$, $D = 4$,

$D = 16$ and $D = 32$, where the solid and dashed curves stand for the numerical and

theoretical results, respectively. From the figure, it can be observed that, with a

fixed SNR ρ, the α keeps the same value for various D. In other words, to maintain

the same level of system performance, the quantization stepsize q thus the number

of quantization bits B needs no modification for different backoff factors D.

Similar conclusion can be drawn from Fig. 4.6(b), even though the overall α

of the subfigure (b) is larger than that in (a) due to the larger q.

4.5.2.4 The effect of N on α

In mobile communications, the number of users N associated with a base station will always change with time. Therefore, it is of much importance to evaluate α with varying N. From the standpoint of system operator, it is reluctant to vary q and thus B to maintain the system performance just because of the varying N.

In the following, we evaluate the α with varying N, where it is assumed that $\sigma_T = 256T_s$, $L = 513$ and $q = 2\sigma_{min}$. The results are shown in Fig. 4.7, where we evaluate two different backoff factors $D = 1$ and $D = 4$ in the subfigures (a) and (b). In Fig. 4.7(a), we evaluate the α with $N = 1$, $N = 2$, $N = 4$ and $N = 8$, where the solid and dashed curves stand for the numerical and theoretical results, respectively. It can be seen from the figure, at the low SNR region, α increases with N. On the other hand, α keeps the same value for various N at high SNR region.

Similar observations can be seen from Fig. 4.7(b). Different from Fig. 4.6, the overall α in the two subfigures of Fig. 4.7 are the same, which further validates that D has no effect on α.

Remark: From the simulation results in Fig. 4.6 and Fig. 4.7, we have observed the effect of D and N on the value of α. Based on the physical meaning of α, it illustrates a good property in the TRDMA system with limited waveform precision, which is that after deciding the quantization stepsize q and thus B for a TRDMA system, there is no need to modify q and B to maintain the same level of system performance regardless of the changes in D. Even though a finer quantization is required for a large N to maintain the same α, such a requirement is not imperative

(a) $D = 1$.   (b) $D = 4$.
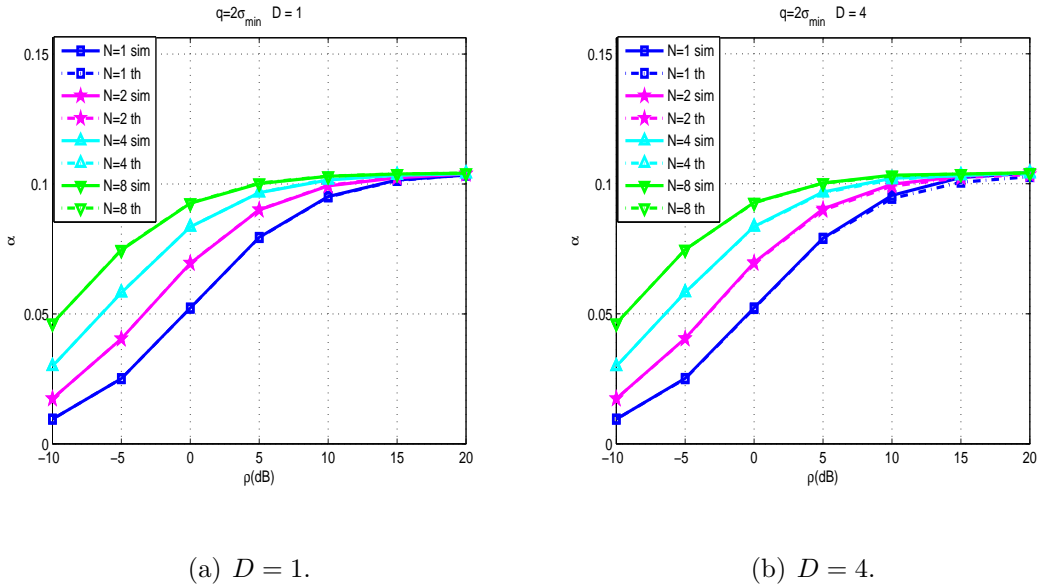
Figure 4.7: The α with varying N.

in high SNR region. These findings provide some guidance to the designer and operator for the TRDMA system.

4.5.3   Appropriate B for TRDMA System

Even though we have evaluated the degraded effective SINR and α in previous discussions, we have not concluded that how large B should be to maintain the almost perfect system performance. Therefore, in the following, we examine the appropriate B for a TRDMA system through investigating the BER performance with varying B. Specifically, we consider a TRDMA system with $\sigma_T = 256T_s$, $L = 513$, $D = 32$ and $N = 6$.

The BER performance under different B is shown in Fig. 4.8. In the figure, it is observed that the BER performance of TRDMA system saturates at the high SNR region due to the dominated ISI and IUI [69]. Moreover, from Fig. 4.8,
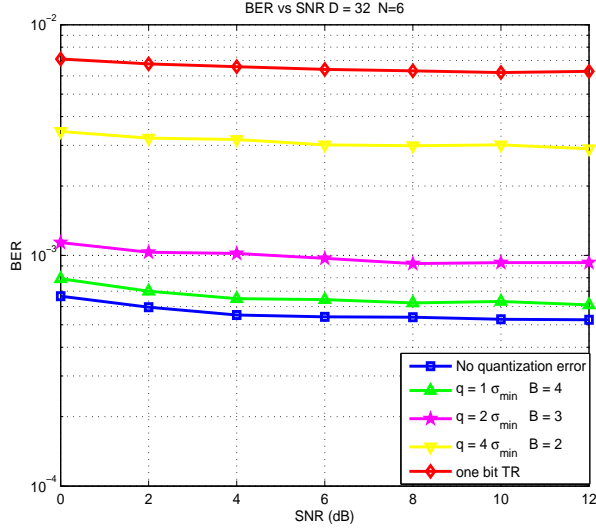
Figure 4.8: The BER performance with $N = 6$, $D = 32$ and varying B.

we can see that compared with the TRDMA system without quantization error (perfect precision), the BER performance of the so-called one-bit TR system actually degrades significantly. The BER performance gradually improves with the increase in B. It is because α significantly reduces with the smaller q, which is indicated in Fig. 4.4. We can observe from Fig. 4.8, the TRDMA system with $B = 4$ achieves the similar BER performance compared with the ideal scenario. In other words, 4-bit quantization is enough for a TRDMA system to eliminate the degradation due to the quantization.

4.6 Conclusion

In this chapter, we analyze the TRDMA system with limited waveform precision and studied the corresponding tradeoff between the complexity and performance. We derive an approximated closed-form expression of the effective SINR as

a function of quantization stepsize, according to which we investigate the number of quantization bits required for the TRDMA system to achieve reasonable performance. A metric α is proposed to depict the performance loss due to the quantization. Simulation results demonstrate that our theoretical analysis match well with the numerical results when the quantization stepsize is not too large. Through evaluating α with varying D and N, a promising property has been discovered that the number of quantization bits need no modification with varying D to maintain the same level of system performance. Finally, we conclude that 4-bit resolution for waveform is enough for the TRDMA system based on the BER performance evaluation.

Chapter 5

Enabling Heterogeneous Connectivity

Ubiquitous RFID tags, sensors, actuators, mobile phones and etc. cut across many areas of modern-day living, which offers the ability to measure, infer and understand the environmental indicators. The proliferation of these devices creates the term of the Internet of Things (IoT), wherein these devices blend seamlessly with the environment around us, and the information is shared across the whole platform [27].

The notion of IoT dates back to the 1999, when it was first proposed by Ashton [4]. Even though logistic is the originally considered application, in the past decade, the coverage of IoT has been extended to a wide range of applications including healthcare, utilities, transport, etc. [59]. Thanks to the significant maturity and market size of wireless communication technologies such as ZigBee, Bluetooth, Wi-Fi, and near-field communication (NFC), IoT is on the path of transforming the current static Internet into a fully integrated future Internet [10]. Due to its high impact on several aspects of everyday life and behavior of the potential users [5], IoT is listed as one of six "Disruptive Civil Technologies" by the US National Intelligence Council with potential impacts on US national power [45].

Considering the massive amount of devices and various application scenarios in

the IoT, the devices within the IoT are highly heterogeneous. From the perspective of communication, one of the significant heterogeneity is the bandwidth heterogeneity and thus the corresponding radio-frequency (RF) front-end. To address the bandwidth heterogeneity, various communication standards such as ZigBee, Bluetooth and Wi-Fi are adopted simultaneously in the current IoT platform, which leads to a wild growth of co-located wireless communication standards [18]. When multiple wireless communication standards are operated in the same geographical environment, the devices often suffer from harmful interference. Furthermore, the communication between devices with different communication standards is only possible through the use of gateway nodes, resulting in the fragmentation of the whole network, hampering the objects interoperability and slowing down the development of a unified reference model for IoT [72].

To enable the connectivity between devices with various bandwidths, some existing works build middlewares to hide the technical details of different communication standards from the application layer. In [16], Service Oriented Device Architecture (SODA) is proposed as a promising approach to integrate Service Oriented Architecture (SOA) principles into the IoT. An effective SOA-based integration of IoT is illustrated in enterprise service [58]. Business Process Execution Language (BPEL) has been widely used as the process language in the middleware [51]. However, these technologies used to realize middleware architectures are often not suitable for resource-constrained scenario due to their complexity.

Instead of building middlewares, is there any other more effective approach to enable the connectivity between the devices with different bandwidths? We try

to answer this question by proposing the time-reversal (TR) approach. It is well known that radio signals will experience many multipaths due to the reflection from various scatters, especially in indoor environments. Through time-reversing (and conjugate, when complex-valued) the multipath profile as the beamforming waveform, TR technique can constructively add up the signals of all the paths at the intended location, ending up with a spatio-temporal resonance effect [65]. As pointed out in [65], the TR technique is an ideal candidate for low-complexity, low energy consumption green wireless communication because of its inherent nature to fully harvest energy from all the paths. A TR-based multiuser media access scheme is proposed in [28], where only the simple detection based on a single received symbol is needed at the device side resulting in low computational complexity and low cost of the terminal devices. With the waveform determined by the physical location, TR technique can provide additional physical-layer security and thus can enhance the privacy and security of customers in IoT. An overview of the TR wireless paradigm for green IoT has been presented in [13] summarizing all the promising features of TR technique. However, they cannot be directly applied to address the bandwidth heterogeneity in IoT, because of the implicit assumption that all terminal devices share the same bandwidth and thus the RF front-end.

In order to support devices with various bandwidths in IoT, a novel TR-based heterogeneous system is proposed in this chapter, where a bank of various pulse-shaping filters are implemented to support data streams of different bandwidths. By integrating the multirate signal processing into TR technique, the proposed system is capable to support these heterogeneous devices with a single set of RF front-end,

therefore it is a unified framework for connecting devices of heterogeneous bandwidths. As shown in Fig. 5.1, instead of connecting devices with different wireless communication standards through gateways and middlewares, the TR-based heterogeneous system in this chapter directly links the devices together. The increase of complexity in the proposed system lies in the digital processing at the access point (AP), instead of at the devices' ends, which can be easily handled with more powerful digital signal processor (DSP). Meanwhile, the complexity of the terminal devices stays low and therefore satisfies the low-complexity and scalability requirement of IoT. Since there is no middleware in the proposed scheme and the additional physical layer complexity concentrates on the AP side, the proposed heterogeneous TR system better satisfies the low-complexity and energy-efficiency requirement for the terminal devices (TDs) compared with the middleware approach. Theoretical analysis of the interference is further conducted to predict the system performance. Simulation results show that the proposed system can support the devices of heterogeneous bandwidths with a reasonable bit-error-rate (BER) performance. In addition, the BER performance can be significantly improved with the appropriate spectrum allocation.

The rest of the chapter is organized as follows. In Section 5.1, the system architecture and working scheme of the existing homogeneous TR system are introduced. Section 5.2 describes a TR-based heterogeneous system based on the existing TR system. The analysis of regarding the interference in the proposed system is derived in Section 5.3. In Section 5.4, simulation results about the BER performance of the system are discussed. Finally, the conclusion is drawn in Section 5.5.
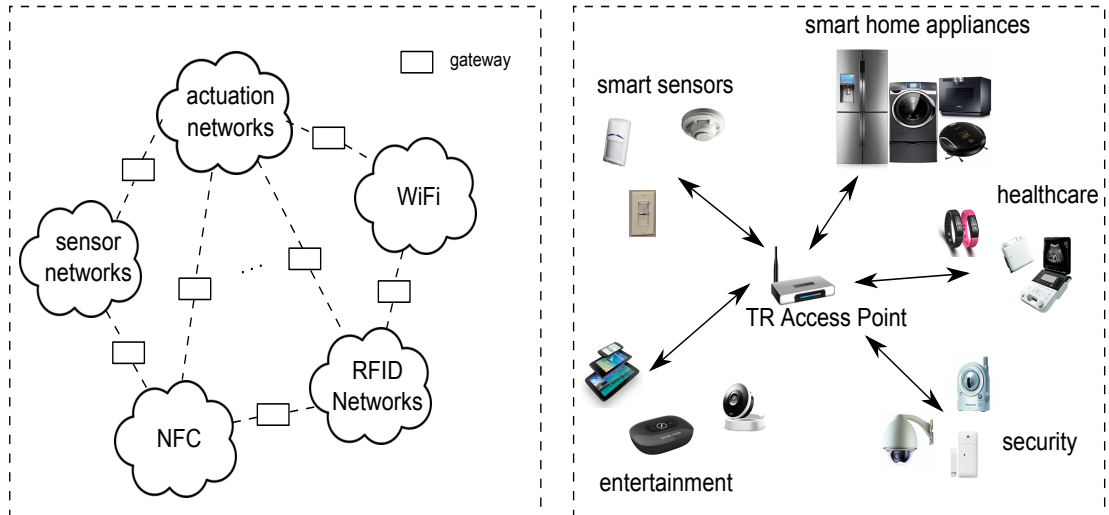
(a) An illustration of current IoT approach.   (b) An illustration of heterogeneous TR-based

IoT approach.

Figure 5.1: Comparison between existing IoT approach and heterogeneous TR-based

IoT approach.

5.1 Typical Homogeneous Time-Reversal System

In this section, we will first introduce the system architecture and working

mechanism of the TR-based homogenous system, where the AP and all terminal

devices (TDs) share the same spectrum thus the bandwidth and ADC sample rate.

A typical TR-based homogenous system is shown in Fig. 5.2 [28]. The channel

impulse response (CIR) between the two transceivers is modeled as

$$h(t) = \sum_{v=1}^{V} h_v \delta(t - \tau_v), \tag{5.1}$$

where h_v is the complex channel gain of vth path of the CIR, τ_v is the corresponding

path delay, and V is the total number of the independent multipaths in the envi-

ronment (assuming infinite system bandwidth and time resolution). Without loss

of generality, we assume that $\tau_1 = 0$ in the rest of chapter, i.e., the first path arrives
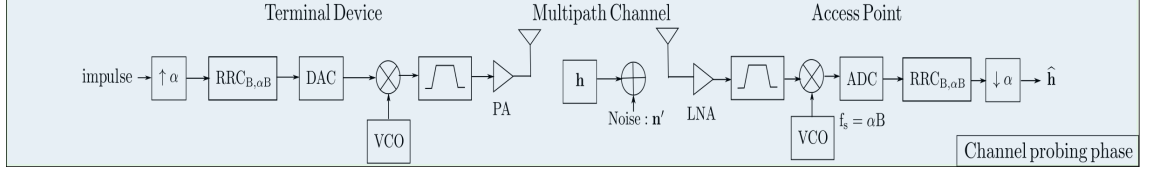
(a) Channel Probing Phase.
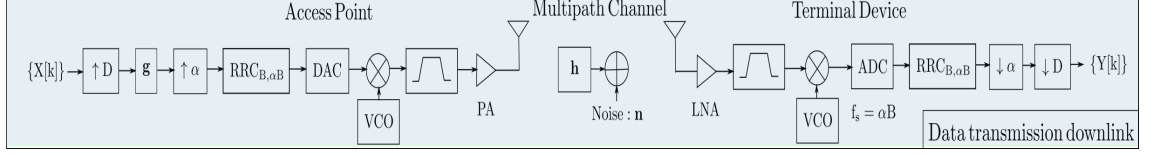
(b) Data Transmission Downlink.
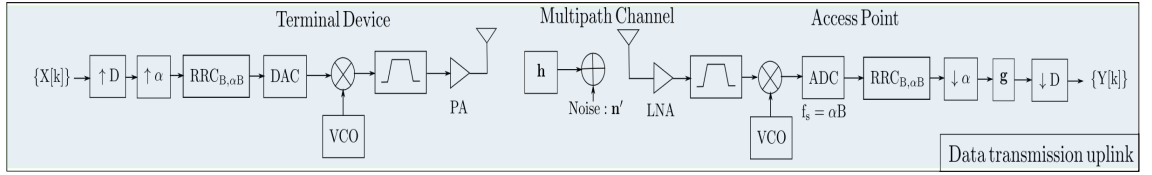
(c) Data Transmission Uplink.

Figure 5.2: Typical Homogeneous TR System.

at time $t = 0$, and as a result, the delay spread of the multipath channel τ_C is given

by $\tau_C = \tau_V - \tau_1 = \tau_V$.

Considering the practical communication system with limited bandwidth, pulse

shaping filters are typically deployed to limit the effective bandwidth of transmission.

In practice, raised-cosine filter is typically utilized as a pulse shaping filter which

minimizes the inter-symbol-interference (ISI) [25]. Generally, the raised-cosine filter

is splitted into two root-raised-cosine filters $\mathbf{RRC}_{B,f_s}[n]$ and deployed at each side

of the transceivers, where B is the available bandwidth and f_s is the sample rate of

the system. Based on the Nyquist rate [49], an α-times oversampling (i.e. $f_s = \alpha B$)

is practically implemented to counter the sampling frequency offset (SFO).

5.1.1 Channel Probing Phase

As shown in Fig. 5.2(a), prior to AP's TR-transmission, an impulse is upsampled by α, filtered by $\mathbf{RRC}_{B,f_s}[n]$ and transmitted out after going through the RF components at the TD side. The transmitted signal propagates to AP through the multipath channel $h(t)$, where AP samples the received signal. Then the sampled signal goes through RF components, which later is filtered by another $\mathbf{RRC}_{B,f_s}[n]$, downsampled by α, and finally recorded as the estimated CIR $\widehat{\mathbf{h}}$.

With sample rate $f_s = \alpha B$, the discrete CIR can be written as

$$\overline{h}[n] = \sum_{v=1}^{V} h_v \delta[nT_s - \tau_v], \tag{5.2}$$

where $T_s = 1/(\alpha B)$. Assume perfect channel estimation (noise and interference are ignored in the channel probing phase), the equivalent CIR between two RRC filters in Fig. 5.2(a) is written as

$$\widetilde{\mathbf{h}} = \left(\mathbf{RRC}_{B,f_s} * \overline{\mathbf{h}} * \mathbf{RRC}_{B,f_s}\right). \tag{5.3}$$

Based on the polyphase identity [62], the equivalent CIR (between the expander and decimator) for the system with bandwidth B can be represented as

$$\widehat{\mathbf{h}} = \left(\mathbf{RRC}_{B,f_s} * \overline{\mathbf{h}} * \mathbf{RRC}_{B,f_s}\right)_{[\alpha]}, \tag{5.4}$$

where $(\cdot)_{[\alpha]}$ represents α-times decimation. From (5.4), one can see that those paths in (5.2), whose time differences are within the main lobe of raised-cosine filter, are mixed together for the system with a limited bandwidth B.

5.1.2 Data Transmission Phase

Upon acquiring the equivalent CIR $\widehat{\mathbf{h}}$, different designs of waveforms (e.g. basic TR waveform [65], ZF waveform [15], and MMSE waveform [69]) can be implemented at the AP side. With no loss of generality, the basic TR waveform is considered in the rest of chapter. In other words, the AP time-reverses (and conjugate, when complex-valued) the equivalent CIR $\widehat{\mathbf{h}}$, and uses the normalized TR waveform as the basic TR waveform $\mathbf{g}$, i.e.,

$$g[n] = \frac{\widehat{h}^*[L-1-n]}{\|\widehat{\mathbf{h}}\|}, \tag{5.5}$$

where L is the number of taps in $\widehat{\mathbf{h}}$.

According to Fig. 5.2(b), there is a sequence of information symbols $\{X[k]\}$ to be transmitted to the TD. Typically, the symbol rate can be much lower than the system chip rate $(1/B)$. Therefore, a rate backoff factor D is introduced to match the symbol rate with chip rate by inserting $(D-1)$ zeros between two symbols [22, 28, 65], i.e.,

$$X^{[D]}[k] = \begin{cases} X[k/D], & \text{if } (k \bmod D) = 0, \\ \\ 0, & \text{if } (k \bmod D) \neq 0, \end{cases} \tag{5.6}$$

where $(\cdot)^{[D]}$ denotes the D-times interpolation. Consequently, the waveform embedded symbols before the α-times expander can be written as

$$S[k] = \left(\mathbf{X}^{[D]} * \mathbf{g}\right)[k]. \tag{5.7}$$

Based on the previous derivation in the channel probing phase, the system components between the expander and decimator in Fig. 5.2(b) can be replaced by $\widehat{\mathbf{h}}$.

Therefore, the signal received at the TD side before the decimator with rate D is the convolution of $S[k]$ and $\widehat{\mathbf{h}}$, plus additive white Gaussian noise (AWGN) $\widetilde{n}[k]$ with zero-mean and variance σ_N^2, i.e.,

$$Y^{[D]}[k] = \left(\mathbf{S} * \widehat{\mathbf{h}} \right)[k] + \widetilde{n}[k]. \tag{5.8}$$

Then, TD decimates the symbols with backoff factor D in order to detect the information symbols $\{X[k]\}$, i.e.,

$$\begin{aligned}
Y[k] = {} & \sqrt{p_u}(\widehat{\mathbf{h}} * \mathbf{g})[L-1]X[k - \frac{L-1}{D}] \\
& + \sqrt{p_u} \sum_{l=0, l \neq (L-1)/D}^{(2L-2)/D} (\widehat{\mathbf{h}} * \mathbf{g})[Dl]X[k-l] + n[k],
\end{aligned} \tag{5.9}$$

where $n[k] \triangleq \widetilde{n}[Dk]$ and p_u stands for the power amplifier.

Benefiting from temporal focusing, the power of $(\widehat{\mathbf{h}} * \mathbf{g})$ achieves its maximum at $(L-1)$ for $X[k - \frac{L-1}{D}]$, i.e.,

$$(\widehat{\mathbf{h}} * \mathbf{g})[L-1] = \frac{\sum_{l=0}^{L-1} \widehat{h}[l]\widehat{h}^*[l]}{\|\widehat{\mathbf{h}}\|} = \|\widehat{\mathbf{h}}\|. \tag{5.10}$$

Consequently, the resulting signal-to-interference-plus-noise ratio (SINR) is obtained as

$$\text{SINR} = \frac{p_u \|\widehat{\mathbf{h}}\|^2}{p_u \sum_{l=0, l \neq (L-1)/D}^{(2L-2)/D} |(\widehat{\mathbf{h}} * \mathbf{g})[Dl]|^2 + \sigma_N^2}, \tag{5.11}$$

assuming that each information symbol $X[k]$ has unit power.

Regarding the uplink, the previously designed waveform $\mathbf{g}$ serves as the equalizer at the AP side as shown in Fig. 5.2(c). Similar to the signal flow in the downlink scheme, the AP can detect the information symbol based on the temporal focusing of $(\widehat{\mathbf{h}} * \mathbf{g})$ in the uplink. Such a scheme of both downlink and uplink is defined as

the asymmetric architecture, which provides the asymmetric complexity distribution between the AP and TD. In other words, the design philosophy of uplink is to keep the complexity of terminal users at minimal level.

Note that the homogeneous TR system can be easily extended to multi-user scenario according to the previous work [28], which exploits the spatial degrees of freedom in the environment and uses the multipath profile associated with each user's location as a location-specific waveform for the user. In addition, different users are allowed to adopt different rate backoff factors to accommodate the heterogeneous QoS requirements for various applications in the IoT.

Remark: Even though the homogeneous TR system can support different QoS through varying D, all devices in the system must share the same bandwidth thus the sample rate, which increases the not only hardware cost but also computation burden for those low-end TDs. Besides the heterogenous QoS required by very diverse applications, the definition of heterogeneity in IoT should also cover the heterogeneous hardware capabilities (such as bandwidth, sample rate, computational and storage power and etc.), which apparently is not supported by the homogeneous TR system. Such more general heterogeneity requirement in the IoT motivates the heterogenous TR paradigm in this chapter.

5.2 Heterogenous Time-Reversal System

Even though the homogeneous TR system cannot handle bandwidth heterogeneity, the majority of challenges in the IoT can be tackled simultaneously through
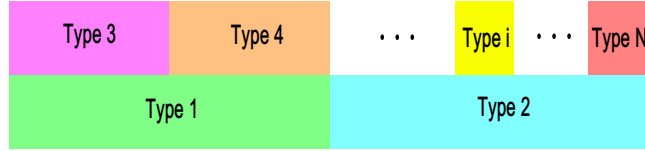
Figure 5.3: Spectrum Occupation of Heterogeneous TDs.
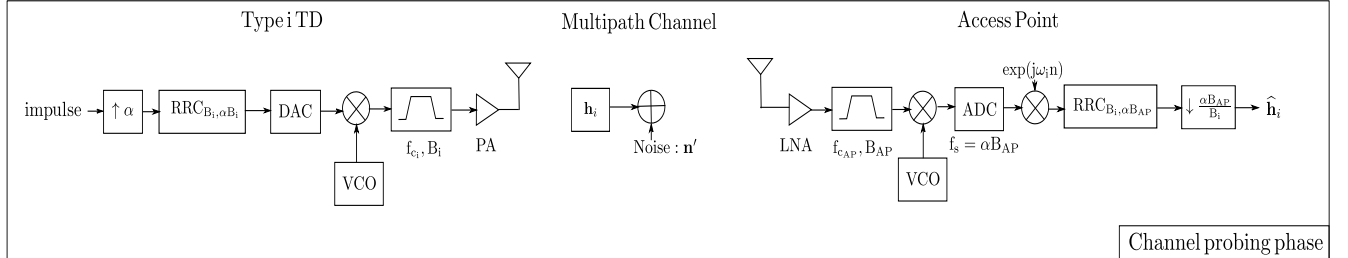
Figure 5.4: Channel Probing of Type i TD in Heterogeneous TR System.

the TR technique [13]. Does there exist an efficient way to modify the existing homogenous TR system to handle the bandwidth heterogeneity while maintaining the most benefit of the TR technique? The answer is yes and the heterogeneous TR system is potentially the best candidate to address the issue.

In contrast with the same spectrum occupation of all devices in the homogenous setting, N types of TDs with distinct spectrum allocation and bandwidths are supported simultaneously by a single AP in the heterogenous TR system. In other words, different types of TDs have the distinct carrier frequency (f_{c_i}) and bandwidth (B_i) as shown in Fig. 5.3.

5.2.1   Modifications on Homogenous TR System

In order to support the heterogenous TDs, several modifications need to be conducted at both AP and TD sides of the existing homogeneous TR system.

100

5.2.1.1 TD Side

As stated before, heterogeneous TDs of different types have distinct f_{c_i}'s and B_i's. First of all, the radio-frequency (RF) components of different types have to be distinct. Specifically, the oscillation frequency of the voltage-controlled oscillator (VCO) at type i TD is set to f_{c_i} and the bandwidth of analog bandpass filter is B_i. Then, the ADC deployed for type i TDs has the sample rate of $f_{s_i} = \alpha B_i$ based on the previous discussion. Furthermore, various root-raised-cosine filters for different types are required, i.e., $\mathbf{RRC}_{B_i, f_{s_i}}$.

5.2.1.2 AP Side

In order to support heterogeneous TDs simultaneously, the bandwidth of AP, denoted as B_{AP}, is the aggregated version of the bandwidth of all heterogeneous TDs. Even though more complicated digital signal processing is enforced to handle different data streams for various types, only one set of RF components is needed at the AP side. The digital signal processing includes frequency shift, rate convertor and root-raised-cosine filter. More specifically, a frequency shift component $\exp^{j\omega_i n}$ is implemented for each type to support multiple carrier frequencies. A distinct sample rate convertor (expander or decimator) with rate $\alpha B_{AP}/B_i$ is deployed for each type i to enable the multirate processing. The root-raised-cosine filter $\mathbf{RRC}_{B_i, \alpha B_{AP}}$ for type i is utilized to limit the effective bandwidth of signals for the heterogeneous TDs.

In the following, the detailed system mechanism together with the modified

system architecture is developed for the proposed heterogeneous TR system.

5.2.2 Channel Probing Phase

The channel probing phase of a type i TD is shown in Fig. 5.4. Compared with the one in Fig. 5.2(a), there exists some differences mentioned in the last subsection. Prior to the data transmission phase, an impulse is upsampled by α, filtered by $\mathbf{RRC}_{B_i, \alpha B_i}[n]$ and transmitted out after going through the RF components at the TD side. The transmitted signal propagates to AP through the multipath channel $h_i(t)$, where AP samples the received signal with a higher sample rate $f_s = \alpha B_{AP}$, shifts the signal to baseband (based on the difference between f_{c_i} and $f_{c_{AP}}$), filters it through the other matched $\mathbf{RRC}_{B_i, \alpha B_{AP}}[n]$, downsamples the waveform by $\alpha B_{AP}/B_i$, and finally records the downsampled waveform as $\widehat{\mathbf{h}}_i$.

With sample rate $f_s = \alpha B_{AP}$, the discrete CIR can be written as

$$\overline{h}_i[n] = h_i(nT_s), \tag{5.12}$$

where $T_s = 1/(\alpha B_{AP})$.

Since the digital-to-analog convertor (DAC) serves the interpolator, the transmitted signal of the TD shown in Fig. 5.4 is mathematically equivalent to that generated through the following process, i.e., upsampled by $\alpha B_{AP}/B_i$, filtered by $\mathbf{RRC}_{B_i, \alpha B_{AP}}[n]$ and converted to analog signal by the DAC. Therefore, similarly according to the polyphase identity, the equivalent CIR for the type i TD with bandwidth B_i can be expressed as

$$\widehat{\mathbf{h}}_i = \sqrt{\beta_i}\big(\mathbf{RRC}_{B_i,\alpha B_{AP}} * \overline{\mathbf{h}}_i * \mathbf{RRC}_{B_i,\alpha B_{AP}}\big)_{[\alpha\beta_i]}, \qquad (5.13)$$

where $\beta_i = B_{AP}/B_i$ and $\sqrt{\beta_i}$ is used to compensate the power difference between $\mathbf{RRC}_{B_i,\alpha B_i}[n]$ and $\mathbf{RRC}_{B_i,\alpha B_{AP}}[n]$.

Even though the channel probing of a single type is evaluated here, it can be extended straightforward to multi-type TDs by deploying different digital processing for multi-type in parallel, e.g., frequency shift, RRC filtering and downsampling with type-specific factor. In other words, the AP can support heterogeneous TDs with one single set of RF components but more complicated digital processing.

5.2.3   Data Transmission Phase

Suppose N types of TDs are communicating with the AP simultaneously, where the number of TDs in type i is denoted as M_i. Upon acquiring the equivalent CIRs, the waveform $\mathbf{g}_{i,j}$ is designed for j^{th} TD in the type i with various existing design methods. Take the basic TR waveform design for example, i.e.,

$$g_{i,j}[n] = \frac{\widehat{h}_{i,j}^*[L-1-n]}{\|\widehat{\mathbf{h}}_{i,j}\|}, \qquad (5.14)$$

where $\widehat{\mathbf{h}}_{i,j}$ is defined in (5.13).

First, the downlink data transmission is considered. As shown in Fig. 5.5(a), let $\{X_{i,j}[k]\}$ be the the sequence of information symbols transmitted to the jth TD in type i. Similar to the case in the homogeneous TR system, a rate backoff factor $D_{i,j}$ is introduced to adjust the symbol rate, i.e., the symbol rate for j^{th} TD in the type i is $(B_i/D_{i,j})$. Then, the waveform $\mathbf{g}_{i,j}$ is embedded into the TD-specific data

stream $\mathbf{X}_{i,j}^{[D_{i,j}]}$ and the waveform embedded symbols of the same type i are merged together as $\mathbf{S}_i$, e.g.,

$$\mathbf{S}_i = \sum_{j=1}^{M_i} \left(\mathbf{X}_{i,j}^{[D_{i,j}]} * \mathbf{g}_{i,j} \right). \tag{5.15}$$

Later, the merged symbols $\mathbf{S}_i$ go through the type-specific digital signal processing, i.e., upsampled with factor $\alpha B_{AP}/B_i$, filtered by $\mathbf{RRC}_{B_i,\alpha B_{AP}}$ and carried to the type-specific digital frequency with frequency shift $\exp(-j\omega_i n)$. In the end, the processed data streams of N types are mixed together and broadcasted to all the heterogeneous TDs through one set of RF components at the AP.

Regarding the receiver side, the jth TD in type i is taken as an example. The broadcast signal propagates to the TD through the multipath profile $h_{i,j}(t)$. Later, the signal passes through the analog bandpass filter centering at f_{c_i} with bandwidth B_i. Note that the filtered signal includes not only the intended signal but the interference, e.g., the inter-user-inference (IUI) from the TDs within the same type and the inter-type-interference (ITI) from the other types (whose spectrum overlaps with type i). Thanks to the spatio-temporal focusing effect, the interference is suppressed due to the unique multipath profile. Afterwards, the signal is carried to baseband and sampled with a sample rate $f_{s_i} = \alpha B_i$, which is much smaller than that at the AP for the low-end TDs. In the end, the sampled signal goes through $\mathbf{RRC}_{B_i,\alpha B_i}$ and the rate matching decimator to generate symbols $\{Y_{i,j}[k]\}$, based on which $\{X_{i,j}[k]\}$ are detected. The theoretical analysis regarding the signal-to-interference-plus-noise ratio (SINR) will be derived in the next section.

The system architecture of uplink is shown in Fig. 5.5(b). From the figure, the

(a) Downlink.

(b) Uplink.

Figure 5.5: Data Transmission in Heterogeneous TR System.

property of asymmetric architecture is preserved in the heterogeneous TR system. Same to the homogeneous TR system, the precoding waveforms $\mathbf{g}_{i,j}$'s in the downlink serve as the equalizers in the uplink. After converting the signal into digital domain through a single set of RF components at the AP, multiple parallel digital processing (e.g., frequency shift, RRC filtering and rate conversion) is required to support N types of TDs simultaneously.

Remark: Compared with the existing homogeneous TR system, the heterogenous TR system maintains the capability to support different QoS through not only varying the backoff factor $D_{i,j}$ but providing the flexibility for TDs to select various B_i's. More importantly, the heterogeneous TR system architecture further promotes the benefit of the asymmetric complexity. In other words, the new modifications enhance the concentration of the complexity at the AP side. Regarding the AP, a single set of RF components is required. Even though more complicated parallel digital signal processing is needed, it can be easily satisfied with more powerful D-SP unit at an affordable cost and complexity. Regarding the heterogeneous TDs, the ADC sample rate is reduced significantly for those devices with smaller bandwidth, which lowers down the cost of hardware dramatically for the low-end TDs. In addition, the lower sample rate naturally decreases the computational burden as well.

Compared with the middleware approach, the proposed TR approach has two main advantages. First, the proposed TR approach serves a unified system model for IoT, while middleware leads to the fragmentation of the whole network due to the coexistence of different communication standards. Moreover, by concentrating the

complexity at the AP, the proposed TR approach better satisfies the requirement of low-complexity and energy-efficiency at the TDs since no middleware needs to be implemented on the TD side.

5.3 Performance Analysis of Heterogeneous TR System

In this section, we conduct some theoretic analysis on the proposed heterogeneous TR system and evaluate the SINR for the individual TD. Without loss of generality, the downlink scenario is investigated here. Due to the asymmetric architecture and channel reciprocity, the uplink scenario can be analyzed similarly. In the following, two special cases in the heterogeneous TR system are first studied. Then, the analysis of a specific TD in the general setting is derived through extending the results of the special cases.

5.3.1 Overlapping Case

First, a special case of heterogenous TR system is considered. Suppose there are only two types of TDs in the system, e.g., type i and type k. As shown in Fig. 5.6, both types share the same carrier frequency with AP, whose spectrum is overlapped. Without loss of generality, only a single TD is assumed to exist within each type.

In this special case, the downlink system architecture in Fig. 5.5(a) can be significantly simplified. In the first place, the frequency shift can be removed due to the same carrier frequency. Moreover, the analog bandpass filter could also be
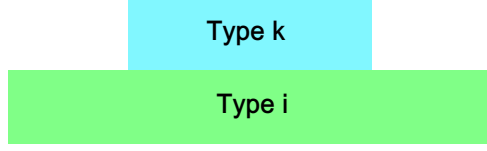
Figure 5.6: Spectrum Occupation of Case I

ignored in the analysis since the effective bandwidth has already been limited by the RRC filters. Denote $\widehat{\mathbf{h}}_{a,b}$ as the equivalent CIR for the type a symbols sent from the AP to the type b TD. Based on (5.4), we have

$$\widehat{\mathbf{h}}_{a,a} = \sqrt{\beta_a}\big(\mathbf{RRC}_{B_a,\alpha B_{AP}} * \overline{\mathbf{h}}_a * \mathbf{RRC}_{B_a,\alpha B_{AP}}\big)_{[\alpha\beta_a]}. \tag{5.16}$$

In addition, the equivalent CIR for interference can be derived as follows through utilizing the noble identities [62],

$$\widehat{\mathbf{h}}_{a,b} = \Big(\mathbf{RRC}_{B_a,\alpha B_{AP}} * \overline{\mathbf{h}}_b * \mathbf{RRC}^{[\beta_b]}_{B_b,\alpha B_b}\Big)_{[\alpha]}, \tag{5.17}$$

where $a,b \in \{i,k\}$, $\beta_a = B_{AP}/B_a$ and $\overline{\mathbf{h}}_a$ is the discrete CIR from the AP to the type a TD with sample rate $f_s = \alpha B_{AP}$.

Upon acquiring the equivalent CIRs, the waveform for each type is designed, e.g.,

$$g_a[n] = \frac{\widehat{h}^*_{a,a}[L-1-n]}{\|\widehat{\mathbf{h}}_{a,a}\|}, \tag{5.18}$$

where $a \in \{i,k\}$. Note that there exists focusing effect of the term $(\mathbf{g}_a * \widehat{\mathbf{h}}_{a,a})$ based on (5.18). Therefore, the simplified system model is shown in Fig. 5.7 base on the equations above.

(a) Equivalent Data Stream for Type i. (b) Equivalent Data Stream for Type k.
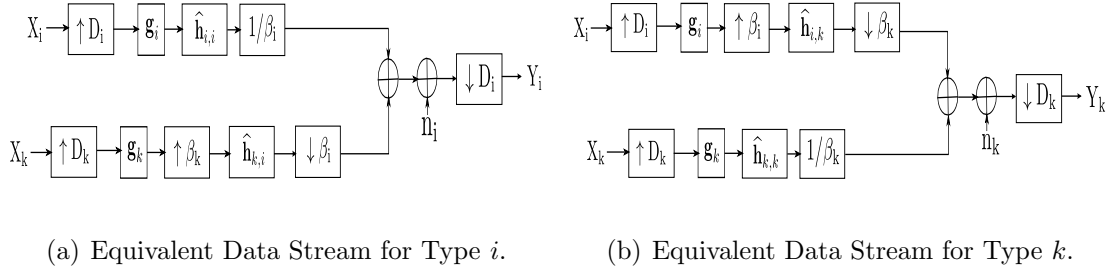
Figure 5.7: Equivalent Architecture in Case I.

From the figure, the received symbols at type i TD can be expressed as

$$
\begin{aligned}
Y_i[n] = {} & \frac{\sqrt{p_u}}{\beta_i} \left(\mathbf{g}_i * \widehat{\mathbf{h}}_{i,i} \right) [L_i - 1] X_i[n - \frac{L_i - 1}{D_i}] \\
& + \frac{\sqrt{p_u}}{\beta_i} \sum_{l=0, l \neq (L_i-1)/D_i}^{(2L_i-2)/D_i} \left(\mathbf{g}_i * \widehat{\mathbf{h}}_{i,i} \right) [D_i l] X_i[n - l] \\
& + \sqrt{p_u} \sum_{l=0}^{(L_{k,i}-1)/(\beta_k D_k)} \left(\mathbf{g}_k^{[\beta_k]} * \widehat{\mathbf{h}}_{k,i} \right) [\beta_k D_k l] X_k[n - l] \\
& + n_i[n],
\end{aligned}
\tag{5.19}
$$

where p_u is the power amplifier, $L_i = \text{length} \left(\widehat{\mathbf{h}}_{i,i} \right)$ and $L_{k,i} = \text{length} \left(\mathbf{g}_k^{[\beta_k]} * \widehat{\mathbf{h}}_{k,i} \right)$.

In (5.19), the first and second term are the typical expected signal term and ISI term, respectively. In addition, the third term is the inter-type-interference (ITI) from the type k TD. Moreover, based on the spatio-temporal focusing effect in the TR system, the ITI is suppressed naturally with the location-specific waveform. A similar equation of the received symbols can be derived for the type k TD.

Since the frequency shift $\exp^{-j\omega_i n}$ has unitary power, the analysis in (5.19) is also applied for the case where the carrier frequency of type i and k are different as long as their spectrum is overlapped.

Type i	Type k
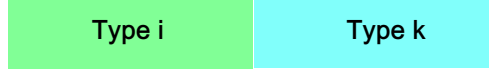
Figure 5.8: Spectrum Occupation of Case II

5.3.2 Non-overlapping Case

Another special case, where the spectrum of different types is non-overlapped, is considered in this subsection. Suppose two types of TDs exist in the system, e.g., type i and type k, each of which contains a single TD. As shown in Fig. 5.8, there are no ITI between non-overlapped types due to the corresponding analog bandpass filters and RRC filters. Therefore, the analysis becomes straightforward and the received symbols at type i TD is derived as,

$$
\begin{aligned}
Y_i[n] = {} & \frac{\sqrt{p_u}}{\beta_i} \left(\mathbf{g}_i * \widehat{\mathbf{h}}_{i,i} \right) [L_i - 1] X_i[n - \frac{L_i - 1}{D_i}] \\
& + \frac{\sqrt{p_u}}{\beta_i} \sum_{l=0, l \neq (L_i-1)/D_i}^{(2L_i-2)/D_i} \left(\mathbf{g}_i * \widehat{\mathbf{h}}_{i,i} \right) [D_i l] X_i[n - l] \\
& + n_i[n],
\end{aligned}
\tag{5.20}
$$

which is well studied in the homogeneous TR system [65].

5.3.3 Mixed Case

Based on the previous analysis of two special cases, the heterogeneous TR system is analyzed under the general scenario, where N types of TDs are supported in the system and the number of type i TD is M_i. The spectrum of different types is shown in Fig. 5.3.

110

As discussed in Section 5.2, $\{X_{i,j}[k]\}$ denotes the information symbols for the jth TD in type i, and $D_{i,j}$ and $\mathbf{g}_{i,j}$ are the backoff factor and the embedded waveform for the symbols $\{X_{i,j}[k]\}$, respectively. Based on Section 5.3.1, the TDs in type i suffer ITI from type k TDs, where $k \in T_i$ and T_i denotes the set of types whose spectrum is overlapped with type i. In other words, the data streams of type k, where $k \notin T_i$, causes no interference to type i TDs according to Section 5.3.2.

Regarding the CIR, denote $\overline{\mathbf{h}}_{i,j}$ as the discrete CIR from the AP to the jth TD in type i with sample rate $f_s = \alpha B_{AP}$. Moreover, let $\widehat{\mathbf{h}}_{i_m,k_n}$ be the equivalent CIR for the data stream of mth TD in type i between the AP to n^{th} TD in type k. Similar to (5.16) and (5.17), the equivalent CIR for data streams can be derived as

$$
\widehat{\mathbf{h}}_{i_m,k_n} = \begin{cases} \sqrt{\beta_i}\big(\mathbf{RRC}_{B_i,\alpha B_{AP}} * \overline{\mathbf{h}}_{i,n} * \mathbf{RRC}_{B_i,\alpha B_{AP}}\big)_{[\alpha\beta_i]}, & i = k, \\ \big(\mathbf{RRC}_{B_i,\alpha B_{AP}} * \overline{\mathbf{h}}_{k,n} * \mathbf{RRC}^{[\beta_k]}_{B_k,\alpha B_k}\big)_{[\alpha]}, & i \neq k, \end{cases}
\tag{5.21}
$$

where $\beta_i = B_{AP}/B_i$. From (5.21), the length of the equivalent CIR solely depends on the types of data stream and the receiving TD. Once the CIRs are estimated, various waveform design methods can be deployed. Take the basic TR waveform of the jth TD of type i for example, i.e.,

$$
g_{i,j}[n] = \frac{\widehat{h}^*_{i_j,i_j}[L - 1 - n]}{\|\widehat{\mathbf{h}}_{i_j,i_j}\|}.
\tag{5.22}
$$

Thus the received symbols at the jth of type i TD $\mathbf{Y}_{i,j}$ can be expressed as

$$
\begin{aligned}
Y_{i,j}[n] = {} & \frac{\sqrt{p_u}}{\beta_i} \left(\mathbf{g}_{i,j} * \widehat{\mathbf{h}}_{i_j,i_j} \right) [L_i - 1] X_{i,j}[n - \frac{L_i - 1}{D_{i,j}}] \\
& + \frac{\sqrt{p_u}}{\beta_i} \sum_{l=0, l \neq (L_i-1)/D_{i,j}}^{(2L_i-2)/D_{i,j}} \left(\mathbf{g}_{i,j} * \widehat{\mathbf{h}}_{i_j,i_j} \right) [D_{i,j}l] X_{i,j}[n - l] \\
& + \frac{\sqrt{p_u}}{\beta_i} \sum_{\substack{m=1 \\ m \neq j}}^{M_i} \sum_{\substack{l=0 \\ l \neq (L_i-1)/D_{i,m}}}^{(2L_i-2)/D_{i,m}} \left(\mathbf{g}_{i,m} * \widehat{\mathbf{h}}_{i_m,i_j} \right) [D_{i,m}l] X_{i,m}[n - l] \quad (5.23) \\
& + \sqrt{p_u} \sum_{k \in T_i} \sum_{m=1}^{M_k} \sum_{l=0}^{\frac{L_{k,i}-1}{\beta_k D_{k,m}}} \left(\mathbf{g}_{k,m}^{[\beta_k]} * \widehat{\mathbf{h}}_{k_m,i_j} \right) [\beta_k D_{k,m}l] X_{k,m}[n - l] \\
& + n_{i,j}[n],
\end{aligned}
$$

where $L_i = \text{length}\left(\widehat{\mathbf{h}}_{i_*,i_*} \right)$, $\beta_i = B_{AP}/B_i$ and $L_{k,i} = \text{length}\left(\mathbf{g}_{k,*}^{[\beta_k]} * \widehat{\mathbf{h}}_{k_*,i_*} \right)$.

In (5.23), the first term is the intended signal, the second and third term represents the ISI and the IUI within the same type and the ITI from overlapped types ($k \in T_i$) is expressed as the fourth term. Based on (5.23), the SINR for the jth TD in type i within the general heterogeneous TR system can be calculated correspondingly like (5.11).

5.4   Simulation Results

In this section, we conduct simulation to demonstrate the ability of proposed TR approach to support heterogeneous bandwidth devices with a reasonable BER performance. We assume that N types of TDs coexist in the system with single or multiple devices within each type. Different types devices have heterogenous bandwidths, spectrum occupation, hardware capabilities and QoS requirement. The CIR used in the simulation is based on the ultra-wide band (UWB) channel model of

IEEE P802.15 [24], which makes the simulation in the following a good predication of the system performance.

5.4.1 TDMA and Spectrum Allocation

We first consider 3 devices in the heterogeneous TR system, whose features are listed in Table 5.1. According to the table, the bit rates of the HD video and the HD audio are around 18 Mbits/s and 4 Mbits/s. Based on previous discussion, the bandwidth of AP is assumed to be 150MHz to support simultaneous data transmission to these 3 devices.

Device Name	Bandwidth (MHz)	Backoff Factor	Modulation	Coding Rate	Waveform Design
HD Video 1	150	8	QPSK	1/2	Basic TR
HD Audio 1	50	12	QPSK	1/2	Basic TR
HD Audio 2	50	12	QPSK	1/2	Basic TR

Table 5.1: Features of 1 HD Video and 2 HD Audio

We first consider the case that 3 devices are categorized into 2 types, where Type 1 includes the HD video device and Type 2 consists 2 HD audio devices. The BER performance of 3 devices under such scenario is shown in Fig. 5.9. Inferred from the figure, the BER performance of the 2 HD audio devices is much worse
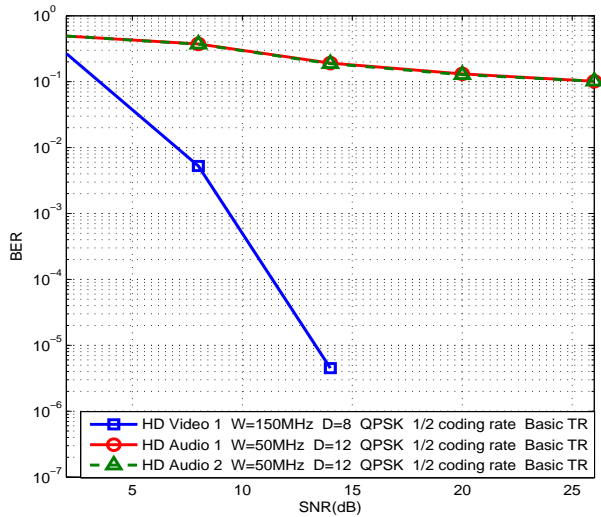
Figure 5.9: BER performance of 3 devices where 2 HD audio devices are included in the same type with basic TR waveform.

compared with the BER of HD video. The reason behind is that the suppression of IUI in the TR system heavily depends on the number of resolved independent multipaths, which increases with the bandwidth. Since the bandwidth of two HD audio is much narrower, the IUI from the other devices becomes severer with the basic TR waveform. In order to tackle the IUI for the devices with a narrower bandwidth, along with the TR technology, other techniques have to be considered in the heterogenous TR system as well.

We first consider applying time division multiple access (TDMA) to the heterogeneous TR system. In other words, the AP supports one HD audio at a time. To maintain the same QoS requirement in terms of bit rate, either adjusting the coding rate or decreasing the backoff factor is adopted in the system. The improved BER performance of 3 devices with simple waveform design is shown in Fig. 5.10,
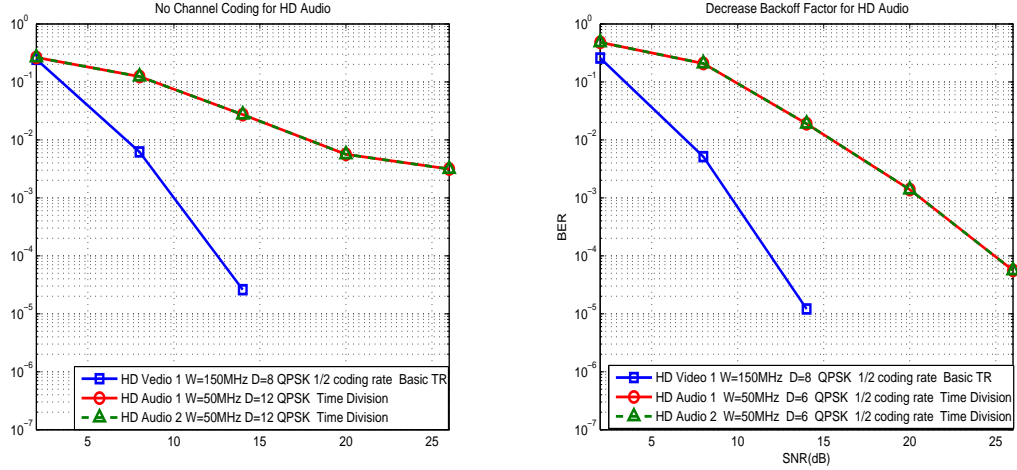
(a) No channel coding to maintain the same bit (b) Decrease backoff factor to maintain the same
rate.   bit rate.

Figure 5.10: Improved BER performance with TDMA for the HD audio.

where (a) removes the channel coding and (b) decreases the backoff rate to maintain
the same bit rate for the HD audio. Compared with the BER in Fig. 5.9, the BER
performance is improved significantly with the simple waveform design. Moreover,
decreasing backoff factor to maintain the bit rate seems to be a better strategy for
the devices with narrow bandwidth through comparing (a) and (b). Note that there
are some waveform design techniques [69] that potentially can be implemented in
the heterogeneous TR system with even better performance.

Even though a narrow bandwidth decreases the number of resolved indepen-
dent multipaths thus resulting in severer IUI, a narrow bandwidth on the other hand
provides more flexibility for spectrum allocation. Therefore, another way to improve
the BER performance in Fig. 5.9 is to arrange the spectrum occupation smartly
thus removing the unnecessary interference. For example, 3 devices in Table 5.1 can
be categorized into 3 distinct types, where two HD audio devices are allocated into
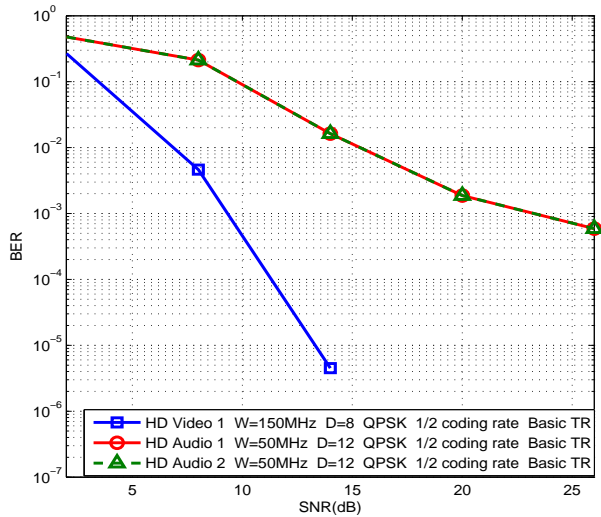
Figure 5.11: Improved BER performance with spectrum allocation for the HD audio 2 spectrally non-overlapped types. Then the improved BER performance with the spectrum allocation is shown in Fig. 5.11.

5.4.2 Heterogeneous TR System versus Homogeneous TR System

As discussed in the previous subsection, appropriate spectrum allocation can significantly improve the BER performance even with a narrow bandwidth in the heterogeneous TR system. In other words, the narrow bandwidth under heterogeneous setting does not necessarily lead to worse BER performance compared with the wide bandwidth under homogeneous setting. Inspired by that, we investigate the BER performance of the devices in both homogeneous and heterogeneous TR system under the same bit rate.

Assume there exists three devices with bit rate requirement of 12.5 Mbits/s supported by a TR AP with 150 MHz bandwidth. Suppose the devices have flexible

hardware capabilities, i.e., the carrier frequency and the bandwidth. To support these devices, two potential paradigms, homogeneous paradigm and heterogeneous paradigm, are available. For the sake of fairness, the basic TR waveform is adopted in both paradigms.

In the homogeneous setting, all three devices occupy the 150 MHz spectrum with QPSK modulation and backoff factor $D = 12$. A channel coding with 1/2 coding rate is employed. In the heterogeneous setting, the devices are categorized into three non-overlapped types. More specifically, three devices with 50MHz bandwidth are allocated into three non-overlapped spectrum. To maintain the same bit rate, a backoff factor $D = 4$ is implemented. Their BER performance is shown in Fig. 5.12. From the figure, the BER performance of the homogeneous paradigm saturates fast, which is due to the well-known fact that ISI and IUI would dominate the noise with the basic TR waveform at high SNR region [69]. However, the IUI is better tackled in the heterogenous paradigm with smart spectrum allocation even though the number of independent multipaths resolved by the narrower bandwidth becomes fewer. Therefore, the performance of the heterogeneous paradigm can be even better than that of the homogeneous paradigm with additional techniques like spectrum allocation.

5.4.3 Heterogeneous TR System Case Study: Smart Homes

In this subsection, we choose Smart Homes as an example of the IoT application to test the BER performance with the heterogeneous TR paradigm. Instru-

Device Name	Bandwidth (MHz)	Backoff Factor	Modulation	Coding Rate	Waveform Design
HD Video 1	150	8	QPSK	1/2	Basic TR
HD Audio 1	50	12	QPSK	1/2	Basic TR
Smart Sensor 1	10	10	QPSK	1/2	Basic TR
Smart Sensor 2	10	10	QPSK	1/2	Basic TR
Smart Sensor 3	10	10	QPSK	1/2	Basic TR
Smart Sensor 4	10	10	QPSK	1/2	Basic TR
Smart Sensor 5	10	10	QPSK	1/2	Basic TR

Table 5.2: Features of Devices in the Smart Homes
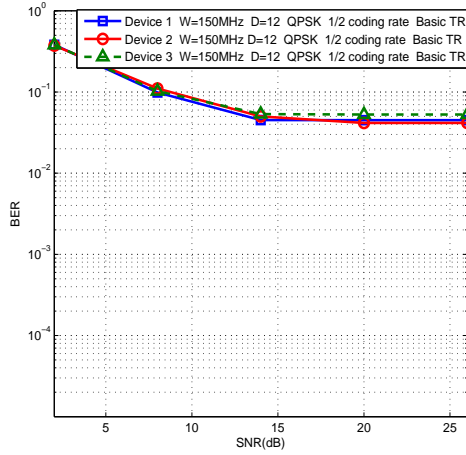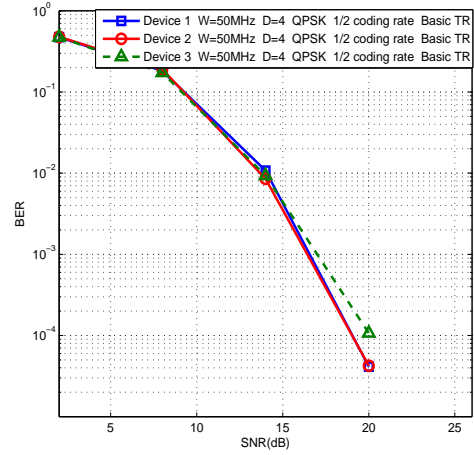
(a) Homogeneous Paradigm. (b) Heterogeneous Paradigm.

Figure 5.12: BER Comparison of Homogeneous Paradigm and Heterogeneous Paradigm with Basic TR Waveform.

menting buildings with the IoT technologies will help in not only reducing resources (electricity, water) consumption but also in improving the satisfaction level of humans. Typically, the HD video and HD audio are employed in the Smart Homes for both the security monitoring and entertainment. Moreover, smart sensors are used in the Smart Homes to both monitor resource consumptions as well as to proactively detect the users' need. Therefore, in the following simulation, we assume 1 HD video, 1 HD audio and 5 smart sensors in the Smart Homes are supported by the heterogeneous TR paradigm. The specific features of these devices are listed in Table 5.2 and the corresponding BER performance is shown in Fig 5.13. Note the saturation of the BER for the HD video is due to the dominant IUI with the basic TR waveform. In addition, the slight difference in the BER for the smart sensors comes from the frequency-selectivity of the channel.
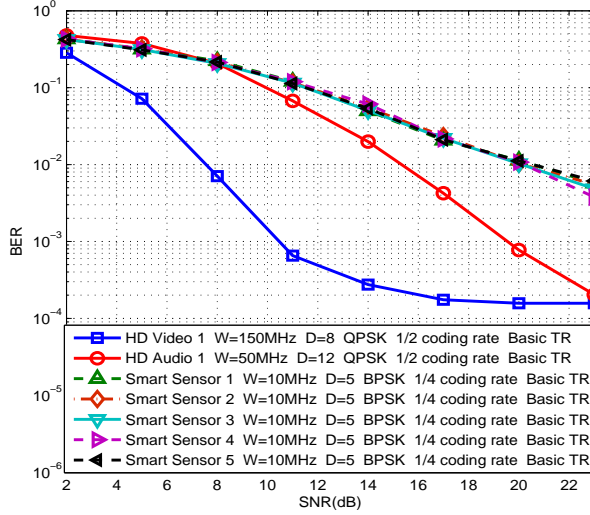
Figure 5.13: BER Performance of the Devices in Smart Homes

5.5 Conclusion

A novel TR-based heterogeneous communication system is developed to support devices with various bandwidths in IoT. Different from building middlewares, the proposed approach enables connectivity between devices with heterogeneous bandwidth requirement by means of multirate signal processing. In this way, the complexity of the proposed system mostly lies in the parallel digital processing at the AP side, which can be easily handled with more powerful DSP, while maintaining low complexity of the TDs. Therefore, compared with middleware approach, the proposed TR approach better satisfies the requirement of low-complexity and energy-efficiency for terminal devices in IoT. System performance is evaluated through both theoretical analysis and simulations, which show that the proposed system can serve the devices of heterogeneous bandwidths with a reasonable BER performance and the BER performance can be improved significantly with appropriate spectrum

allocation.

Chapter 6

Conclusions and Future Work

6.1 Conclusions

In the first part of this dissertation, we demonstrated the great potential of TR technique by theoretically deriving the massive multipath effect. We answered the bandwidth requirement of TR technique by evaluating the maximal spectral efficiency. We generated a tradeoff between complexity and performance in TR system by deriving the effective SINR as a function of quantization stepsize. In the second part of dissertation, we tackled the heterogeneous bandwidth problem in IoT by proposing a modified TR-based heterogeneous paradigm. More specifically, we address the following problems in this dissertation.

In Chapter 2, we demonstrated that the TR technology, through harvesting the naturally existing virtual antennas, can offer a cost effective solution to realize the massive multipath effect, which is a counterpart of massive MIMO effect in indoor scenarios. With the derived massive multipath effect, we further derived the asymptotic rates of TR technology in a rich-scattering environment. We validated with simulations that the TR system with typical waveforms can asymptotically achieve the limiting achievable rate, where the interference is completely eliminated.

Finally, based on the real channel measurements, it was shown that the single-antenna TR wideband system can achieve promising rates in a practical indoor environment. By utilizing the environment as virtual antenna array and computing resource, the low complexity of TR technology is ideal for indoor communications. What a TR system needs is a large enough bandwidth to harvest the multipaths in the environment, which can be made possible with more affordable high-speed ADC and wide spectrum in mmWave band.

In Chapter 3, we evaluated the bandwidth requirement for the TR system to achieve the maximum spectral efficiency. Through evaluating the spectral efficiency of TR system with both basic TR waveform and ZF waveform, we found that the optimal bandwidth for TR system, instead of being affected by the waveform types, is determined by the system parameters such as the number of users N and backoff factor D. We validated with simulations that the optimal bandwidth increases with D when D is small while increases with N when D is large. Finally, based on the rank condition of channel matrix, a sub-optimal bandwidth was proposed for TR system. Based on the simulation results, it was shown that the sub-optimal bandwidth serves as a low bound for optimal bandwidth and the bound is quite tight when D is small.

In Chapter 4, we analyzed the TRDMA system with limited waveform precision and studied the corresponding tradeoff between the complexity and performance. We derived an approximated closed-form expression of the effective SINR as a function of quantization stepsize, according to which we investigated the number of quantization bits required for the TRDMA system to achieve reasonable perfor-

mance. A metric α was proposed to depict the performance loss due to the quantization. Simulation results demonstrated that our theoretical analysis match well with the numerical results when the quantization stepsize is not too large. Through evaluating α with varying D and N, a promising property had been discovered that the number of quantization bits need no modification with varying D to maintain the same level of system performance. Finally, we concluded that 4-bit resolution for waveform is enough for the TRDMA system based on the BER performance evaluation.

Lastly, in Chapter 5, we first developed a novel TR-based heterogeneous communication system to support devices with various bandwidths in IoT. Different from building middlewares, the proposed approach enabled connectivity between devices with heterogeneous bandwidth requirement by means of multirate signal processing. In this way, the complexity of the proposed system mostly lay in the parallel digital processing at the AP side, which can be easily handled with more powerful DSP, while maintaining low complexity of the TDs. Therefore, compared with middleware approach, the proposed TR approach better satisfied the requirement of low-complexity and energy-efficiency for terminal devices in IoT. Then, system performance was evaluated through both theoretical analysis and simulations, which showed that the proposed system could serve the devices of heterogeneous bandwidths with a reasonable BER performance and the BER performance could be improved significantly with appropriate spectrum allocation.

6.2 Future Work

To meet the exponentially increasing demand of wireless data and various applications, there are numerous challenges need to be addressed, and the development in surmounting these challenges will not only lead to fruitful research, but also improve our everyday life and behavior. In this dissertation, the TR technique for both 5G and IoT can be further studied in many perspectives as follows.

First, we have made several assumptions about the waveforms to better elucidate the proposed ideas of solving the problems. In practice, many possible impairments besides quantization such as timing synchronization error, channel estimation error, carrier/sampling frequency offset, DC offset, and IQ imbalance, can weaken the assumptions and degrade the performance. Therefore, it is important to study the effect of these impairments on the system performance. For example, the channel knowledge at the transmitter cannot be perfect due to all the impairments occurring when estimating the channel impulse response. To tackle these impairments, the robust waveform design can be formulated and investigated.

Another important aspect in TR communication is the channel probing mechanism. In the channel probing phase, the base station has no information about the individual receiver. This fact makes the channel probing the most difficult task considering the multiuser and mobile communication scenario. For example, even though orthogonal pilot can be used to simultaneously probe the channel by the multiple users, TR system still faces the pilot contamination problem considering the multicell and a huge number of coexist users in 5G communication scenario.

Considering the mobile communication, individual will join and leave the cell frequently, the mechanism about channel information update and waveform redesign will significantly affect the efficiency of TR communication in the practical scenario.

Considering the large bandwidth required by TR technique, mmWave band is the most promising available spectrum except the industrial, scientific and medical (ISM) band. Due to the extremely high carrier frequency, mmWave band is highly likely to owe some distinct RF characteristics compared to the traditional ultra-wide-band (UWB) in IEEE P802.15. The traditional channel model may not fully characterize these properties and therefore the evaluation of TR technique on the new band is of much importance.

For the IoT, we demonstrated that the TR-based heterogeneous paradigm could support devices of heterogeneous bandwidths simultaneously. These devices are currently supported by the basic TR waveform. It is known that, when the symbol rate is very high, such ISI can be notably severe and causes crucial performance degradation. To enable high data rate in the IoT, we need to consider the advanced waveforms. Even though waveform design has been studied in several existing work, the formulation of waveform design for devices of heterogeneous bandwidth has not been considered.

Bibliography

[1] D. Abbasi-Moghadam and V.T. Vakili. A simo one-bit time reveresal for uwb communication systems. *EURASIP Journal on Wireless Communications and Networking*, pages 1–9, 2012.

[2] J.G. Andrews, S. Buzzi, Choi Wan, S.V. Hanly, A. Lozano, A.C.K. Soong, and J.C. Zhang. What will 5g be? *IEEE J. Sel. Areas Commun.*, 32(6):1065–1082, 2014.

[3] X. Artiga, B. Devillers, and J. Perruisseau-Carrier. Mutual coupling effects in multi-user massive mimo base stations. In *Proc. of IEEE APSURSI*, pages 1–2, 2012.

[4] Kevin Ashton. That internet of things thing. *RFiD Journal*, 22(7):97–114, 2009.

[5] Luigi Atzori, Antonio Iera, and Giacomo Morabito. The internet of things: A survey. *Computer networks*, 54(15):2787–2805, 2010.

[6] I.H. Azzam and R.S. Adve. Linear precoding for multiuser mimo systems with multiple base stations. *in Proc. IEEE ICC*, pages 1–6, 2009.

[7] F. Boccardi, R.W. Heath, A. Lozano, T.L. Marzetta, and P. Popovski. Five disruptive technology directions for 5g. *IEEE Commun. Mag.*, 52(2):74–80, 2014.

[8] B. P. Bogert. Demonstration of delay distortion correction by time-reversal techniques. *IRE Trans. Commun. Syst.*, 5(3):2–7, 1957.

[9] M.-A. Bouzigues, I. Siaud, M. Helard, and A.-M. Ulmer-Moll. Turn back the clock: time reversal for green radio communications. *IEEE Veh. Technol. Magazine*, 8(1):49–56, 2013.

[10] J. Buckley. *The Internet of Things: From RFID to the Next-Generation Pervasive Networked Systems*. Auerbach Publications, Nework York, 2006.

[11] Y.H. Chang, S.H. Tsai, X. Yu, and C.C.J. Kuo. Ultrawideband transceiver design using channel phase precoding. *IEEE Trans. Signal Processing*, 55(7):3807–3822, 2007.

[12] Y. Chen, B. Wang, Y. Han, H. Q. Lai, Z. Safar, and K. J. R. Liu. Why time reversal for future 5g wireless? [perspectives]. *IEEE Signal Processing Magazine*, 33(2):17–26, March 2016.

[13] Yan Chen, Feng Han, Yu-Han Yang, Hang Ma, Yi Han, Chunxiao Jiang, Hung-Quoc Lai, D. Claffey, Z. Safar, and K. J. R. Liu. Time-reversal wireless paradigm for green internet of things: An overview. *IEEE Internet of Things Journal*, 1(1):81–98, Feb 2014.

[14] Cisco. Visual networking index. *Cisco white paper*, 2016.

[15] R.C. Daniels and R.W. Heath. Improving on time-reversal with miso precoding. In *Proc. of 8th Int. Symp. Wireless Pers. Commun. Conf.*, pages 18–22, 2005.

[16] S. de Deugd, R. Carroll, K.E. Kelly, B. Millett, and J. Ricker. Soda: Service oriented device architecture. *Pervasive Computing, IEEE*, 5(3):94–96, July 2006.

[17] R.L. de Lacerda Neto, A.M. Hayar, and M. Debbah. Channel division multiple access based on high uwb channel temporal resolution. *in Proc. IEEE VTC*, pages 1–5, 2006.

[18] Eli De Poorter, Ingrid Moerman, and Piet Demeester. Enabling direct connectivity between heterogeneous objects in the internet of things through a network-service-oriented architecture. *EURASIP Journal on Wireless Communications and Networking*, 2011(1):1–14, 2011.

[19] A. Derode, P. Roux, and M. Fink. Robust acoustic time reversal with high order multiple scattering. *Phys. Rev. Lett.*, 75:4206–4209, 1995.

[20] A. Derode, A. Tourin, and M. Fink. Ultrasonic pulse compression with one-bit time reversal through multiple scattering. *Journal of applied physics*, 85(9):6343–6352, 1999.

[21] G.F. Edelmann, T. Akal, W.S. Hodgkiss, S. Kim, W.A. Kuperman, and H.C. Song. An initial demonstration of underwater acoustic communication using time reversal. *IEEE J. Ocean. Eng.*, 27(3):602–609, 2002.

[22] M. Emami, Mai Vu, J. Hansen, A.J. Paulraj, and G. Papanicolaou. Matched filtering with rate back-off for low complexity communications in very large delay spread channels. *Conference Record of the Thirty-Eighth Asilomar Conference on Signals, Systems and Computers*, 1:218–222, Nov 2004.

[23] M. Fink and C. Prada. Acoustic time-reversal mirrors. *Inverse problems*, 17(1):R1, 2001.

[24] Jeff Foerster. Channel modeling sub-committee report final. *IEEE P802. 15-02/368r5-SG3a*, 2002.

[25] Ian Glover and Peter M Grant. *Digital communications*. Pearson Education, 2010.

[26] Marcel JE Golay. Complementary series. *IRE Transactions on Information Theory*, 7(2):82–87, 1961.

[27] Jayavardhana Gubbi, Rajkumar Buyya, Slaven Marusic, and Marimuthu Palaniswami. Internet of things (iot): A vision, architectural elements, and future directions. *Future Generation Computer Systems*, 29(7):1645–1660, 2013.

[28] F. Han, Y.H. Yang, B. Wang, Y. Wu, and K. J. Ray Liu. Time-reversal division multiple access over multi-path channels. *IEEE Trans. Commun.*, 60(7):1953–1965, 2012.

[29] Y. Han, Y. Chen, and K. J. R. Liu. Time-reversal with limited signature precision: Tradeoff between complexity and performance. In *Signal and Information Processing (GlobalSIP), 2014 IEEE Global Conference on*, pages 664–668, Dec 2014.

[30] Y. Han, Y. Chen, B. Wang, and K. J. R. Liu. Enabling heterogeneous connectivity in internet of things: A time-reversal approach. *IEEE Internet of Things Journal*, PP(99):1–1, 2016.

[31] Aawatif Menouni Hayar, Raymond Knopp, and Rachid Saadane. Subspace analysis of indoor uwb channels. *EURASIP J. Appl. Signal Process.*, 2005:287–295, 2005.

[32] R. Hunger and M. Joham. A general rate duality of the mimo multiple access channel and the mimo broadcast channel. *in Proc. IEEE Global Telecommun. Conf.*, 2008.

[33] A. Inamdar, S. Rylov, A. Talalaevskii, A. Sahu, S. Sarwana, D.E. Kirichenko, I.V. Vernik, T.V. Filippov, and D. Gupta. Progress in design of improved high dynamic range analog-to-digital converters. *IEEE Trans. Appl. Supercond.*, 19(3):670–675, 2009.

[34] Y. Jin, J. Yi, and J.M.F. Moura. Multiple antenna time reversal transmission in ultra-wideband communications. *in Proc. IEEE GlOBECOM*, pages 26–30, 2007.

[35] Liu Kewen, Ma Zherui, and He Ting. A novel tr-stbc-ofdm scheme for mobile wimax system. *in Proc. IEEE ISAPE*, pages 1365–1368, 2008.

[36] P. Kyritsi and G. Papanicolaou. One-bit time reversal for wlan applications. *In Personal, Indoor and Mobile Radio Communications, 2005. PIMRC 2005. IEEE 16th International Symposium on*, 1:532–536, 2005.

[37] Jungwon Lee, Hui-Ling Lou, D. Toumpakaris, and J.M. Cioffi. Snr analysis of ofdm systems in the presence of carrier frequency offset for fading channels. *Wireless Communications, IEEE Transactions on*, 5(12):3360–3364, December 2006.

[38] S.K. Lehman and A.J. Devaney. Transmission mode time-reversal super-resolution imaging. *J. Acoust. Soc. Amer.*, 113(5):2742–2753, 2003.

[39] D. Liu, G. Kang, L. Li, Y. Chen, S. Vasudevan, W. Joines, Q.H. Liu, J. Krolik, and L. Carin. Electromagnetic time-reversal imaging of a target in a cluttered environment. *IEEE Trans. Antennas Propag.*, 53(9):3508–3066, 2005.

[40] Jin Liu, Hlaing Minn, and Alan Gatherer. The death of 5g part 2: Will analog be the death of massive mimo? Downloaded from http://www.comsoc.org/ctn/death-5g-part-2-will-analog-be-death-massive-mimo, June 2015.

[41] M. Maaz, M. Helard, P. Mary, and M. Liu. Performance analysis of time-reversal based precoding schemes in miso-ofdm systems. *in Proc. IEEE VTC*, pages 1–6, 2015.

[42] T.L. Marzetta. Noncooperative cellular wireless with unlimited numbers of base station antennas. *IEEE Trans. Wireless Commun.*, 9(11):3590–3600, 2010.

[43] C. Masouros, M. Sellathurai, and T. Ratnarajah. Large-scale mimo transmitters in fixed physical spaces: the effect of transmit correlation and mutual coupling. *IEEE Trans. Commun.*, 61(7):2794–2804, 2013.

[44] Paul H. Moose. A technique for orthogonal frequency division multiplexing frequency offset correction. *IEEE Transactions on Communications*, 42(10):2908–2914, Oct 1994.

[45] National Intelligence Coucil. Disruptive civil technologies - six technologies with potential impacts on us interests out to 2025 - conference report cr 2008-07. Downloaded from http://www.dni.gov/nic, April 2008.

[46] H.Q. Ngo, E.G. Larsson, and T.L. Marzetta. Energy and spectral efficiency of very large multiuser mimo systems. *IEEE Trans. Commun.*, 61(4):1436–1449, 2013.

[47] H.T. Nguyen. On the performance of one bit time reversal for multi-user wireless communications. In *Wireless Communication Systems, 2007. ISWCS 2007. 4th International Symposium on*, pages 672–676, 2007.

[48] H.T. Nguyen, J.B. Anderson, and G.F. Pedersen. The potential of time reversal techniques in multiple element antenna systems. *IEEE Commun. Lett.*, 9(1):40–42, 2005.

[49] Alan V Oppenheim, Ronald W Schafer, John R Buck, et al. *Discrete-time signal processing*. Prentice-hall Englewood Cliffs, 1989.

[50] Monica Panolini. Beyond data caps: An analysis of the uneven growth in data traffic. Downloaded from http://www.senzafiliconsulting.com, March 2011.

[51] J. Pasley. How bpel and soa are changing web services development. *Internet Computing, IEEE*, 9(3):60–67, May 2005.

[52] Antonios Pitarokoilis, Saif Khan Mohammed, and Erik G Larsson. Uplink performance of time-reversal mrc in massive mimo systems subject to phase noise. *IEEE Trans. Wireless Commun.*, 14(2):711–723, 2015.

[53] B.M. Popovic. Efficient golay correlator. *Electron. Lett.*, 35(17):1427–1428, Aug 1999.

[54] T.S. Rappaport, Shu Sun, R. Mayzus, Hang Zhao, Y. Azar, K. Wang, G.N. Wong, J.K. Schulz, M. Samimi, and F. Gutierrez. Millimeter wave mobile communications for 5g cellular: It will work! *IEEE Access*, 1:335–349, 2013.

[55] R. Saadane, A. Menouni, R. Knopp, and D. Aboutajdine. Empirical eigen-analysis of indoor uwb propagation channels. In *Proc. of IEEE GLOBECOM*, volume 5, pages 3215–3219, 2004.

[56] M. Schubert and H. Boche. Solution of the multiuser downlink beamforming problem with individual sinr constraints. *IEEE Trans. Veh. Technol.*, 53(1):18–28, 2004.

[57] P.F.M. Smulders and L.M. Correia. Characterisation of propagation in 60 ghz radio channels. *Electron. Commun. Eng. J.*, 9(2):73–80, Apr 1997.

[58] P. Spiess, S. Karnouskos, D. Guinard, D. Savio, O. Baecker, L. Souza, and V. Trifa. Soa-based integration of the internet of things in enterprise services. pages 968–975, July 2009.

[59] Harald Sundmaeker, Patrick Guillemin, Peter Friess, and Sylvie Woelfflé. Vision and challenges for realising the internet of things. 2010.

[60] E. Telatar. Capacity of multiple-antenna gaussian channels. *European Trans. Telecommun.*, 10(6):585–595, 1999.

[61] D. Tse and P. Viswanath. Downlink-uplink duality and effective bandwidths. *in Proc. IEEE ISIT*, 2002.

[62] Parishwad P Vaidyanathan. *Multirate systems and filter banks*. Pearson Education India, 1993.

[63] J. Vieira, S. Malkowsky, K. Nieman, Z. Miers, N. Kundargi, Liang Liu, I. Wong, V. Owall, O. Edfors, and F. Tufvesson. A flexible 100-antenna testbed for massive mimo. In *Proc. of IEEE GC Wkshps*, pages 287–293, 2014.

[64] Andrew J Viterbi. *CDMA: principles of spread spectrum communication*. Addison Wesley Longman Publishing Co., Inc., 1995.

[65] B. Wang, Y. Wu, F. Han, Y.H. Yang, and K. J. Ray Liu. Green wireless communications: a time-reversal paradigm. *IEEE J. Select. Areas Commun.*, 29(8):1698–1710, 2011.

[66] Bernard Widrow and István Kollár. Quantization noise: Roundoff error in digital computation. *Signal Processing, Control, and Communications*, pages 485–528, 2008.

[67] Zhung-Han Wu, Yi Han, Yan Chen, and K. J. R. Liu. A time-reversal paradigm for indoor positioning system. *IEEE Trans. Veh. Technol.*, 64(4):1331–1339, 2015.

[68] Y. H. Yang and K. J. Ray Liu. Waveform design with interference pre-cancellation beyond time-reversal systems. *IEEE Transactions on Wireless Communications*, 15(5):3643–3654, May 2016.

[69] Yu-Han Yang, Beibei Wang, W Sabrina Lin, and K. J. Ray Liu. Near-optimal waveform design for sum rate optimization in time-reversal multiuser downlink systems. *IEEE Trans. Wireless Commun.*, 12(1):346–357, 2013.

[70] E. Yoon, S. Kim, and U. Yun. A time-reversal-based transmission using pre-distortion for intersymbol interference alignment. *IEEE Trans. Commun.*, 63(2):455–465, 2014.

[71] Chenming Zhou, Nan Guo, B.M. Sadler, and R.C. Qiu. Performance study on time reversed impulse mimo for uwb communications based on measured spatial uwb channels. *in Proc. IEEE MILCOM*, pages 1–6, 2007.

[72] Michele Zorzi, Alexander Gluhak, Sebastian Lange, and Alessandro Bassi. From today's intranet of things to a future internet of things: a wireless-and mobility-related view. *Wireless Communications, IEEE*, 17(6):44–51, 2010.